

1



2

Exploiting CVD diamond properties for particle detection and identification

3

4

5

Matevž Červ

6

Vienna University of Technology

7

A thesis submitted for the degree of

8

Doctor of technical sciences

9

Geneva 2016

¹⁰ Contents

¹¹ 1	Introduction	1
¹² 1.1	Fundamental research	2
¹³ 1.1.1	CERN	3
¹⁴ 1.1.2	Particle accelerators	4
¹⁵ 1.1.3	The ATLAS experiment	5
¹⁶ 1.1.4	Atominsttitut, Vienna	6
¹⁷ 1.1.5	n-ToF	7
¹⁸ 1.2	Particle detectors	8
¹⁹ 1.2.1	Semiconductor detectors	9
²⁰ 1.2.2	Diamond sensors	10
²¹ 2	Signal formation in diamond	12
²² 2.1	Principles of signal formation in semiconductors	13
²³ 2.1.1	Signal induction by moving charges	15
²⁴ 2.1.2	Radiation-induced electrical pulses	17
²⁵ 2.1.3	Signal charge fluctuations	18
²⁶ 2.2	Carrier transport in a diamond sensor	18
²⁷ 2.3	Electronics for signal processing	21
²⁸ 2.3.1	Signal preamplifiers	21
²⁹ 2.3.1.1	Current-sensitive amplifier	21
³⁰ 2.3.1.2	Charge-sensitive amplifier	22
³¹ 2.3.1.3	Analogue electronic noise	23
³² 2.3.2	Analogue-to-digital converters	23
³³ 2.3.3	Digital signal processing	24
³⁴ 3	Experimental results	
³⁵	<i>Diamond irradiation study</i>	27
³⁶ 3.1	Measurement setup	28
³⁷ 3.1.1	Preamplifiers	28
³⁸ 3.1.1.1	Calibration	29
³⁹ 3.1.2	Diamond samples	30
⁴⁰ 3.1.3	Readout devices	31
⁴¹ 3.1.4	Setup for the efficiency study using β particles	31
⁴² 3.1.5	Room temperature α -TCT setup	32

CONTENTS

43	3.1.6	Cryogenic α -TCT setup	32
44	3.2	Charged particle pulses and spectra	34
45	3.2.1	Noise limitations	34
46	3.3	Radiation limitations	36
47	3.3.1	Quantifying radiation damage in diamonds	37
48	3.3.1.1	Irradiation with a $\pi_{300 \text{ MeV}}$ beam	37
49	3.3.1.2	Charge collection efficiency and charge collection distance	38
50	3.3.1.3	Irradiation damage factor	39
52	3.3.2	Long-term measurement stability	40
53	3.3.2.1	β long-term stability	41
54	3.3.2.2	α long-term stability	42
55	3.4	Temperature limitations	46
56	3.4.1	Temperature-variant α -TCT before irradiation	48
57	3.4.2	Temperature-variant α -TCT after irradiation	50
58	3.4.2.1	Collected charge as a function of temperature	51
59	3.4.2.2	Charge trapping	53
60	3.5	Conclusion	57
61	4	Charge monitoring	
62		<i>The ATLAS Diamond Beam Monitor</i>	58
63	4.1	Luminosity measurements	59
64	4.2	Diamond pixel module	60
65	4.2.1	Sensors	61
66	4.2.2	Front-end electronics	62
67	4.3	Module assembly and quality control	64
68	4.3.1	Assembly	64
69	4.3.2	Testing	65
70	4.3.3	Installation and commissioning	66
71	4.4	Performance results	67
72	4.4.1	Source tests	67
73	4.4.2	Test beam results	68
74	4.5	Operation	70
75	4.5.1	Positioning	70
76	4.5.2	Data taking during collisions	71
77	4.6	Conclusion	74
78	5	Current monitoring	
79		<i>Real-time particle identification</i>	75
80	5.1	Motivation	76
81	5.2	Requirements	76
82	5.3	Device specifications	77
83	5.4	Pulse parameters	77

CONTENTS

84	5.5 Applications	78
85	5.6 Description of the firmware	79
86	5.6.1 Analysis module	80
87	5.6.2 Vector cleaning for area and width measurements	82
88	5.6.2.1 Vector cleaning	83
89	5.6.2.2 Algorithm	84
90	5.7 Control and data interface	84
91	5.7.1 Software	85
92	5.7.2 Data readout	85
93	5.8 Performance results	87
94	5.8.1 Comparison between the charge- and current-sensitive spec-	
95	troscopy	88
96	5.9 Source calibration	88
97	5.9.1 Source measurements - scatter plots	92
98	5.9.2 Discussion	100
99	5.9.3 Space charge build-up	101
100	5.10 Applications in neutron instrumentation	103
101	5.10.1 Thermal neutron flux monitoring	103
102	5.10.1.1 Measurements	104
103	5.10.1.2 Results	105
104	5.10.2 Fusion power monitoring	105
105	5.10.3 Fast neutron monitoring	106
106	5.11 Conclusion	108

¹⁰⁷ **List of Figures**

108	1.1	Standard model [22]	2
109	1.2	The Large Hadron Collider [20]	4
110	1.3	The ATLAS Experiment [38]	5
111	1.4	The TRIGA MARK II neutron reactor [15]	7
112	1.5	The calorimeter in the n-ToF area [19]	8
113	1.6	The Insertable B-Layer – a silicon particle tracker installed in the ATLAS experiment in 2014 [34]	9
114	1.7	A pCVD diamond pad detector [23]	10
116	2.1	In the equivalent electrical circuit diagram, electron-hole creation and drift can be modelled as a current source with a capacitor in parallel	14
117	2.2	Stopping power for muons according to the Bethe-Bloch formula []	15
118	2.3	A point-like charge inducing current in a conductive plane	15
119	2.4	Charge carrier drift in diamond for β/γ and for α particles	17
120	2.5	Calculated intrinsic energy resolution for silicon and diamond	19
122	2.6	Introduction of space charge in the diamond bulk. The induced current signal is proportional to the effective electrical field. d is the thickness of the diamond sensor.	20
123	2.7	Introduction of impurities and non-uniformities into the crystal lattice due to radiation damage.	21
124	2.8	Simplified equivalent circuits of a current and charge amplifier	22
125	2.9	Input and output signal of the current amplifier	22
126	2.10	Input and output signal of the charge amplifier	23
127	2.11	Input signal digitisation and quantisation error	24
128	2.12	An example of an FPGA and an ASIC chip	26
132	3.1	Diagram of a diamond detector readout chain.	28
133	3.2	Amplifiers used for the charge and current measurements	29
134	3.3	Two scCVD diamond samples: A IIa 1scdhq (left) and an E6 S37 (right)	30
135	3.4	Positioning of the α -source on top of the sensor carrier	33
136	3.5	Superimposed and averaged pulses (a, b and c, current amplifier) and distributions of deposited energy (d, e, f, charge amplifier) for three types of radiation. Note the scale on the X axis of the distributions.	35

LIST OF FIGURES

139	3.6	Diamond radiation damage - a model based on displacements per atom [26]. Added are data points for protons and pions by RD42 [35] and one data point for pions measured in the scope of this thesis.	38
140	3.7	First figure shows the CCD for S37, S79 and S52 at a range of bias voltage settings. The charge collection distance at 1 V/ μ m bias voltage for the three diamond samples is then compared to the RD42 data for pion irradiation in the second figure. The data points are about 15–25 % lower than expected from the RD42 data [35].	40
141	3.8	Relative increase of charge collection over time due to priming with the ^{90}Sr radioactive source. The bias voltage for this measurement is 1 V/ μ m.	42
142	3.9	Relative decrease of collected charge with time for non-irradiated and irradiated diamond samples.	43
143	3.10	The signal of the irradiated and primed S79 deteriorates with time for both polarities. Every plot contains 60 superimposed pulses.	44
144	3.11	Deterioration of the pulse shapes with time	45
145	3.12	Five procedures for the “healing” process for an irradiated diamond that was exposed to α radiation at bias voltage switched on for at least 30 minutes at a rate of 10^4 s $^{-1}$	47
146	3.13	Varied bias voltage at a fixed temperature	48
147	3.14	Several data points between 4 K and 295 K at a bias voltage of ± 500 V	49
148	3.15	Varied bias voltage at a fixed temperature for an irradiated sample	51
149	3.16	After irradiation: several data points between 4 K and 295 K at a bias voltage of ± 500 V	52
150	3.17	Collected charge as a function of temperature	54
151	3.18	Charge carrier lifetime decreases with irradiation, but is stable across the range of temperatures between 4 K – 75 K and 150 K – 295 K. The first figure shows the carrier lifetime s a function of temperature whereas the second figure depcits the carrier lifetime averaged over all temperatures and plotted against the π irradiation dose	56
152	4.1	Diamond detectors installed in high-energy physics experiments in the last decade, sorted by the active sensor area. The first four detectors from the left are radiation monitors whereas the right two are pixel trackers.	59
153	4.2	DBM module, top-down view. Visible is the flexible PCB with signal and power connections, the silicon sensor and a part of the FE-I4. Wire bonds from the PCB to the FE-I4 and to the sensor are also visible.	60
154	4.3	A pCVD wafer. The golden dots on the surface are the electrodes that are applied during the qualification test. The wafer is measured across the surface to find the regions with the highest efficiency.	61

LIST OF FIGURES

179	4.4	FE-I4 layout, top-down view. The pink area are pixels grouped into columns, the green area below is the common logic and the red strip at the bottom are the wire bond pads.	62
180	4.5	Schematic of an analog pixel. Courtesy of the FE-I4 collaboration. . .	63
181	4.6	Module production with time	66
182	4.7	Occupancy and pseudo-efficiency scans for the silicon (left) and diamond sensor (right) to check for disconnected regions and estimate the sensor's efficiency. Shadows of the electronic components are clearly visible because fewer electrons were able to traverse through such a higher amount of material.	69
183	4.8	Measurements of pseudo-efficiency and disconnected regions for all modules that went through the QC procedure	70
184	4.9	An efficiency study of a prototype DBM diamond module in a test beam. The statistics are low (~ 10 hits/pixel) as the data was collected during a short run.	70
185	4.10	This photo highlights four telescopes installed onto the nSQPs and around the pipe	71
186	4.11	Position of the DBM in the ATLAS experiment	72
187	4.12	Occupancy of individual modules during collisions. Only 16 modules were taking data.	72
188	4.13	A diagram showing the radial distance R_0 and longitudinal distance Z_0 of the trajectory from the interaction point at the minimal distance d . Z is the axis along the beam line. Three module planes intercept a particle and reconstruct its trajectory.	73
189	4.14	These two plots show two parameters of particle tracks recorded by one of the DBM telescopes: radial and longitudinal distance of the projected tracks from the interaction point.	73
190	5.1	78
191	5.2	Firmware design structure	80
192	5.3	A sample pulse. The first vector shows which samples are above the width measurement height. The second vector is a clean vector. The third line shows the position of the maximum amplitude. The vector cleaning algorithm starts from the maximum amplitude and continues in both ways along the vector.	82
193	5.4	This block counts the remaining binary ones in the clean vectors and outputs this value as the pulse width.	83
194	5.5	This block masks the input data with the clean vector and sums the remaining samples.	83
195	5.6	Vector cleaning routine outputs two vectors - one forward in time and one back in time from the peak of the pulse.	84
196	5.7	One logic step in the algorithm chain before and after Karnaugh minimisation.	84

LIST OF FIGURES

221	5.8 Abstraction levels of the controller software	85
222	5.9 This figure shows the capability of the device to analyse all arriving	
223	pulses for a range of input frequencies. The highest achievable rate	
224	with zero lost pulses is $5 \times 10^6 \text{ s}^{-1}$	87
225	5.10 These diagrams show the linearity of the measurements and their sta-	
226	bility with respect to analog noise.	89
227	5.11 Spectrum of a $^{148}\text{Gd}^{239}\text{Pu}^{241}\text{Am}^{244}\text{Cm}$ source using a Cx and a C2	
228	amplifier	90
229	5.12 Accumulated pulses for all runs	91
230	5.13 Background measurements	93
231	5.14 ^{241}Am , e^- collection. Qualifier: FWHM 7–10 ns.	94
232	5.15 ^{241}Am , h^+ collection. Qualifier: FWHM 5.5–8 ns.	95
233	5.16 ^{90}Sr	96
234	5.17 ^{60}Co	97
235	5.18 ^{239}Pu Be. Qualifiers: BW-FWHM 0.2–4 ns, FWHM 3–12 ns, Form	
236	factor 1.45	98
237	5.19 ^{239}Pu Be. Qualifiers: BW-FWHM 0.2–4 ns, FWHM 3–12 ns, Slope	
238	25–104 mV/ns	99
239	5.20 Built up space charge causes a slope which has the opposite slope for	
240	electrons and holes	101
241	5.21 Using β radiation to reduce space charge in diamond	102
242	5.22 Thermal neutrons, photons. Qualifier: FWHM 7–12 ns	105
243	5.23 Fast neutrons, thermal neutrons, photons. Qualifiers: BW-FWHM	
244	0–4 ns, FWHM 3–12 ns, Form factor 1.45, Slope 10–108 mV/ns	107

LIST OF FIGURES

²⁴⁵ Chapter 1

²⁴⁶ Introduction

²⁴⁷ The aim of the thesis is to present and discuss applications of diamond based particle
²⁴⁸ detectors.

²⁴⁹ The introductory chapter paints a picture of the current state of particle physics
²⁵⁰ research. It presents some of the research institutes that are active in this field,
²⁵¹ pushing the boundaries of human knowledge further. It explains their goals and the
²⁵² means with which they are achieving them. Next section describes particle detectors
²⁵³ in a broad sense – their history and the types existing now. One type in particular –
²⁵⁴ a diamond detector – is then described more in detail.

²⁵⁵ Second chapter discusses the properties of diamond detectors. Dissecting the
²⁵⁶ detector chain into individual parts and describing them in detail – sensors, amplifiers,
²⁵⁷ digitisers and signal processing units. We learn about energy resolution in diamond,
²⁵⁸ analog and digital noise contribution etc. Principles of signal formation are presented,
²⁵⁹ starting with the famous Shockley-Ramo theorem and building from there. We will
²⁶⁰ see that different types of radiation induce different electrical signals.

²⁶¹ The base laid down in the second chapter is complemented in the third where the
²⁶² measurements are presented and the results discussed. The focus is on diamond's
²⁶³ measurement stability with respect to irradiation damage. To carry out this study,
²⁶⁴ two diamond sensors were irradiated to two different doses, with the measurements
²⁶⁵ carried out before and after irradiation.

²⁶⁶ Building on the understanding of the behaviour of the diamond, two applications
²⁶⁷ were developed. The fourth chapter describes the Diamond Beam Monitor, a detec-
²⁶⁸ tor that makes use of the diamond's charge measurement capabilities and its high
²⁶⁹ radiation hardness. This detector has been installed in one of the largest particle
²⁷⁰ physics experiments in the world and is currently taking data. Here, its development
²⁷¹ process is presented: the quality control procedures during assembly and installation,
²⁷² its performance in the test environment and some recent experimental data.

²⁷³ The final and most important chapter describes the real-time application for par-
²⁷⁴ ticle identification. Here the shape of the electrical signal of the diamond sensor is
²⁷⁵ used to discriminate different types of radiation in real time and dead time free. The
²⁷⁶ chapter includes the description of the device's logic and algorithms, lab test results
²⁷⁷ and the application in neutron monitoring.

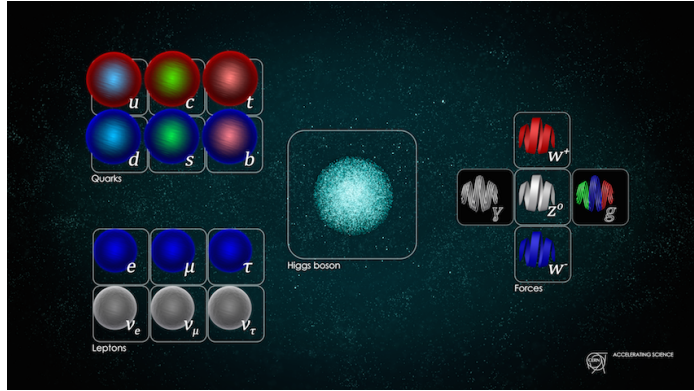


Figure 1.1: Standard model [22]

278 1.1 Fundamental research

279 This section gives a short overview of the institutes and collaborations carrying out
 280 fundamental physics research. The facilities were used for the research carried out in
 281 this thesis.

282 The aim of fundamental (even pure or basic) research is to improve the scientific
 283 theories and verify them to improve our understanding of the universe. It does not
 284 in itself focus on applying this research by developing products and is not meant to
 285 create a direct return on investment. Instead, it expands the overall knowledge of the
 286 human kind - by making the results freely available to the general public.

287 Particle physics research peers into the smallest constituents of the universe, dis-
 288 secting the atoms into quarks and electrons, catching cosmic rays and figuring out
 289 what dark matter is made up of. Particle physicists want to explain the phenomena
 290 surrounding us by studying the fundamental particles and the mechanisms governing
 291 their interactions. By understanding this, we would be able to answer difficult ques-
 292 tions; How did the universe begin? What is the invisible force (dark matter, dark
 293 energy) pushing the galaxies apart from each other? Where does mass come from?
 294 Why is there almost no antimatter in the universe? In this effort, scientists have
 295 formed several theories. One of them, the Standard Model of particles, is currently
 296 the best theory to describe the visible universe.

297 **The Standard Model** (SM) is a physics theory developed in the 1970's [37]. It
 298 was designed to explain the current experimental results. As such, it was also able to
 299 predict new discoveries and was a driving force for the scientists to invest time and
 300 money in developing new experiments. To date, it is by far the most established and
 301 verified physics theory. It explains how the basic building blocks of matter – *fermions*
 302 – interact with each other via mediators of interactions called *bosons*. There are two
 303 main families of fermions - *quarks* and *leptons*, as shown in diagram 1.21. Each group
 304 consists of six members divided into three *generations*, the first being the lightest and
 305 most stable and the last the heaviest – unstable. The nature around us is made up
 306 of the stable particles – those from the second or third generations can only be found

- 307 in cosmic rays or produced artificially using particle accelerators.
- 308 Quarks have a spin of 1/2 and a charge of either +2/3 (up, charm, top) or -1/3
309 (down, strange, bottom) while the leptons have a spin of 1/2 and a charge of either 1
310 (electron, muon, tau) or 0 (electron neutrino, muon neutrino, tau neutrino). Leptons
311 only exist individually – they do not cluster. Quarks, however, immediately form a
312 cluster of either two (unstable), three (more stable) or five (unstable). Two up and
313 one down quark make up a proton whereas two down and one up quark make up a
314 neutron.
- 315 In addition to fermions, each particle has its corresponding antiparticle – a particle
316 with the same mass but the opposite charge. If an antiparticle hits a particle, they
317 annihilate each other, producing energy in form of photons.
- 318 Bosons are the carriers of force, mediating weak (W^+ , W^- and Z bosons), strong
319 (gluons) and electromagnetic (photons) interactions. The weak interaction is respons-
320 sible for the radioactive decay of subatomic particles, thus playing an essential role in
321 nuclear fission – a process taking place in the stars. The electromagnetic interaction
322 works at a macroscopic level – it allows particles to interact via electric and magnetic
323 fields. The strong interaction is effective at distances of a femtometer and it governs
324 how quarks interact and bind with each other. An additional boson is the Higgs
325 boson and was discovered at CERN in 2012 []. It is a representation of the Higgs
326 mechanism, which gives rise to the mass (or lack thereof) of all the particles in the
327 Standard Model.

328 1.1.1 CERN

- 329 CERN (European Centre for Nuclear Research) [6] is a nuclear research institute
330 housing the largest particle physics laboratory in the world. It straddles the Swiss-
331 French border just outside Geneva. It was established in 1954 to bring the war-torn
332 Europe together by means of fundamental scientific research. Today, it has 22 mem-
333 ber state countries and several observer states. More than 10000 scientists, engineers,
334 technicians, students and others from all around the globe work at CERN on many
335 projects in research fields ranging from particle to nuclear physics. The scope is to
336 probe the fundamental structure of the universe and to understand the mechanisms
337 governing it. Therefore CERN’s main function is to provide the infrastructure for
338 high-energy physics experiments. These are carried out using large machines called
339 particle accelerators. These instruments boost beams of particles to high energies
340 before making them collide with each other or with stationary targets. The result-
341 ing collisions are recorded by particle detectors and later analysed by physicists. To
342 carry out research on the smallest constituents of matter, their dynamics and struc-
343 ture, very high energies are needed. This is why the most powerful accelerators are
344 used for fundamental research. The largest accelerators at CERN are the Proton
345 Synchrotron [], the Super Proton Synchrotron [36] and the Large Hadron Collider [].

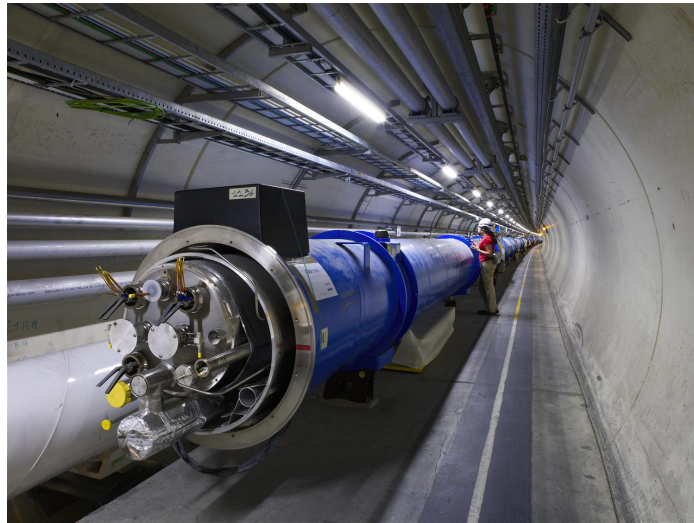


Figure 1.2: The Large Hadron Collider [20]

³⁴⁶ **1.1.2 Particle accelerators**

³⁴⁷ A particle accelerator is a machine that accelerates beams of charged particles like
³⁴⁸ protons, electrons, ions etc. It generates electric fields that add kinetic energy to the
³⁴⁹ particles, speeding them up. It then uses magnets to retain them within a defined
³⁵⁰ trajectory and inside the evacuated beam pipe. The trajectory can be either linear
³⁵¹ (linear accelerators) or circular (circular or cyclic accelerators). The advantage of the
³⁵² latter ones is that they can accelerate particles many times while keeping them in
³⁵³ orbit.

³⁵⁴ Particle accelerators are used in numerous fields ranging from fundamental and
³⁵⁵ material research, cancer treatment to industrial applications, such as biomedicine
³⁵⁶ and material processing. There are several types of accelerators existing: electro-
³⁵⁷ static accelerators, linear accelerators (LINACs), cyclotrons, synrocyclotrons, syn-
³⁵⁸ chrotrons, synchrotron radiation sources and fixed-field alternating gradient acceler-
³⁵⁹ ators (FFAGs).

³⁶⁰ **The Large Hadron Collider** (LHC, figure 1.2) at CERN is the largest particle
³⁶¹ collider in the world. It is a 27 km long circular machine set up in a tunnel deep under
³⁶² the surface (ranging from 50 to 175 m). It accelerates two proton beams to the energy
³⁶³ of 6.5 TeV per beam before it makes them to collide with each other at four different
³⁶⁴ points around its circumference. The LHC was build between 1998 and 2008 and was
³⁶⁵ first successfully started in 2010 and operated stably until 2013 when it underwent a
³⁶⁶ two years long upgrade. They restarted its operation at the beginning of 2015. The
³⁶⁷ hair-thin particle beams travel inside two evacuated pipes with a ~5 cm radius. Coils
³⁶⁸ made up of a superconductive material are wound up around the pipes in special
³⁶⁹ patterns. When they are cooled down to -271 °C using liquid helium, they become
³⁷⁰ superconductive - the resistivity of the material drops significantly, minimising the
³⁷¹ heat dissipation despite high electric currents. These produce strong magnetic fields

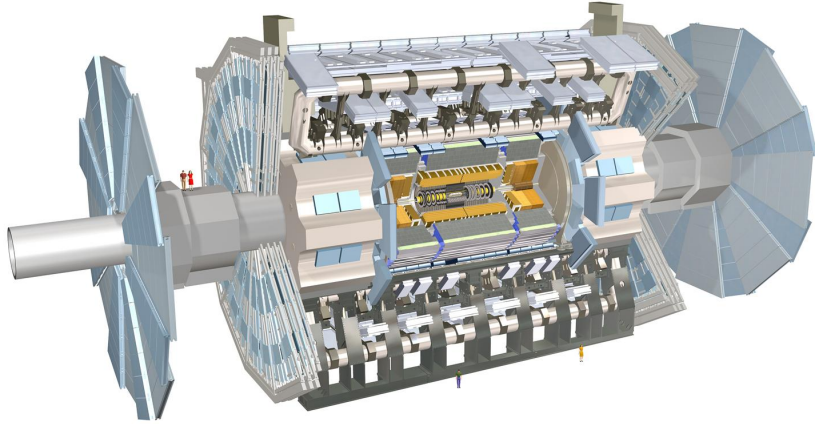


Figure 1.3: The ATLAS Experiment [38]

which bend the particles and keep them in a circular trajectory. The particles are accelerated when traversing the radiofrequency (RF) cavities with the RF frequency of 400 MHz. This oscillating frequency creates buckets – compartments for bunches of highly energetic particles – which are 2.5 ns long. Only one out of ten buckets is being filled, so the bunches are spaced at 25 ns. This defines the machine’s clock as well as the maximum rate of collisions - the bunches travelling in the opposite direction will cross at the intersections up to 40 million times per second. Currently around 20 collisions occur during every bunch crossing, making the maximum collision rate of 10^9 per second. The number of collisions will further increase in the next years, when they will increase the number of particles in every bunch and decrease the transverse spread of the bunches – squeeze them, therefore increase their density and the collision probability.

1.1.3 The ATLAS experiment

ATLAS (short for A Toroidal Lhc ApparatuS, figure 1.3) [] is a particle physics experiment at CERN. Its purpose is to verify current theories and search for new discoveries by observing and analysing high energy proton-proton collisions produced by the LHC. It is the biggest experiment at CERN by dimensions (45 m in length and 26 m in height) and the number of people involved (more than 3000 physicists and engineers). The ATLAS detector consists of many detectors, each designed to measure a specific property of the particles and photons produced during the collision. The closest to the collision point is the Inner Detector (ID), which consists of several layers of highly spatially segmented semiconductor sensors. These can record the path of the individual particles and photons. In addition, a strong magnetic field of 2 T curves the

1.1. FUNDAMENTAL RESEARCH

paths of the charged particles, which in turn allows the ID to identify an individual particle's charge and momentum. The next two parts are the electromagnetic and tile calorimeter. These detectors weigh a few thousand tonnes and measure the energy of the particles that are stopping in the bulk. The only particles that make it through the calorimeters are muons. These are detected by the Muon Spectrometer, a set of large plates placed all around the inner layers. Last is the superconductive magnet, which provides the magnetic field through the whole of ATLAS except the ID, which already has its own magnets. To sum up, the Inner Detector measures the charge and momenta of the particles and photons, the calorimeters measure their energies, the Muon Spectrometer measures muons and the magnets provide magnetic fields, which curve the trajectories of the charged particles, facilitating the charge and momentum measurements.

A complex Trigger and Data Acquisition system (TDAQ) is in place to distribute the clock signal, configure the detectors, trigger them and handle the output data. They are then stored at the CERN computer centre and distributed across the globe by means of the GRID – a cloud-like distributed data system.

The ATLAS detector has been designed to measure every collision taking place in its core. With 25 ns between collisions, this makes up 40 million collisions per second. In reality, the maximum achievable rate is about 300 kHz. The recorded collision is called an event. Every event holds information from all the detector channels within ATLAS. With $\sim 10^6$ channels, an event size is approximately 10 MB. At the maximum achievable rate this means a data rate of up to 3 TB/s. Unfortunately no supercomputer existing today is capable of reading in and saving such a huge amount of data. This is where the trigger logic comes into play. It is programmed to decide in the order of tens of nanoseconds after an event whether this is a potentially interesting event or not. If so, it triggers the readout of the whole detector. This way, the recorded event rate is reduced from 300 kHz to ~ 500 Hz, which is already within the limits of the computing centre's capabilities.

1.1.4 Atominstitut, Vienna

Atominstitut (ATI) [2], an institute for atomic and subatomic physics, was established in 1958 in Vienna as an inter-university institute. It currently houses around 200 people involved in a broad range of research fields: quantum, particle, neutron, nuclear, radiation and reactor physics, quantum optics etc. Its central facility is a TRIGA MARK II neutron reactor (described in detail below).

As of 2002 the ATI is part of the University of Technology in Vienna.

TRIGA MARK II neutron reactor [12] is a reactor of a swimming-pool type used for training, research and isotope production. It is one of 40 such reactors worldwide, produced by an californian company General Atomic in the early 60's. It is capable of continuous operation at a maximum output power of 250 kW. The reactor core consists of 3 kg of 20 % enriched uranium (^{235}U). The fuel moderator rods are mostly made up of zirconium with low percentage of hydrogen and uranium. Both the

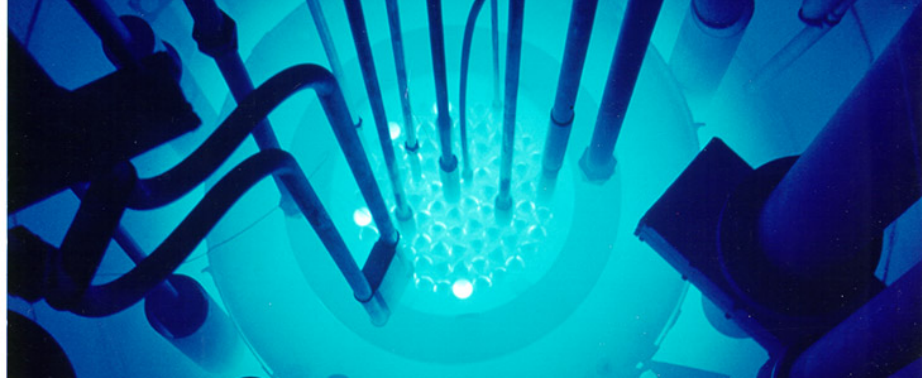


Figure 1.4: The TRIGA MARK II neutron reactor [15]

436 core and the rods are immersed in a pool of water as shown in figure 1.4 for the purpose
437 of cooling and radiation protection. The surrounding concrete walls are 2 m wide
438 with an added graphite layer for improved shielding. Four main experimental beam
439 holes are placed radially through the walls. All exits are heavily shielded to prevent
440 radiation damage to people, but still leaving enough space to set up experiments.
441 Apart from the beam holes, there are several other exits and components, e.g. a
442 thermal column for generation of thermal (low energetic) neutrons.

443 1.1.5 n-ToF

444 n-ToF (or neutron time-of-flight) [9] is a scientific collaboration with the aim of study-
445 ing neutron-nucleus interactions. Over 30 institutes and universities are currently
446 active members of this collaboration, among them Atominstitut in Vienna. n-ToF
447 is also a facility at CERN where the experiments are carried out in a 200 m long
448 experimental area. The knowledge stemming from the experimental results can then
449 be applied in various fields ranging from nuclear technology and cancer therapy to
450 astrophysics.

451 A pulsed beam of highly energetic protons (20 GeV/c) is produced by the Proton
452 Synchrotron (PS) and aimed at a fixed lead spallation target. Each proton hitting
453 the target produces around 300 neutrons of various energies. Initially highly energetic
454 neutrons are slowed down by the target and by a slab of water placed behind it. This
455 broadens their energy spectrum, which then ranges from meV (thermal neutrons) to
456 GeV (fast neutrons). The neutrons are then collimated and sent through a 185 m
457 long evacuated pipe to the experimental area, where they are made to collide with
458 another target or a sample. The radiation resulting from the collisions is detected by
459 a set of dedicated detectors around the interaction point (seen in figure 1.5). Having
460 different energies, neutrons travel with different speeds, highly energetic ones reaching
461 the target faster than those with low energies. Analysis of the collisions with a precise
462 timing allows us to determine the interaction probability with sample material as a
463 function of incident neutron energy.

1.2. PARTICLE DETECTORS

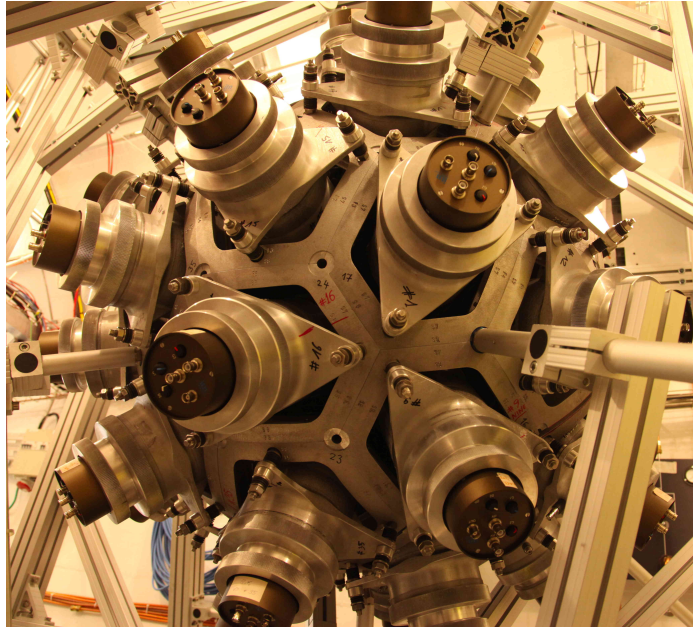


Figure 1.5: The calorimeter in the n-ToF area [19]

1.2 Particle detectors

Particle detectors, or radiation detectors, have first come into use at the end of the 19th century. At that time Wilhelm Röntgen used a photographic plate onto which he shone X-rays. Soon after, in 1912, Victor F. Hess discovered cosmic rays during a balloon flight. This paved the way for development of particle detectors. A cloud chamber was designed – a chamber filled with a supersaturated vapour of water or alcohol. If a highly energetic particle traversed the chamber, the mixture ionised, creating condensation nuclei. These traces were visible and were photographed. All the subsequent particle detectors relied on the same principle of interaction between the particles – ionisation. The bubble chamber invented in 1952 used a superheated transparent liquid – a liquid heated just below its boiling point. A particle ionised the liquid, forming microscopic bubbles along its trajectory. Then followed the spark chamber and the wire chamber where the particle ionised the gas, causing a spark between two parallel plates at a high potential difference. These are nowadays used in museums as showcases. Next were ionisation chambers, which measured the induced current of the free ionised charges moving in an externally applied electric field. Finally in the 1960s, semiconductor detectors were introduced. Their principle of operation is similar to that of an ionisation chamber, with the difference that a semi-conductive material is used as an ionisation medium instead of gas. Every technology has its advantages and disadvantages. Nowadays an ensemble of several types of detectors is used as a single detector system. There are many considerations that need to be taken into account when designing such a system: detector geometry, segmentation, event rate, efficiency, readout, support structures, cabling, cooling, cost etc.

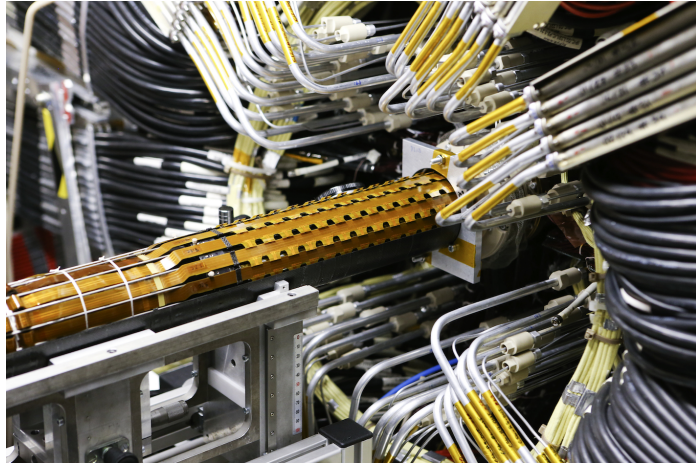


Figure 1.6: The Insertable B-Layer – a silicon particle tracker installed in the ATLAS experiment in 2014 [34]

On large, particle detectors can be divided in two groups: tracking detectors and calorimeters. The former are designed to measure trajectories (momentum) of particles and photons with a minimal impact on their flight path or energy. They must be built with a high spatial resolution and lightweight. Typically they are semiconductor detectors. The calorimeters, on the other hand, measure the energy of the particles/photons by stopping them. This means they need to be heavy and dense. A typical physics experiment nowadays would consist of a tracking detector enclosed by a calorimeter. This way both the momentum and energy are derived, measuring energy, charge and trajectory of every particle/photon.

1.2.1 Semiconductor detectors

Semiconductor particle detectors are devices that use a semiconductor for detecting radiation. They work on the principle of an ionisation chamber. An incident particle or a photon ionises the atoms in the crystal lattice. The freed charges start drifting in an externally applied electric field, inducing current on the electrodes. The charges are freed if the deposited energy is higher than the energy band gap. There are many semiconductor materials currently existing, each with a different band gap. Germanium (Ge), for instance, has a band gap of 0.67 eV, which means that most of the electrons at the room temperature will already be in an excited state. Diamond's 5.5 eV band gap, on the other hand, is too high for the visible light to excite the electrons. Silicon with an energy gap of 1.12 eV has been the material of choice for the majority of semiconductor applications, including radiation detectors. Semiconductor detectors are most widely used for tracking applications, like the Insertable B-Layer (see figure 1.6) [39], which was installed in ATLAS Experiment in 2014. They can be produced into light and thin sensors, they have a fast signal response, they are highly efficient and highly resistant to radiation damage. They also allow for a fine spatial segmentation to increase the tracking resolution. Semiconductor sensors come

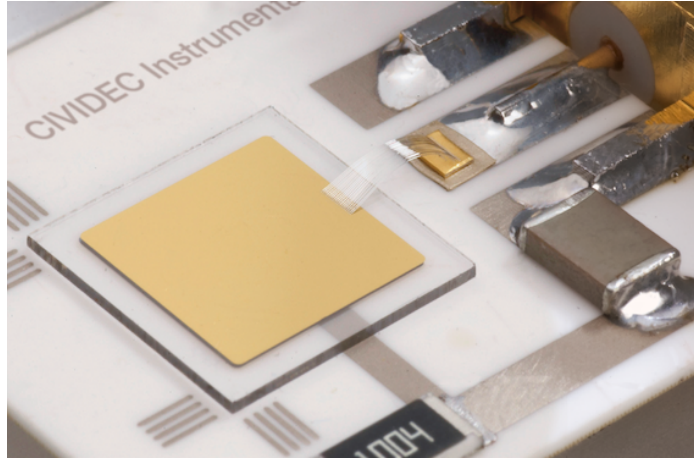


Figure 1.7: A pCVD diamond pad detector [23]

in several configurations. The simplest type is a pad – a single plate measuring 25 mm². Pads are used for particle counting and radiation monitoring. Next is a strip detector, a more finely segmented detector made out of long parallel sensing areas or strips. Each strip has its own signal line for readout. Usually the strip detectors are used in pairs – one detector is placed on top of the other at a 90° angle to increase spatial resolution in both axes. The third and the most finely segmented is a pixel detector, consisting of a 2D array of independent sensing areas. In tracking applications, pixel detectors are used where the detection resolution is the highest. Due to their high production cost and a high number of signal channels, they can only cover limited areas. Strip detectors are cheaper to produce and can be used to cover larger areas in several consecutive layers.

1.2.2 Diamond sensors

Diamond has been known for over two millennia, valued for its mechanical properties and its appearance. When we learnt how to synthesise it, diamond found its way to a broad range of industries which exploited its optical and electrical properties. The discovery of the Chemical Vapour Deposition (described below) as a new synthesis process gave rise to a range of new applications. From being used on machines for drilling tunnels it found its way to electronics, high-power switching devices, electrochemical systems, radiation sensors, quantum computing etc. Recently it was found that it also exhibits superconductivity. This thesis focuses on the use of diamond for radiation detection. Compared to a natural diamond, a detector-grade CVD diamond has almost no impurities (foreign atoms like nitrogen or boron). The carbon lattice is very uniform, which improves its electrical properties. It is an almost perfect insulator, but behaves as a semiconductor under certain conditions. Compared to silicon, the most widely used semiconductor material for radiation detection, it has many advantages, which are described in detail in chapter ???. Figure 1.7 shows a diamond pad detector produced by CIVIDEC Instrumentation GmbH.

541 **Chemical vapour deposition** (CVD) [] is a process where a material is deposited
542 from a gas onto a substrate, involving chemical reactions. It is often carried out un-
543 der high pressure and high temperatures. It takes place in enclosed chambers called
544 furnaces with careful regulation of the temperature, pressure and gas mixture. Syn-
545 thetic diamond is grown at 700–900 °C with a mixture of hydrogen and methane
546 gas. At this temperature the molecules dissociate into carbon and hydrogen atoms.
547 The carbon atoms are the building blocks and are deposited on the surface of the
548 substrate. However, they would rather form graphitic bonds as they are more stable
549 than diamond bonds. Nevertheless, with high pressure, high temperature and with
550 added abrasive atomic hydrogen, the graphitic double bonds are broken up and con-
551 verted into diamond bonds. The speed of the growth can be anywhere between 0.1
552 and 10 micron per hour. The detector grade samples are grown at a rate of the order
553 of 1 micron per hour. They can grow up to several millimetres in thickness. Their
554 width, however, depends entirely on the substrate used. Diamond can be deposited
555 on various materials: diamond, silicon, tungsten, quartz glass etc. The substrate
556 material must be able to withstand the high temperatures during the CVD process.
557 The diamond substrate does not need any surface pre-treatment. Carbon atoms form
558 bonds with atoms in the existing crystal structure. This is the homoepitaxial growth
559 where the newly deposited atoms retain the orientation of the structure in the sub-
560 strate. Other non-diamond substrates, however, need to be pre-treated, usually by
561 being polished using diamond powder. Some powder particles remain on the surface,
562 acting as seeds for the growth of small crystals or grains. These grains grow and
563 at some point merge with the adjacent ones, making up a compact material. The
564 lower side is later polished away. These diamonds are called *polycrystalline* (pCVD)
565 whereas those grown on a diamond substrate are *single crystal* (sCVD) diamonds.
566 The area of the former can be large - up to 0.5 m² or more compact 15 cm² in the case
567 of detector grade diamonds. The sCVD diamonds, on the other hand, can currently
568 only measure up to 1.5 cm².

569 **Chapter 2**

570 **Signal formation in diamond**

571 This chapter describes the fundamentals of signal formation in a diamond sensor, as
572 well as its use as a particle detector. This is described in section 1.1 where energy
573 deposition and signal formation mechanism are explained. Then some examples of
574 ionisation are shown. Later, some of the internal lattice defects that effect the signal
575 are described. The final section contains the description of the remaining part of the
576 signal chain – signal amplifiers, digitisers and devices for signal processing. Noise
577 contributions are discussed at every stage of the signal chain.

578 There are many types of radiation sensors existing, but in this chapter we will
579 focus on semiconductors, in particular on diamond sensors. Diamond is a good insu-
580 lator, but behaves as a semiconductor in certain cases. In fact, the main principle of
581 operation is the same for diamond, silicon and other semiconducting materials – ion-
582 isation. An incident highly energetic charged particle ionises the atoms in the lattice,
583 freeing electrons and holes, which then drift towards positively and negatively charged
584 electrodes, inducing an electrical signal. A sensor converts the energy deposited by a
585 particle or a photon to an electrical signal.

586 Silicon is currently considered as the industry standard for particle detection.
587 However, there are some disadvantages of using silicon instead of diamond, due to
588 significant differences in the material properties. In particular, the properties of silicon
589 change significantly with radiation. For instance, the leakage current increases, which
590 in turn increases shot noise and can lead to a thermal runaway. In addition, due to
591 induced lattice defects, which act as charge traps, its charge collection efficiency starts
592 dropping quickly. Both are true for diamond as well, but on a much smaller scale.

593 Table 1.2 compares the properties of diamond and silicon. Some of these values
594 will be revisited and used in the course of this thesis.

Property	Diamond	Silicon
Band gap energy E_g (eV)	5.5	1.12
Electron mobility μ_e ($\text{cm}^2 \text{ V}^{-1} \text{ s}^{-1}$)	1800	1350
Hole mobility μ_h ($\text{cm}^2 \text{ V}^{-1} \text{ s}^{-1}$)	1200	450
Breakdown field (V cm^{-1})	10^7	3×10^5
Resistivity ($\Omega \text{ cm}$)	$> 10^{11}$	2.3×10^5
Intrinsic carrier density (cm^{-3})	$< 10^3$	1.5×10^{10}
Mass density (g cm^{-3})	3.52	2.33
Atomic charge	6	14
Dielectric constant ϵ	5.7	11.9
Displacement energy (eV/atom)	43	13 – 20
Energy to create an e-h pair (eV)	13	3.6
Radiation length (cm)	12.2	9.6
Avg. signal created/ μm (e)	36	89

595

596

Table 2.1: Comparison diamond – silicon []

597

598

2.1 Principles of signal formation in semiconductors

599 There are several ways the particles can interact with the sensor: via bremsstrahlung [],
 600 elastic or inelastic scattering (e-h pair production). Bremsstrahlung is radiation cre-
 601 ated when a particle is deflected from its original path due to attraction of the core of
 602 an atom. This is in principle an unwanted effect in semiconductors as it decreases the
 603 spatial resolution of the sensor. Elastic scattering is deflection of the particle's tra-
 604 jectory without energy loss. Inelastic scattering is the interaction through which the
 605 atom is ionised and an electron-hole pair is created. All these effects are competing
 606 and are dependent on the particle's mass, momentum etc.

607 Semiconductors are materials that are conductive only under specific
 608 conditions. They can be made up of atoms with four electrons in their valence band
 609 (e.g. silicon–Si, carbon–C or germanium–Ge) or as combinations of two or more
 610 different materials (e.g. gallium arsenide–GaAs). The atoms in the lattice form
 611 valence bonds with adjacent atoms, making solid crystal structures. These bonds
 612 can break up if sufficient external energy is applied. The electron that was forming
 613 the bond is kicked out, leaving behind a positively charged ion with a vacancy in its
 614 valence band (see figure 1.1a). A free electron-hole pair is thus created. The free
 615 electron travels through the crystal until it is caught by another hole. Similarly, the
 616 hole also “travels” through the material. Its positive charge attracts a bound electron
 617 in the vicinity, which breaks from the current bond and moves to the vacancy, leaving
 618 a new hole behind. The process continues, making it look like the vacancy – the hole
 619 – is traveling through the material.

620 The electrons need to absorb a certain energy to get kicked out of the atomic
 621 bond – to get ionised. The minimal energy required to excite (ionise) an electron in
 622 a semiconductor is equal to the energy gap E_g . Typical widths of the forbidden gap
 623 are 0.7 eV in Ge, 1.12 eV in Si, 1.4 eV in GaAs and 5.5 eV in Di. Due to the small

2.1. PRINCIPLES OF SIGNAL FORMATION IN SEMICONDUCTORS

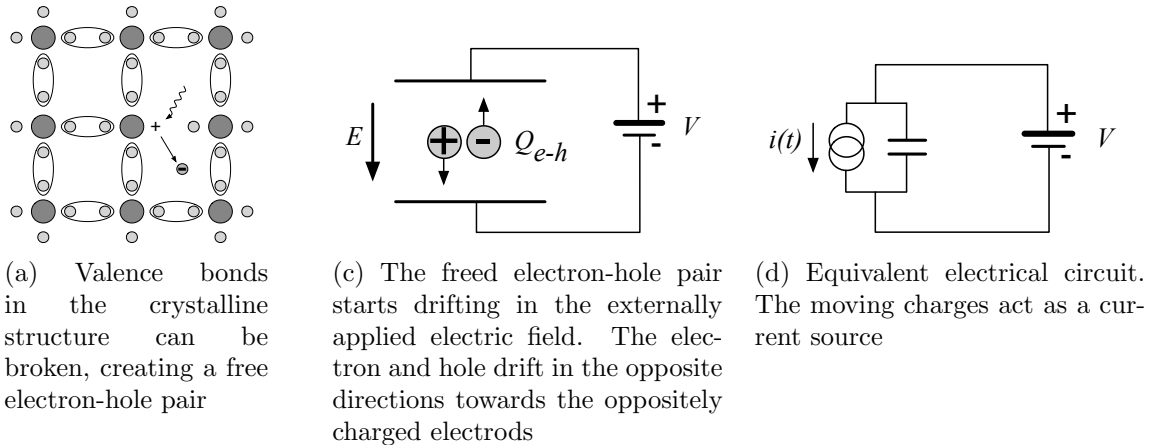


Figure 2.1: In the equivalent electrical circuit diagram, electron-hole creation and drift can be modelled as a current source with a capacitor in parallel

624 band gap in semiconductors some electrons already occupy the conduction band at
 625 room temperature (RT). The intrinsic carrier concentration n_i in semiconductors is
 626 given as

$$n_i = T^{3/2} \cdot \exp\left(-\frac{E_g}{2kT}\right) \quad (2.1)$$

627 wherein $k = 1.381 \times 10^{-23} \text{ m}^2 \text{ kg s}^{-2} \text{ K}^{-1}$ is the Boltzmann constant and T is the
 628 temperature.

629 If an external electric field is applied to the crystalline structure, the free elec-
 630 trons and holes drift toward the positive and negative potential, respectively (see
 631 figure 1.1c). While drifting, the charges couple with the electrodes, inducing cur-
 632 rent in the circuit, which is explained by the Shockley–Ramo theorem (see subsection
 633 below). The charges recombine upon reaching the electrodes.

634 Energy deposition of α radiation and heavy ions

635 **Energy deposition of β and γ radiation** The mean energy loss of a particle travers-
 636 ing the detector with respect to its momentum is given with the the Bethe-Bloch
 637 equation []:

$$-\left\langle \frac{dE}{dx} \right\rangle = \frac{4\pi}{m_e c^2} \cdot \frac{n z^2}{\beta^2} \cdot \left(\frac{e^2}{4\pi\epsilon_0} \right)^2 \cdot \left[\ln \left(\frac{2m_e c^2 \beta^2}{I \cdot (1 - \beta^2)} \right) - \beta^2 \right] \quad (2.2)$$

638 The resulting function for a muon (a heavy electron) is shown in figure 1.2. At the
 639 momentum of around 300 MeV/c the particle deposits the lowest amount of energy.
 640 That is called a minimum ionising particle or a MIP.

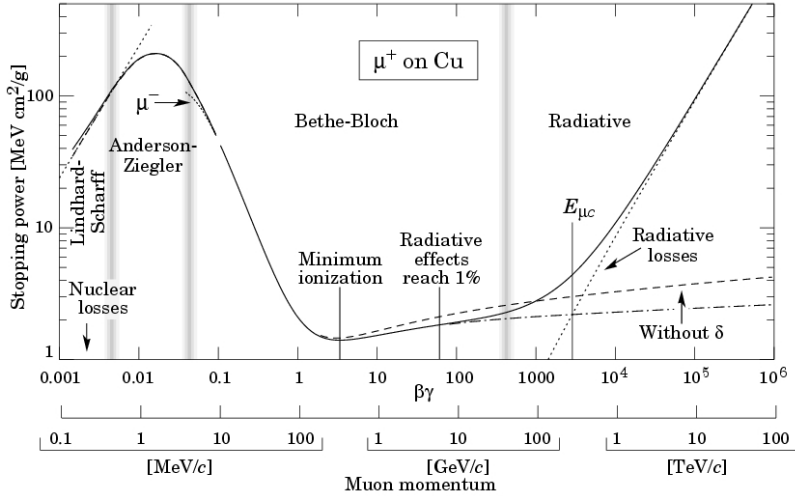
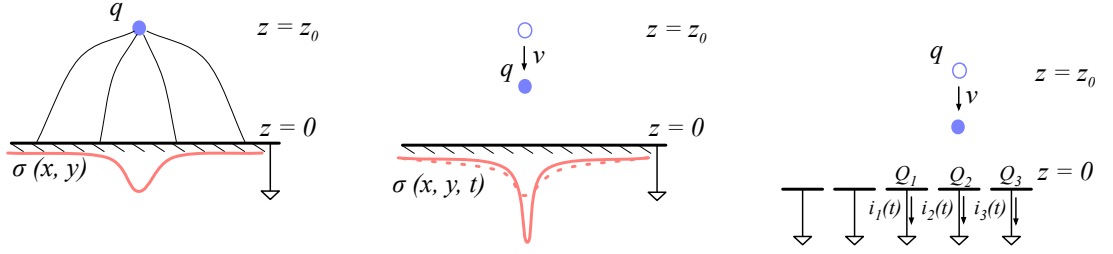


Figure 2.2: Stopping power for muons according to the Bethe-Bloch formula []



(a) Newly created point charge couples with the conductive plane
 (b) When the charge drifts, the charge density in the plane changes
 (c) The changing charge density in the small regions of the plane induces current

Figure 2.3: A point-like charge inducing current in a conductive plane

2.1.1 Signal induction by moving charges

The book [17] gives a simple introduction to understanding signal induction in a conducting plane by a point-like charge. The idea behind it lies in the coupling of the charge with the electrode. The electrode can be in this case modelled as an infinite conducting plane. When the point charge q is created (e.g. an electron-hole pair created via ionisation), its electrostatic field lines immediately couple with the electrode, as seen in figure 1.3a. The electric field on the metal surface due to a point-like charge q at the distance z_0 equals

$$E_z(x, y) = \frac{qz_0}{2\pi\epsilon_0(x^2 + y^2 + z_0^2)^{\frac{3}{2}}} \quad E_y = E_z = 0. \quad (2.3)$$

A mirror charge appears on the conducting plane, with a charge density distribution

$$\sigma(x, y) = \epsilon_0 E_z(x, y) = \frac{qz_0}{2\pi(x^2 + y^2 + z_0^2)^{\frac{3}{2}}}. \quad (2.4)$$

2.1. PRINCIPLES OF SIGNAL FORMATION IN SEMICONDUCTORS

650 The charge density integrated over the whole plane gives the mirror charge Q , which
651 has the opposite value of the point charge q :

$$Q = \int_{-\infty}^{\infty} \int_{-\infty}^{\infty} \sigma(x, y) dx dy = -q. \quad (2.5)$$

652 Now we segment the plane into infinitely long strips with a width w whereby each
653 of the strips is grounded (figure 1.3c). With the charge density distribution 1.4, the
654 resulting mirror charge on a single strip Q_2 directly below the point charge ($x =$
655 $0, y = 0$) will be equal to

$$Q_2(z_0) = \int_{-\infty}^{\infty} \int_{-w/2}^{w/2} \sigma(x, y) dx dy = -\frac{2q}{\pi} \arctan\left(\frac{w}{2z_0}\right) \quad (2.6)$$

656 If the charge starts moving towards the conducting plane, the mirror charge density
657 distribution also changes (see figure 1.3b). This results in the $Q_2[z_0(t)]$ to change
658 with time, inducing an electric current $i_n(t)$:

$$i_n(t) = -\frac{d}{dt} Q_2[z_0(t)] = -\frac{\partial Q_2[z_0(t)]}{\partial z_0} \frac{\partial z_0(t)}{\partial t} = \frac{4qw}{\pi[4z_0(t)^2 + w^2]} v. \quad (2.7)$$

659 The movement of the point-like charge therefore induces current in the conducting
660 plane. The induced current is linearly dependent on the velocity of the point-like
661 charge.

662 W. Shockley [42] and S. Ramo [40] independently proposed a theory which explains
663 how a moving point charge induces current in a conductor. The Shockley-Ramo
664 theorem can therefore be used to calculate the instantaneous electric current induced
665 by the charge carrier or a group of charge carriers. It can be used for any number of
666 electrodes. It states that the current $I_n^{\text{ind}}(t)$ induced on the grounded electrode n by
667 a point charge q moving along a trajectory $\mathbf{x}(t)$ equals

$$I_n^{\text{ind}}(t) = -\frac{dQ_n(t)}{dt} = -\frac{q}{V_w} \nabla \Psi_n[\mathbf{x}(t)] v(t) = -\frac{q}{V_w} E_n[\mathbf{x}(t)] v(t), \quad (2.8)$$

668 where $\mathbf{E}_n(\mathbf{x})$ is the electric field in the case where the charge q is removed, electrode n
669 is set to voltage $V_w = 1$ and all other electrodes are grounded. $\mathbf{E}_n(\mathbf{x})$ is also called the
670 *weighting field* of electrode n and is defined as the spatial differential of the *weighting*
671 *potential*: $\mathbf{E}_n(\mathbf{x}) = \nabla \Psi_n(\mathbf{x})$. In the case of two parallel electrodes, the weighting field
672 is $E_w = -\frac{d\Psi}{dx} = -1/d$, where d is the distance between the electrodes. The resulting
673 induced current is therefore

$$i(t) = \frac{q}{d} v_{\text{drift}}(x, t), \quad (2.9)$$

674 whereby v_{drift} is the drift velocity of the point-like charge and d is the distance between
675 the electrodes.

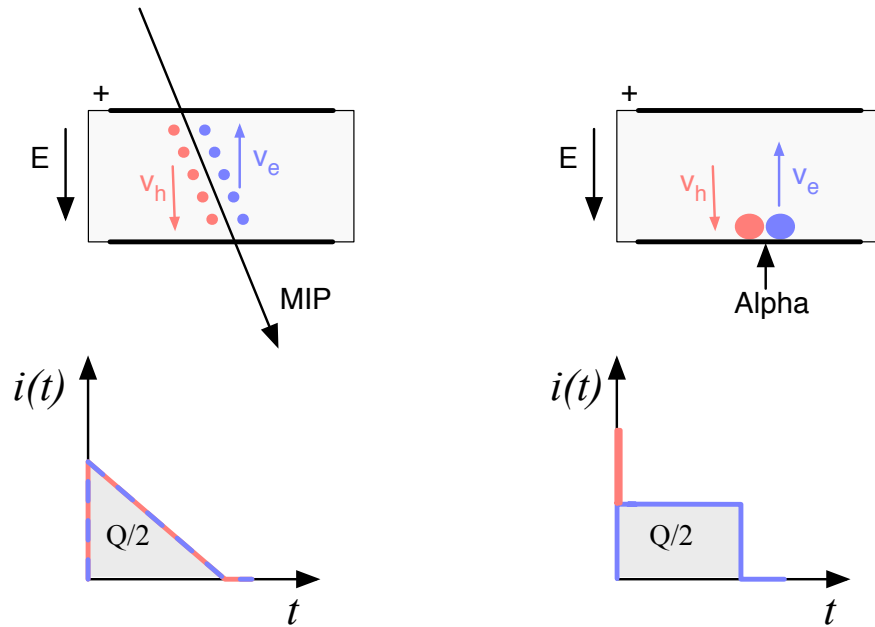


Figure 2.4: Charge carrier drift in diamond for β/γ and for α particles

676 2.1.2 Radiation-induced electrical pulses

677 When a highly-energetic particle travels through the sensor, it interacts with atoms
 678 in the lattice. It ionises the valence electrons, creating electron-hole (e-h) pairs on its
 679 way. It can either deposit only a fraction of its energy and fly exit the sensor on the
 680 other side or it can get stopped in the bulk, depositing all of its energy. A special
 681 case is when it interacts with the core of the atom in the middle of the sensor via
 682 a nuclear interaction. All these various types interactions produce different amounts
 683 and different spatial distributions of e-h pairs. The induced electrical current will
 684 therefore differ for different types of interaction. Two most frequent types are shown
 685 in figure 1.4. The first diagram shows the interaction of a minimum ionising particle
 686 (an electron or a proton) or in some cases a photon, if it is energetic enough. The
 687 electrons and holes are created all along the trajectory of the particle and imme-
 688 diately start drifting towards the positive and negative electrode, respectively. At
 689 the beginning, all charges drift and contribute to the induced current. Those closest
 690 to the electrodes have a very short drift path and recombine quickly, reducing the
 691 induced current. Gradually all the charge carriers recombine. The resulting current
 692 signal is a triangular pulse with a sharp rising edge and a linear falling edge. The
 693 accumulated charge Q_s equals to the sum of the contributions of the positive and
 694 negative charge carriers. The second type of interaction happens when the particle
 695 is stopped in the diamond close to the point of entry. Most of its energy is deposited
 696 in a small volume close to the electrode. A cloud of charge carriers is created and
 697 the charges with the shorter path to the electrode recombine almost instantly. The

2.2. CARRIER TRANSPORT IN A DIAMOND SENSOR

carriers of the opposite charge, however, start drifting through the sensor to the other electrode. In an ideal diamond sensor, their velocity is constant throughout the drift up until they recombine on the other side. The contribution of the first charge cloud is a peak with a short time. The cloud drifting through the sensor, on the other hand, induces a current signal with a flat top. The resulting signal has a shape of a rectangle, with a spike in the beginning. This spike is filtered out in a real device because it is too fast for the electronics existing currently. The accumulated charge Q_s is equal to a half of the deposited charge by the stopped particle.

The two aforementioned types of interactions have well defined signal responses. Nuclear interactions on the other hand yield various results. The resulting signal shape depends on the decay products of the interaction – they can be α , β or γ quanta, inducing a mixed shaped signal.

2.1.3 Signal charge fluctuations

Two of the important sensor characteristics are the magnitude of the signal and the fluctuations of the signal at a given absorbed energy. They determine the relative resolution $\Delta E/E$. For semiconductors the signal fluctuations are smaller than the simple statistical variance $\sigma_Q = \sqrt{N_Q}$, where N_Q is the number of released charge pairs (ratio between the total deposited energy E_0 and the average energy deposition E_i required to produce an electron-hole pair). [2] shows that the variance is $\sigma_Q = \sqrt{FN_Q}$, where F is the Fano factor [2] (0.08 for diamond and 0.115 for silicon [2]). Thus, the variance of the signal charge is smaller than expected, $\sigma_Q \approx 0.3\sqrt{N_Q}$. The resulting intrinsic resolution of semiconductor detectors is

$$\Delta E_{FWHM} = 2.35\sqrt{FEE_i} \quad (2.10)$$

wherein $E_i(Si) = 3.6$ eV and $E_i(C) = 13$ eV. E.g., for an α particle with energy $E_\alpha = 5.486$ MeV the calculated resolution in diamond is equal to $\Delta E_{FWHM} = 5.6$ keV. This defines the maximum achievable resolution for energy spectroscopy with semiconductors. Figure 1.5 shows the calculated energy resolution function for silicon and diamond.

2.2 Carrier transport in a diamond sensor

This section describes the carrier transport phenomena in diamond. This theory provides the basis for discussion about the measurements in chapter ??.

Free charge carriers in a semiconductor get thermally excited and scatter in random directions with a thermal velocity v_{th} [2]. Their integral movement due to thermal excitation equals zero. Their transport is instead by means of drift and diffusion. Diffusion is caused by the concentration gradient. In its presence the carriers tend to scatter in the direction of the lower concentration. Drift on the other hand is caused by an externally applied electrical field. In that case the carriers move in parallel to

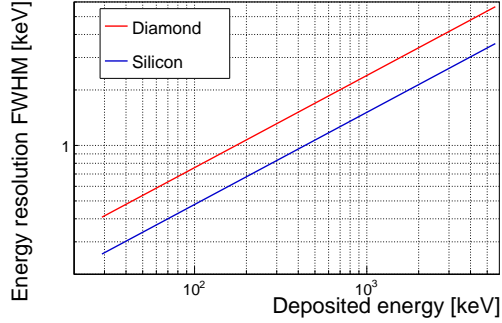


Figure 2.5: Calculated intrinsic energy resolution for silicon and diamond

to the field lines. In a sensor with a high applied field the diffusion contribution is negligible.

Diffusion The concentration profile dissolves with time forming a Gaussian distribution with variance $\sigma(t) = \sqrt{Dt}$ [1].

Drift velocity and mobility The charge carriers drift through the diamond bulk with a drift velocity $v_{\text{drift}}(E)$ [1], which is proportional to the electric field E at low electric fields: $v_{\text{drift}} = \mu E$. The proportionality factor μ is defined as the mobility in $\text{cm}^2\text{V}^{-1}\text{s}^{-1}$. For higher fields, however, the velocity saturates. The final equation for v_{drift} is therefore

$$v_{\text{drift}}(E) = \mu(E)E = \frac{\mu_0 E}{1 + \frac{\mu_0 E}{v_{\text{sat}}}} \quad (2.11)$$

where μ_0 is the low field mobility and v_{sat} is saturation velocity. The drift velocity can be retrieved experimentally via the transit time measured with the Transient Current Technique (TCT). This technique enables the measurement of transit time t_t of the carriers through the sensor with the thickness d .

$$v_{\text{drift}}(E) = \frac{d}{t_t(E)}. \quad (2.12)$$

The velocities for holes and electrons usually differ. In diamond, the holes travel 30 % faster than electrons [1]. The measurements in chapter ?? empirically confirm this statement.

Velocity saturation At higher drift velocities the carriers lose more energy to the lattice. They induce increasingly more lattice vibrations (phonon transport) with increased velocity. There is a velocity limit above which the carriers cannot reach – velocity saturation. Thesis [1] defines this velocity to be $v_{\text{sat}}^e = v_{\text{sat}}^h = (14.23 \pm 0.12) \times 10^6 \text{ cm/s}$ for both positive and negative charge carriers.

Space charge Poisson's equation shows that

$$\frac{d^2\Phi(x)}{dx^2} = \frac{dE(x)}{dx} = \frac{\rho(x)}{\epsilon} \quad (2.13)$$

2.2. CARRIER TRANSPORT IN A DIAMOND SENSOR

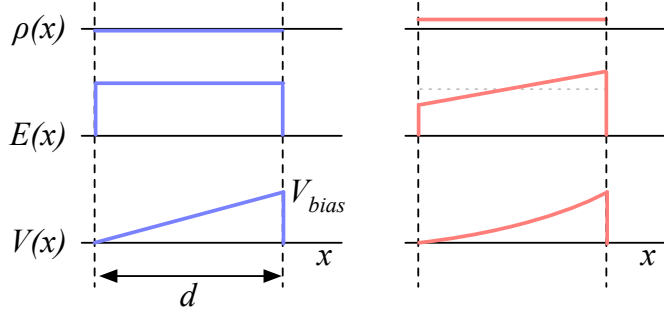


Figure 2.6: Introduction of space charge in the diamond bulk. The induced current signal is proportional to the effective electrical field. d is the thickness of the diamond sensor.

where $\rho(x)$ is the space charge distribution, E is the electrical field and Φ is the voltage potential. In an ideal diamond, the externally applied high voltage potential on the two electrodes decreases linearly through the bulk. The electrical field is therefore constant throughout the sensor and the space charge distribution across it equals 0. However, in some cases space charge is introduced in the bulk, uniformly or non-uniformly. It can do so by means of trapping of charge carriers in the non-uniformities in the lattice or it can already be introduced during the production of the diamond material. The space charge can be either permanent or changing – sometimes it is possible to reduce it by means of priming. All in all, it is very important to reduce it because it affects the shape of the electrical signal. Since the drift velocity of the charge carriers is proportional to the electrical field, the charges change their velocity while drifting through the space charge region. Figure 1.7 compares the voltage potential, electrical field, space charge for an ideal sensor and for that with a uniformly distributed positive space charge.

Radiation damage The diamond crystal lattice is very strong and uniform. However, when the highly energetic particles or photons impinge the diamond, they can damage the crystal structure. Figure ?? shows several examples of the lattice damage:

- a) foreign interstitial (e.g. H, Li),
- b, c) foreign substitutional (e.g. N, P, B),
- d) vacancy and
- e) self interstitial.

These non-uniformities – traps – form new energy levels in the forbidden gap. The drifting charge carriers are stopped by these traps, which in effect reduces the induced current. The energy level of the trapped carrier is reduced from the conduction band to the energy level of the trap. Different types of lattice damage have different energy levels. The release time depends on the level (shallow, deep trap).

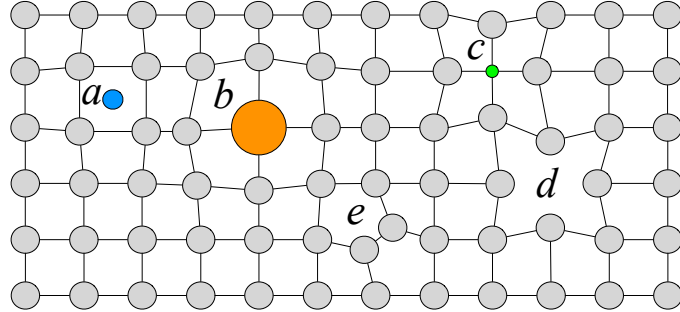


Figure 2.7: Introduction of impurities and non-uniformities into the crystal lattice due to radiation damage.

782 2.3 Electronics for signal processing

783 This section describes the electronics of a detector, starting with a description of
784 signal amplifiers and then discussing the digitisation and signal processing. All these
785 stages are necessary to extract information from the sensor. First, the signal has to be
786 amplified. Then it is digitised and finally processed in a specially designed processor
787 or a logic unit.

788 2.3.1 Signal preamplifiers

789 The signal charge generated in the sensor by a single highly energetic particle or
790 photon is of the order of fC. The induced current is ranging between 10^{-8} A (β, γ
791 radiation) and 3×10^{-7} A (α radiation). Signals as low as these have to be pre-
792 amplified before processing. Depending on the measurement, several types of signal
793 amplifiers can be used. The preamplifiers have to be designed carefully to minimise
794 electronic noise while maximising gain – thus maximising the signal-to-noise ratio
795 (SNR). In addition, they have to have a high bandwidth limit because the signals
796 from the diamond sensors are very short. A critical parameter is the total capaci-
797 tance, i.e. sensor capacitance and input capacitance of the preamplifier. The SNR
798 improves with a lower capacitance. Several types of amplifiers can be used, all of
799 which affect the measured pulse shape. They behave differently for resistive or ca-
800 pacitive sources. Given that semiconductors are capacitive sources, we will focus on
801 these. Two preamplifiers are used most commonly, a current and a charge amplifier.
802 Both are described below in detail.

803 2.3.1.1 Current-sensitive amplifier

804 Figure 1.8a shows the equivalent circuit of a capacitive source and a current amplifi-
805 er. An amplifier operates in current mode if the source has a low charge collection
806 time t_c with respect to the $R_i C_d$ time constant of the circuit. In this case the sensor
807 capacitance discharges rapidly and the output current i_o is proportional to the in-

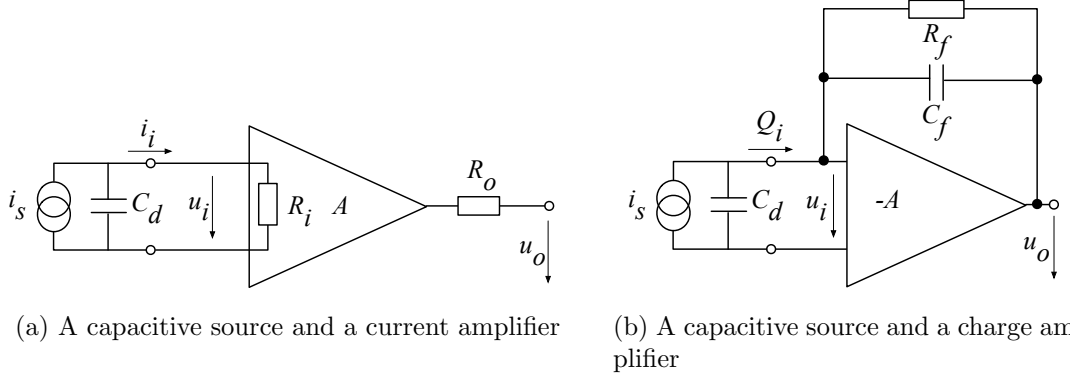


Figure 2.8: Simplified equivalent circuits of a current and charge amplifier

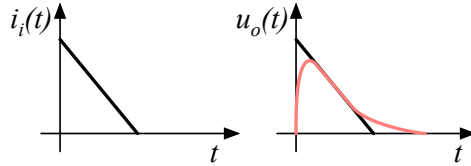


Figure 2.9: Input and output signal of the current amplifier

stantaneous current i_i . The amplifier is providing a voltage gain, so the output signal voltage u_o is directly proportional to the input voltage u_i :

$$u_o(t) = A \cdot R_i \cdot i_s(t). \quad (2.14)$$

The detector capacitance C_{det} together with the input resistance of the amplifier R_i defines the time constant of the signal (see figure 1.9). The higher the C_{det} is, the slower will be the response of the amplifier. For the case of the diamond sensor, which has the capacitance of the order of 2 pF and the input resistance of 50 Ω , the resulting time constant is $\tau = 10^{-10}$ s. This yields the signal rise time $t_r \sim 2.2\tau = 0.22$ ns.

2.3.1.2 Charge-sensitive amplifier

In order to measure integrated charge in the sensor, a feedback loop is added to the amplifier (see figure 1.8b). The feedback can be used to control the gain and input resistance, as well as to integrate the input signal. The charge amplifier is in principle an inverting voltage amplifier with a high input resistance.

In an ideal amplifier the output voltage u_o equals $-Au_i$. Therefore the voltage difference across the capacitor C_f is $u_f = (A + 1)u_i$ and the charge deposited on the capacitor is $Q_f = C_f u_f = C_f(A + 1)u_i$. Since no current can flow into the amplifier, all of the signal current must charge up the feedback capacitance, so $Q_f = Q_i$.

In reality, however, charge-sensitive amplifiers respond much slower than is the duration of the current pulse from the sensor. In addition, a resistor is added to the

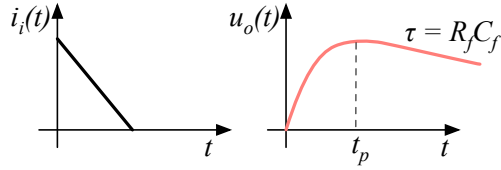


Figure 2.10: Input and output signal of the charge amplifier

826 feedback line in parallel to the capacitor. The resistor and capacitor define the decay
 827 time constant of the pulse (see figure 1.10). This is necessary to return the signal to
 828 its initial state and ready for a new measurement.

829 2.3.1.3 Analogue electronic noise

830 Electronic noise determines the ability of a system to distinguish signal levels. The
 831 analogue signal contains a lot of information, which can quickly be erased or altered
 832 if the signal properties change. It is therefore instrumental to understand the noise
 833 contributions to the signal to qualify the information it carries. There are several
 834 noise contributions, of which the important ones are listed below. The thermal noise
 835 is the dominant noise contribution in the use case for diamond detector signal ampli-
 836 fication and therefore defines the limitations of the detector system. Thermal noise
 837 or Johnson–Nyquist [] noise is generated by the random thermal motion of charge
 838 carriers in the conductor. The frequency range of the thermal noise is from 0 to
 839 ∞ with a more or less uniform distribution. Therefore this is nearly a white noise.
 840 The resulting signal amplitude has a Gaussian distribution. The RMS of the noise
 841 amplitude is defined as

$$u_{\text{RMS}} = \sqrt{4k_B RT \Delta f} \quad (2.15)$$

842 where k_B is the Boltzmann constant, R is the resistance of the conductor, T its
 843 temperature and Δf the frequency range. This equation shows that it is possible to
 844 reduce the noise RMS by either (1) reducing the frequency range, (2) reducing the
 845 resistance of the conductor or (3) cooling the conductor.

846 Contributions of shot noise, flicker noise and burst noise and other types are not
 847 significant relative to the thermal noise. However, the contributions of external factors
 848 can severely deteriorate the signal. This means the noise produced by capacitive or
 849 inductive coupling with an external source, which causes interference in the signal.
 850 These effects can be reduced by shielding the electronics and avoiding ground loops.

851 2.3.2 Analogue-to-digital converters

852 An analogue-to-digital converter (ADC) is a device that converts the analogue elec-
 853 trical signal on the input to its digital representation - a series of digital values. This
 854 involves a quantisation – *sampling* of the signal at a defined sampling period, resulting

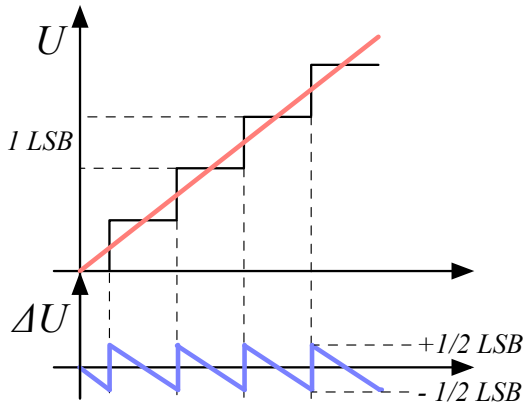


Figure 2.11: Input signal digitisation and quantisation error

in a sequence of samples at a discrete time period and with discrete amplitude values. The resolution of the ADC is the number of output levels the ADC can quantise to and is expressed in bits. For instance, an ADC with a resolution $n = 8$ bit will have the dynamic range $N = 2^n = 256$ steps. The resulting voltage resolution Q_{ADC} at the input voltage range of $V_{\text{ADC}} = \pm 50$ mV is then equal to

$$Q_{\text{ADC}} = \frac{V_{\text{ADC}}}{2^n} = \frac{100 \text{ mV}}{2^8 \text{ steps}} = 0.39 \text{ mV/step}. \quad (2.16)$$

With a sampling period of $t_s = 1$ ns this will produce the sampling rate of $f_s = 1$ GSFS (gigasample per second).

Quantisation error and quantisation noise (or a round-off error) is a contribution to the overall measurement error due to digitisation (rounding). It is defined as a difference between the actual analog value and a digitised representation of this value. The error is defined by the least significant bit (LSB), as seen in figure 1.11. Typically, the input signal amplitude is much larger than than the voltage resolution. Therefore the quantisation error is not directly correlated with the signal and has an approximately uniform distribution []:

$$\Delta Q_{\text{ADC}} = \frac{1}{\sqrt{12}} \text{ LSB} \sim 0.289 \text{ LSB}. \quad (2.17)$$

For the example above the quantisation error will be $\Delta Q_{\text{ADC}} = 0.289 \cdot 0.39 \text{ mV} = 0.11 \text{ mV}$. The error depends strongly on the linearity of the ADC, but this will not be discussed in this document as the devices used have ADCs with a linear response.

2.3.3 Digital signal processing

The digitised signal can be processed to extract useful information. Therefore after the signal amplification and digitisation the signal is routed in a device which handles

875 the analysis. The signal can either be processed immediately (in real time) or it can
876 be saved to a data storage for analysis at a later stage (offline). The devices carrying
877 out the processing can be multipurpose (e.g. Field programmable gate arrays) or
878 dedicated (e.g. application-specific integrated circuits). Each of the two has its
879 advantages and disadvantages, which are listed below.

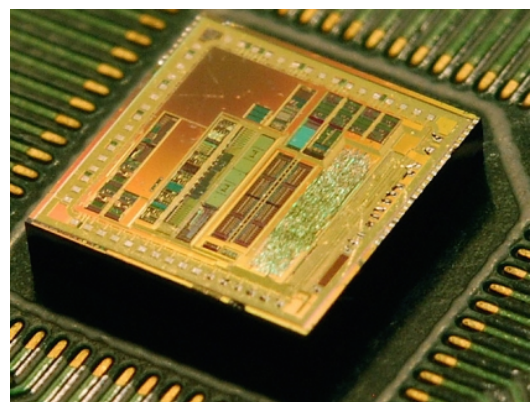
880 **Field programmable gate array** (FPGA) is an integrated circuit designed to be
881 reprogrammable and reconfigured after manufacturing. It consists of a set of logic
882 gates that can be interconnected in numerous combinations to carry out a logic op-
883 eration. Many such logic operations can take place in parallel, making the FPGA a
884 powerful tool for signal processing. FPGAs are often used during system develop-
885 ment or in systems in which the requirements might change with time. They can
886 be reprogrammed in the order of seconds. In addition, the logic design only needs
887 minor changes when migrating to a newer version of the FPGA chip of the same
888 vendor. They also offer faster time-to-market with comparison to application-specific
889 solutions, which have to be developed. On the other hand, the price per part can be
890 significantly higher than for the application-specific solutions. Also, their other major
891 disadvantages are a high power consumption and a relatively low speed. However,
892 today's solutions are capable of clock speeds of the order of 500 MHz. Together with
893 the integrated digital signal processing blocks, embedded processors and other mod-
894 ules, they are already very powerful and versatile. All in all, FPGAs are a good choice
895 for prototyping and limited production, for projects with a limited requirements for
896 speed and complexity.

897 **Application-specific integrated circuit** (ASIC) is an integrated circuit designed
898 for a specific use. The design cannot be modified after chip production, as compared
899 to FPGAs. On the other hand, the ASICs can be optimised to perform a required
900 operation at a high speed and at a low power consumption. In addition, due to the
901 specific design the size of the chip can be much smaller. ASICs can be designed
902 as hybrid chips, containing both a digital and an analog part. To update the chip,
903 the design has to be submitted to a foundry, which produces the new chips with a
904 turnover time of 4–6 weeks. The costs of a submission start at \$ 50 000, but the
905 price per part can be reduced significantly with a high volume. To sum up, ASICs
906 are used for high volume designs with well defined requirements where some stringent
907 constraints in terms of power consumption and speed have to be met.

2.3. ELECTRONICS FOR SIGNAL PROCESSING



(a) Xilinx Virtex 5 FPGA [13]



(b) ASIC [1]

Figure 2.12: An example of an FPGA and an ASIC chip

⁹⁰⁸ Chapter 3

⁹⁰⁹ Experimental results

⁹¹⁰ *Diamond irradiation study*

⁹¹¹ This chapter contains the measurement results of data taken with diamond sensors.
⁹¹² First the measurement setup is described (section 1.1). Then the measured particle
⁹¹³ spectra are shown in 1.2. This is followed by a study of effects of irradiation damage
⁹¹⁴ on the electrical signal of the diamond detector and its lifetime. The last section
⁹¹⁵ shows the results of the measurements of irradiated diamond samples at cryogenic
⁹¹⁶ temperatures. The aim of these studies is to find the operational limitations of dia-
⁹¹⁷ mond detectors for spectroscopy and tracking applications. The studies compare the
⁹¹⁸ experimentally acquired data with the theory from the previous chapter and define
⁹¹⁹ limitations of the diamond detectors in terms of noise, radiation and temperature.

⁹²⁰ Diamond sensors are mainly used for two types of measurements: particle counting
⁹²¹ and spectroscopy. The first type of measurements depends on the sensor's efficiency –
⁹²² the ability to detect all or at least a known percentage of radiation quanta (particles
⁹²³ or photons) that hit it. The energy of the radiation is not so important; what bears
⁹²⁴ the information is the rate and the spatial distribution. Here the radiation does
⁹²⁵ not necessarily stop in the bulk, but rather continues its way. In spectroscopy, on
⁹²⁶ the other hand, the idea is that a particle stops within the sensor, depositing all
⁹²⁷ its energy, which is then measured via the freed charge carriers. The aim of the
⁹²⁸ experiments described in this chapter is to:

- ⁹²⁹ 1. Quantify the efficiency of the sCVD diamond in counting mode,
- ⁹³⁰ 2. Quantify the degradation of efficiency with respect to the received radiation
⁹³¹ dose,
- ⁹³² 3. Quantify the macroscopic effects on charge carrier behaviour with respect to
⁹³³ the received radiation dose and
- ⁹³⁴ 4. Define limitations for its use in spectroscopy.

⁹³⁵ The results discussed here show that there are several limitations for using diamond as
⁹³⁶ a measurement device. All of them need to be taken into account for the measurement

3.1. MEASUREMENT SETUP

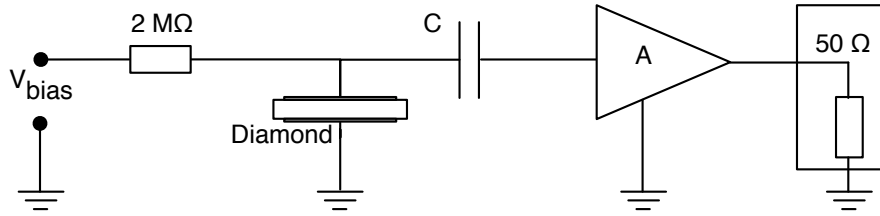


Figure 3.1: Diagram of a diamond detector readout chain.

device to perform reliably and stably. The first step is to build a setup that is insensitive to external electromagnetic interferences and minimises electrical noise in the system. The setup needs to be calibrated before use. Then, the measurement conditions have to be defined, such as the temperature, the type of radiation and its flux. This allows us to estimate the lifetime of the detector and predict the longterm change of the signal. This change can then be accounted for when interpreting the output data.

3.1 Measurement setup

To get reliable measurement results, great care has to go towards designing a measurement setup that minimises the noise in the measurements. Shielding has to be applied wherever possible. For instance, aluminium foil can be wrapped around the exposed parts of the system to shield them from external radio-frequency (RF) interferences. In addition, the sensors have to be covered to prevent the light from shining directly onto them. The incident photons can deposit enough energy to increase the leakage current of the detector.

The measurements using diamond that are explained in these chapters were carried out using several measurement setups, but they are all similar in terms of the electrical signal chain. The measurement chain consists of three main parts: a diamond sensor, a signal preamplifier and a readout device, as seen in diagram 1.1. The signals propagating along the analogue chain (before being digitised by the readout device) are fast – in the GHz bandwidth range – and with low amplitudes – of the order of tens of μV . This gives rise to importance of RF shielding. Also, the connection between the carrier and the preamplifier has to be as short as possible to avoid capacitive signal losses in the transmission line. Finally, the system needs to be grounded properly.

3.1.1 Preamplifiers

Two preamplifiers are used for the measurements, one sensitive to charge and the other to current. *CIVIDEC Cx* (figure 1.2a) is a charge sensing amplifier. Its high SNR (equivalent noise charge of $300 + 30\text{ pF}^{-1}\text{ e}^-$ and a reported gain of $\sim 12\text{ mV/fC}$) makes it a good choice for spectroscopic measurements with diamond

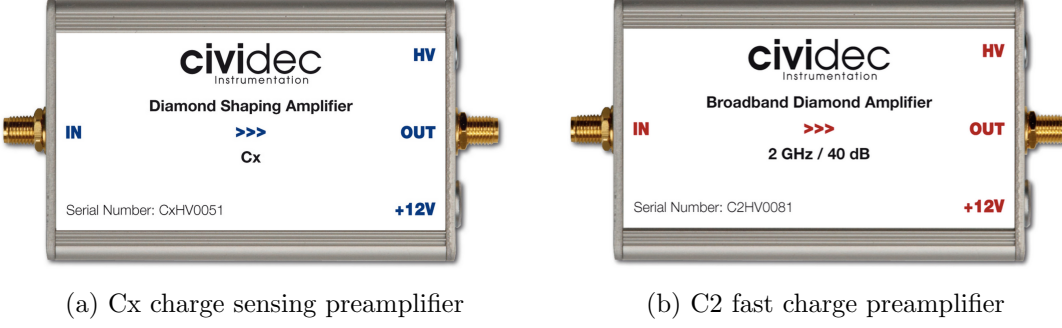


Figure 3.2: Amplifiers used for the charge and current measurements

966 sensors. *CIVIDEC C2* (figure 1.2b) is a fast current preamplifier with a 2 GHz band-
967 width limit. It is used for TCT measurements because of its fast response and a good
968 SNR. Both are embedded in an RF-tight aluminium box to reduce the noise pickup.
969 Both have an AC coupled input and an output with a 50Ω termination.

970 3.1.1.1 Calibration

971 The amplifiers have to be calibrated before use to determine their gain. Both are
972 calibrated using a square signal generator with a known amplitude step of $U_{\text{in}} =$
973 (252 ± 5) mV. A 2 GHz oscilloscope with a 10 GS/s sampling is used to carry out
974 these measurements.

975 In the case of the Cx charge sensitive amplifier, the signal is routed through a
976 capacitor with a calibration capacitance $C_{\text{cal}} = (0.717 \pm 0.014)$ pF and then to the
977 input of the amplifier. The pulse area behind the capacitor is $a_{\text{cal}} = (5.0 \pm 0.5)$ pVs,
978 with the signal amplitude on the output amounting to $U_{\text{Cx}} = (1.95 \pm 0.05)$ V. The
979 input voltage step combined with the calibration capacitance yields a calibration
980 charge $Q_{\text{cal}} = C_{\text{cal}} \cdot U_{\text{in}} = (181 \pm 5)$ fC. The gain of the Cx amplifier is therefore
981 $A_{\text{Cx}}^{\text{Q}} = \frac{U_{\text{Cx}}}{Q_{\text{cal}}} = (9.3 \pm 0.4)$ mV/fC or $A_{\text{Cx}}^{\text{a}} = \frac{U_{\text{Cx}}}{a_{\text{cal}}} = (390 \pm 40)$ mV/pVs. The area-based
982 amplification factor has a higher uncertainty ($\sim 10 \%$) than the amplitude-based
983 factor ($\sim 4 \%$) due to the measurement limitations of the oscilloscope. Nevertheless,
984 it can be used as an estimate for the integrated charge of a current pulse.

985 To calibrate the C2 current amplifier, only the amplitude gain has to be measured.
986 The input signal amplitude has to be such that it keeps the output amplitude within
987 the amplifier's linear range, that is ± 1 V. The signal from the generator is therefore
988 routed through a 36 dB attenuator to decrease its amplitude to $U_{\text{inAtt}} = (3.95 \pm$
989 $0.05)$ mV. Two amplifiers with different gains have been measured, because both
990 are used for the measurements at different times. The output of the first amplifier
991 amounts to $U_{\text{C2-1}} = (860 \pm 5)$ mV. This yields the amplification gain equal to $A_{\text{C2-1}} =$
992 $\frac{U_{\text{inAtt}}}{U_{\text{C2-1}}} = (217 \pm 3)$. The second amplifier has the output equal to $U_{\text{C2-2}} = (632 \pm 5)$ mV
993 with the gain equal to $A_{\text{C2-2}} = (152 \pm 3)$.

3.1. MEASUREMENT SETUP

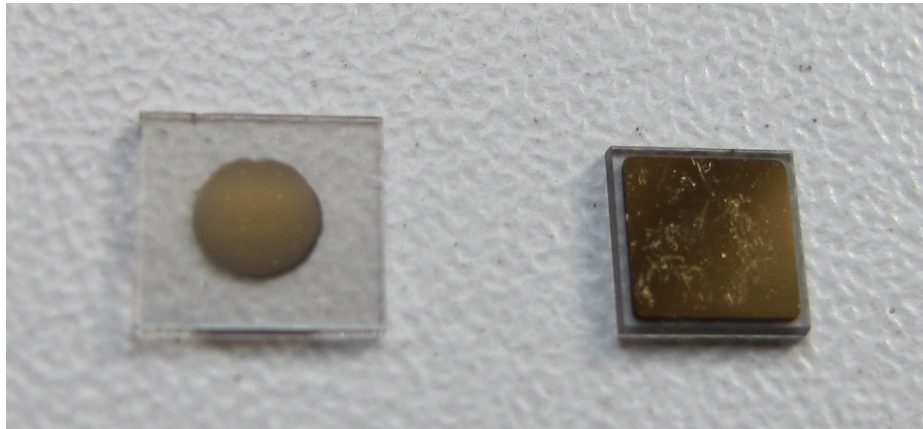


Figure 3.3: Two scCVD diamond samples: A IIa 1scdhq (left) and an E6 S37 (right)

3.1.2 Diamond samples

Detector-grade diamonds are very difficult to produce, mostly because it is very difficult to ensure a high enough purity of the lattice. The sensor samples used for these studies were bought at Element Six (E6) [5]. They all have the same standard dimensions. sCVD diamonds with dimensions $4.7 \times 4.7 \text{ mm}^2$ are already sufficiently large for most of the beam monitoring applications and still affordable. One of the samples with dimensions of $5.6 \times 5.3 \text{ mm}^2$ produced by IIa Singapore [7] was also sent to CERN to be characterised. The target thickness for all the samples is $500 \mu\text{m}$. Diamonds this thick yield a high enough signal-to-noise ratio for MIPs to be measured by the electronics. Table 1.1 shows all the samples used for this study. Two of them were later irradiated with 300 MeV pions and then compared to the pre-irradiated state. Irradiation doses for damaging the material need to be high – above 10^{12} particles per cm^2 to be able to observe change in the sensor's behaviour.

	Name	Type	Producer	Dimensions [mm^2]	Thickness [μm]	Electrode	Irradiated
	S37	sCVD	E6	4.7×4.7	548	Cr/Au	no
	S50	sCVD	E6	4.7×4.7	537	Cr/Au	no
	S52	sCVD	E6	4.7×4.7	515	Cr/Au	$1 \times 10^{14} \pi \text{ cm}^{-2}$
	S79	sCVD	E6	4.7×4.7	529	Cr/Au	$3.63 \times 10^{14} \pi \text{ cm}^{-2}$
	ELSC	sCVD	E6	4.7×4.7	491	Cr/Au	no
	1scdhq	sCVD	IIa	5.6×5.3	460	Cr/Au	no

Table 3.1: Diamond sensor samples used

The diamond samples have quoted impurity densities of $\leq 2 \times 10^{14} \text{ cm}^{-3}$ and nitrogen incorporation of $\leq 1 \text{ ppb}$. The electrodes were added by various companies and institutes. For instance, S52 was metallised by a company DDL (now defunct) while the Physics Department of the University of Firenze, Italy metallised the S79. There are also several techniques for producing the electrodes. The DDL contacts consist of three layers: DLC (diamond-like carbon)/Pt/Au with 4/10/200 nm thicknesses, respectively. The metallisation for S79, on the other hand is made up of Cr/Au with

a total thickness of ~ 400 nm. The area coverage also differs from sample to sample. Diamonds must not be metallised until the very edge as the proximity of contacts with a high potential can lead to sparking. However, the areas not covered by the metallisation are less efficient because the fringe fields at the edges are not as strong as in the middle. This effectively reduces the sensitive area of the sensors. In the diamonds used here the effective area was anywhere from 9 mm^2 to 18 mm^2 . Leakage current through the bulk was below 1 ns, but increased for the irradiated samples. The capacitance was of the order of (2.0 ± 0.3) pF.

3.1.3 Readout devices

Electrical signals in diamond detectors are in the GHz frequency range. To preserve this information, the readout device has to have a high bandwidth limit. For instance, a 250 MHz limit is enough for the spectroscopic measurements with the Cx charge amplifier, but might be insufficient for the current measurements with the C2 amplifier. Two devices are used take data shown in this chapter. The first choice is a 2 GHz LeCroy WaveRunner 204MXi-A. This specific model has a high enough limit for the fast current preamplifier signals. It offers a versatile solution for analogue signal readout – it is fast to set up and reliable. It is very convenient for use in lab tests and for experiments where small amounts of data are taken and where speed is not crucial. However, its slow acquisition speed turns out to be a bottleneck in the test beam experiment. Its initial 100 Hz readout rate decreases to a mere 20 Hz within 20 minutes, because every single trigger is saved as a separate file and the Windows operating system is not capable of handling 10000+ files in a single directory easily. This is why it has been exchanged with a DRS4 [4], an analogue readout device developed by PSI, Switzerland. This compact device is capable of recording up to four waveforms at a time at a steady rate of up to 500 Hz. Its 700 MHz bandwidth limitation is sufficient for the signal from the charge amplifier.

3.1.4 Setup for the efficiency study using β particles

The efficiency study of the diamond sensors has been carried out at CERN in the North Hall test beam facility. There a straight high-energy particle beam of $\pi_{120}\text{ GeV}$ is provided to the users to calibrate their detectors. The beam had a transverse spread of $\sigma = 10$ mm in both axes. The particle rate is of the order of $10^4 \pi \text{ cm}^{-2} \text{ s}^{-1}$. A diamond sensor embedded in a PCB carrier has been placed in the beam spot perpendicular to the beam and connected via an SMA connector directly to a charge amplifier (described below). The amplified signal is read out using a LeCroy oscilloscope and a DRS4 analogue readout system (both described below). A computer is used as a controller and data storage for the readout device. A beam telescope is used as a reference detector. It is a device that helps to cross-check the measurements of the devices under test (DUTs) and to carry out spatially resolved studies on the DUTs. It consists of several pixellated sensor planes placed in series, which can track a particle's trajectory with a precision of a few μm . The sensor planes are positioned

3.1. MEASUREMENT SETUP

in front of the DUT and behind it. Then the beam telescope acts as a trigger system – it triggers the readout of both the telescope data and DUT data when both the planes in front and behind the DUT recorded a hit by the incident particle. A particle detected by all the planes within the DUT window and the DUT itself counts towards its efficiency whereas a hit missed by the DUT means that the DUT is not 100 % efficient. To discard the hits that miss the DUT completely, a region of interest (ROI) can be chosen in the beam telescope planes. The equation for calculating the sensor efficiency is therefore

$$\epsilon = \frac{N_{\text{DUT}} \wedge N_{\text{telescope}}}{N_{\text{telescope}}} \quad (3.1)$$

for an ROI smaller than the sensitive region of the diamond.

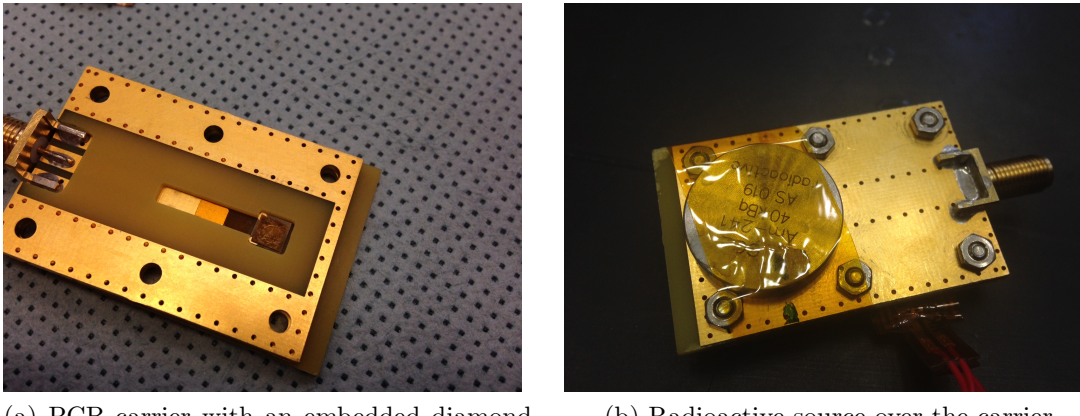
3.1.5 Room temperature α -TCT setup

This TCT study is a follow-up of an extensive diamond TCT study at cryogenic temperatures [28]. The room-temperature TCT measurements have been carried out in the lab. The setup consists of a diamond sensor embedded in a PCB carrier, a current amplifier and an oscilloscope. To measure α particles, their energy loss during their trajectory has to be minimised. Therefore the diamond is placed inside a vacuum chamber. The chamber is a steel tube with a diameter of 5 cm. On one side it is connected to a vacuum pump via a steel pipe. A feedthrough with an SMA connector is placed on the other side. A C2 current amplifier is connected directly onto the feedthrough. The amplified output is connected to the oscilloscope via an SMA cable. An ^{241}Am source with a diameter of 2 cm and a height of 0.5 cm is fixed onto the sensor carrier (figure 1.4a, figure 1.4b). Then the carrier is inserted in the chamber and fixed in place using an air-tight clamp. The pump can then be switched on. It is capable of providing the inside pressure as low as 10^{-4} mbar after approximately one hour of operation, but measurements can take place even after five minutes of evacuation, at around 10^{-3} mbar. The most important thing to bear in mind is to switch the bias voltage of the sensor OFF during the process of evacuation, because the gas becomes more conductive at the pressure of the order of 10^{-1} mbar, which is at the bottom of Paschen's curve [21]. A failure to switch off the bias voltage may cause a spark between the signal and ground line, destroying the amplifier.

3.1.6 Cryogenic α -TCT setup

The experiment at cryogenic temperatures has been carried out in the cryolab at CERN. The room-temperature TCT setup has to be modified to allow for measurements at temperatures as low as 2 K. It consists of three parts:

1. a cryostat – a thermally insulated cylinder capable of containing liquid helium,
2. an inlet – an air-tight mechanical tube with valves and feedthroughs at the top that is lowered in the liquid helium and



(a) PCB carrier with an embedded diamond sample
(b) Radioactive source over the carrier sample

Figure 3.4: Positioning of the α -source on top of the sensor carrier

1093 3. the diamond sample embedded in a PCB carrier with a fitted temperature
1094 sensor, a heater and cables leading to the feedthroughs.

1095 The setup is described in detail in [28].

1096 When the diamond sample is placed in the PCB carrier and the ^{241}Am source is in
1097 place, the inlet is sealed and lowered in the empty cryostat. Then the inside volume
1098 of the inlet is evacuated to down to 10^{-5} mbar while the liquid helium is flowing into
1099 the cryostat. To improve the thermal contact between the diamond and the coolant,
1100 a small amount of helium gas is added inside the evacuated inlet, setting the vacuum
1101 to around 10^{-3} mbar. This value changes with time, because the gas condenses on
1102 the walls of the inlet, reducing the number of floating particles. For this reason the
1103 helium gas has to be added on an irregular basis. Every addition causes a significant
1104 undershoot of the sample temperature, which had to be corrected for using a heater
1105 placed on the back of the PCB carrier. Also, the added gas deteriorates the vacuum
1106 inside the inlet. It is very important to monitor the pressure so as not to let it rise
1107 above 10^{-2} mbar. The gas at this pressure is significantly more conductive and could
1108 cause a short circuit between the two diamond plates or in the SMA connectors,
1109 destroying the amplifier. Furthermore, at approximately 60 K the helium gas has to
1110 be evacuated from the inlet to avoid a potential explosion due to the expansion of
1111 the gas with temperature.

1112 When the sample is cooled to the minimum temperature achievable by means
1113 of liquid helium without over-pressurising it (4.2 K), the measurements start. A
1114 temperature sensor placed on the back of the PCB carrier is used to measure the
1115 temperature of the sample. After every temperature data point, the current through
1116 the heater placed in the PCB next to the diamond sample is increased, warming up
1117 the sample. The initial temperature time constant of the order of tenths of seconds at
1118 low temperatures increases with temperature. Even more so when helium is evacuated
1119 from the inlet at 60 K, removing the thermal bridge between the wall of the inlet and
1120 the diamond sample. At the room temperature (RT), the time constant increases to

3.2. CHARGED PARTICLE PULSES AND SPECTRA

1121 the order of minutes.

3.2 Charged particle pulses and spectra

1123 In previous chapter the ionisation profiles for different types of radiation were dis-
1124 cussed. It is known that β and γ radiation induces a triangular electric pulse whereas
1125 α radiation induces a rectangular one. However, their amplitude, width and rise/fall
1126 time depend heavily on the type of interaction with the diamond, the purity of the
1127 diamond and the bandwidth of the amplifier and the oscilloscope. This section shows
1128 the signal pulses of α , β and γ radiation with their respective energy distributions for
1129 the case of a diamond detector. Then follows a discussion of effects of noise on these
1130 measurements.

1131 A CIVIDEC C2 current amplifier together with the LeCroy oscilloscope (both
1132 with a bandwidth limit of 2 GHz) has been used to record the pulse shapes whereas
1133 the Cx charge amplifier is used for charge measurement. A 2 GHz bandwidth limit
1134 defines the minimum rising time equal to $t_r \simeq \frac{0.34}{BW} = \frac{0.34}{2 \times 10^9} = 170$ ps, therefore
1135 the system is capable of measuring pulses with a minimum FWHM $\simeq 170$ ps. This
1136 already makes it impossible to measure the initial peak in the α response due to the
1137 two flavours of charge carriers travelling. If a charge carrier travelling through the
1138 bulk takes $t_{t1} \sim 6$ ns to get to the electrode on the other side ($d_1 \sim 500$ μm), the
1139 carrier with the opposite charge and a shorter path to the closer electrode – max.
1140 $d_2 \sim 10$ μm – only takes $t_{t2} \sim \frac{d_2}{d_1} t_{t1} = 120$ ps. A drift time this short induces a
1141 current pulse that is too narrow for the C2 amplifier or the oscilloscope to be able to
1142 observe.

1143 Figure 1.5 shows a set of pulses and an averaged pulse for α , β and γ radiation
1144 using an ^{241}Am , ^{90}Sr and ^{60}Co source, respectively. The particles are measured with
1145 the non-irradiated sCVD diamond S37. α particles always produce the same signal
1146 pulse, but with a high noise RMS. The averaging suppresses the noise while still
1147 retaining most the information. It does, however, smear the rising and falling edge,
1148 increasing the rise time. The t_r is now of the order of 0.5 ns. Both β and γ pulses
1149 look similar – triangular and with a wide range of amplitudes. Here the pulse count
1150 is low, so the pulses with a high amplitude are not recorded. A trigger set very high
1151 would be needed to “catch” them with the oscilloscope.

3.2.1 Noise limitations

1152 Noise is a major limiting factor in particle detection. It defines the minimum measurable
1153 particle energy and the minimum measurement resolution. It is hence important
1154 to minimise the electric noise in the detector signal. The major noise contribution
1155 comes from poor shielding from external electromagnetic sources. These often cause
1156 ringing, whereby the signal oscillates with a frequency defined by the external source.
1157 The ringing makes high-frequency measurements impossible. Another source of noise
1158 is the sensor itself. In the case of silicon, natural light increases the number of ther-

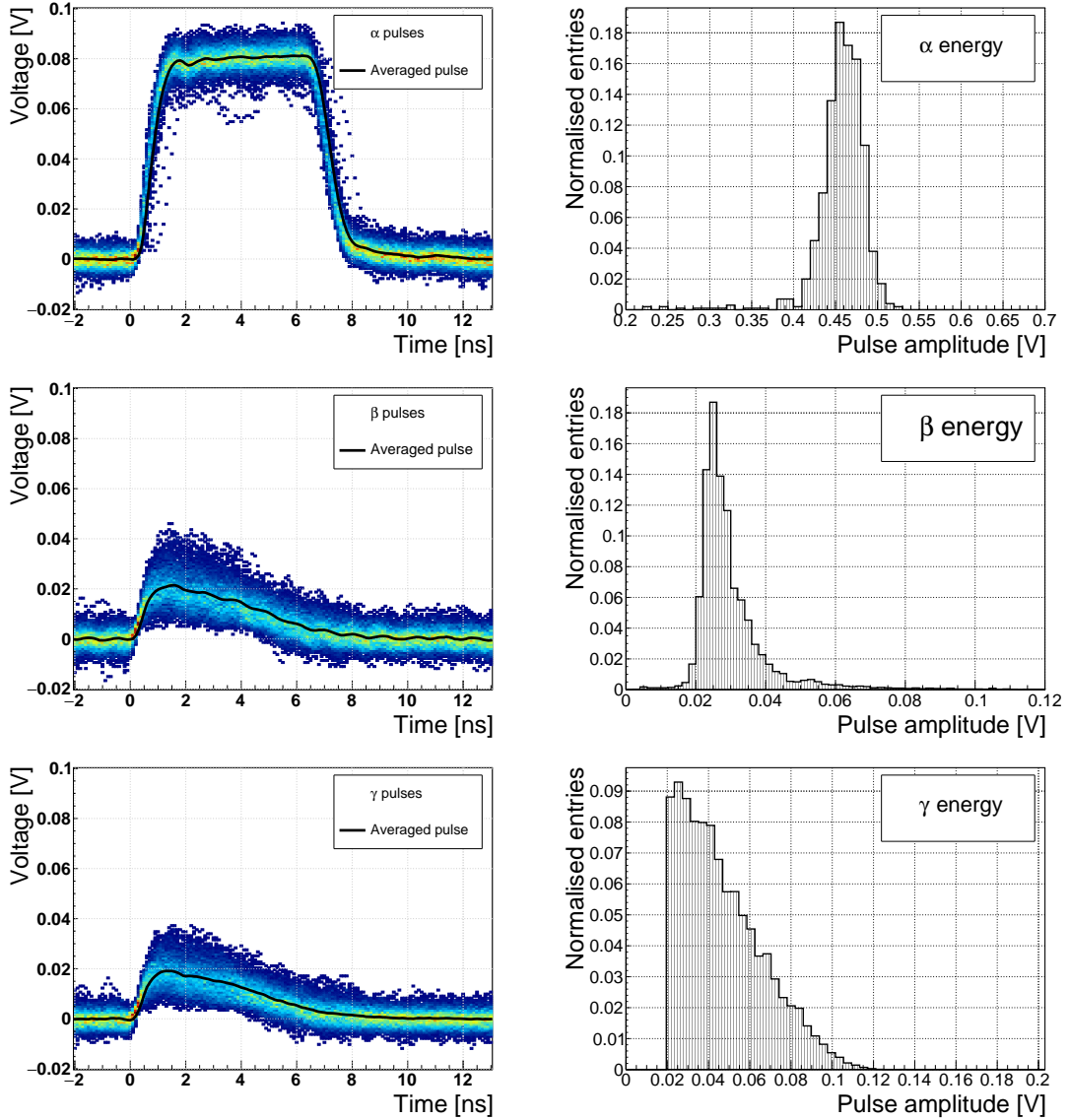


Figure 3.5: Superimposed and averaged pulses (a, b and c, current amplifier) and distributions of deposited energy (d, e, f, charge amplifier) for three types of radiation. Note the scale on the X axis of the distributions.

1160 mally excited free charge carriers, increasing the leakage current. This is not the
 1161 case for diamond, which is with its high energy band gap insensitive to visible light.
 1162 Nevertheless, any noise produced by the sensors is amplified by the signal amplifiers,
 1163 which add an additional noise of the analogue electrical circuit to the amplified
 1164 signal. Finally, the digitisers add the quantisation noise to the digitised signal. If
 1165 the measurement range is significantly higher than the actual measured signal, the
 1166 quantisation noise can be a significant contributor to the decrease of the overall mea-
 1167 surement resolution.

3.3. RADIATION LIMITATIONS

3.3 Radiation limitations

Exposure to ionising radiation degrades sensors. It deforms the lattice by displacing the atoms. Various types of lattice defects can be created in diamond, similar to those in silicon: vacancies, interstitials etc. [31] These deformations introduce new discrete energy levels between the valence and conduction band. Charge carriers drifting in their vicinity can get trapped, their energy falling to the energy level of the trap. Their emission back to the conduction band depends on how deep the trap is (how far away from the conduction band it is). The carriers caught in the shallow traps of the order of 100 meV below the conduction band are excited back up already by means of the thermal excitation. This phenomenon has a short time constant, dependant on the environmental temperature. Those stopped by deep traps near the middle of the band gap need more energy and thus more time to be emitted to either the conduction or valence band. Some charge carriers remain trapped for long periods. If they build up in a certain region of the diamond, their charge starts affecting the surrounding electric field – space-charge forms. It can either help or counteract the field, depending on the polarity of the carrier.

The energy band jumping goes the other way, too. The carriers in the valence band may use the intermediate energy levels as “stepping stones” to jump to the conduction band and start drifting in the externally applied electric field. This is called the leakage current.

The electrons and holes stopped in these traps cause a decrease of the induced current on the electrodes. This yields a lower integrated charge in an irradiated sensor than that in a non-irradiated one. Charge collection efficiency is therefore correlated with the level of irradiation.

This section contains a study of the effects of pion ($\pi_{300 \text{ MeV}}$) irradiation on the charge collection efficiency of sCVD diamond detectors. To carry out this study, two diamond samples have been irradiated to doses of $1 \times 10^{14} \pi \text{ cm}^{-2}$ (S79) and to $3.63 \times 10^{14} \pi \text{ cm}^{-2}$ (S52). Then a test beam campaign has to be carried out to observe the charge collection efficiency at different bias voltage settings. The efficiency values acquired are used to determine the effective drop in efficiency with respect to received radiation dose. This is to test if the collected charge Q is inversely proportional to the received dose Φ . A procedure defined by a collaboration researching diamond behaviour RD42 has been applied to the measured values to extract the damage factor. The next subsection contains measurements and results of a long-term stability study using α and β particles. In particular, the charge collection efficiency as a function of time is measured during the measurements with β and α radiation. To investigate this effect on the scale of charge carriers, the change of TCT pulses with time is observed. Finally, a procedure that improves the pulse shape and with it the charge collection is proposed.

3.3.1 Quantifying radiation damage in diamonds

Radiation damage varies with the type of radiation (particles or photons) and its energy. There are several models existing [27, 26] that try to explain the impact of irradiation and to provide *hardness factors* to compare the radiation damage between different particles. The standard way is to convert the damage into *neutron equivalent* [14]. Some models have been extensively verified with simulations and with experiments. In these experiments charge collection in sensors is measured before and after irradiation. This procedure is repeated several times, with a measurement point taken after every irradiation. When a set of measurements of charge collection is plotted against the radiation dose received by a specific particle at a specific energy, a damage factor k_λ can be extracted. Damage factors have to be measured across a range of energies and types of radiation to properly quantify the damage in the sensors. They are then compared against the simulations to verify that the experimental observations are in line with the theory.

Diamond is an expensive material and the technology is relatively new as compared to silicon. Therefore not many institutes are carrying out diamond irradiation studies. To join the efforts, the RD42 collaboration [11] was formed. It gathers the experimental data from diamond irradiation studies. Unlike with silicon, the experimental results so far show no significant correlation with the NIEL (non-ionising energy loss) model [27], which correlates detector efficiency with the number of lattice displacements. Therefore an alternative model was proposed [26], correlating the diamond efficiency with the number of displacements per atom (DPA) in the bulk. The idea is that if the recoil energy of an incident particle is higher than the lattice binding energy (42 eV for diamond), the atom is displaced from its original position. The newly formed vacancy acts as a trap for drifting charge carriers. The more displacements that form in the bulk, the higher is the probability that a drifting carrier will get trapped, effectively reducing the induced signal. However, different types of particles interact differently with the bulk. In addition the mechanisms of interaction at low energies are different to those at high energies. To assess the damage for individual particles at a range of energies, simulations need to be run first. The simulation shown in [26] shows the DPA model for a range of energies of proton, pion and neutron irradiation in diamond. Figure 1.6 contains the simulation results as well as the superimposed empirical results of several irradiation studies. According to the figure, a 300 MeV pion beam damages the diamond bulk twice as much as a 24 GeV proton beam. The data points obtained by RD42 are also added to the figure. They have been normalised to damage by 24 GeV protons. Finally, the data point measured in the scope of this thesis has been added for comparison. The derivation is done below.

3.3.1.1 Irradiation with a $\pi_{300 \text{ MeV}}$ beam

The samples were irradiated at the Paul Scherrer Institute (PSI) [10] by means of a beam of pions with an energy of 300 MeV (kinetic energy 191.31 MeV) and with a

3.3. RADIATION LIMITATIONS

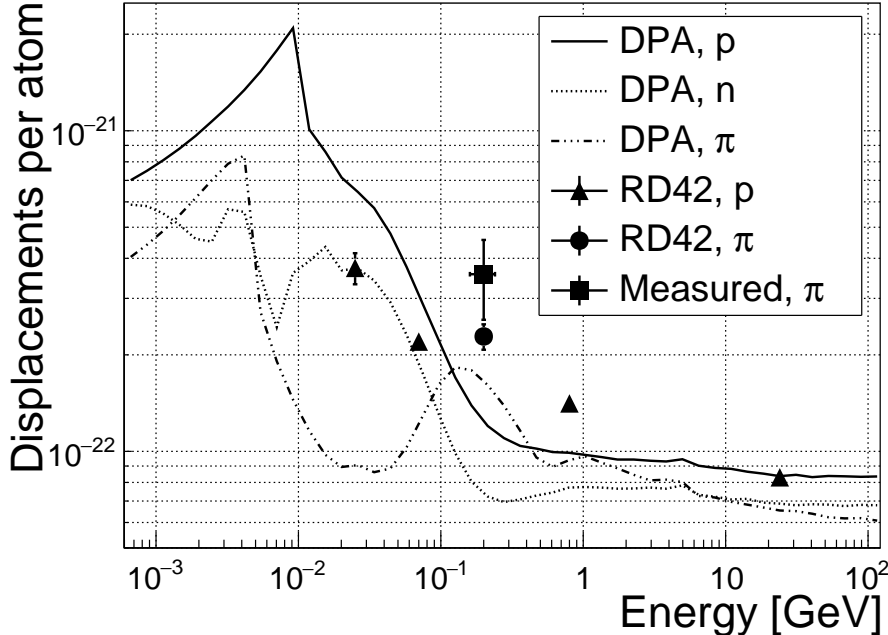


Figure 3.6: Diamond radiation damage - a model based on displacements per atom [26]. Added are data points for protons and pions by RD42 [35] and one data point for pions measured in the scope of this thesis.

1248 flux of up to $1.5 \times 10^{14} \pi \text{ cm}^{-2}$ per day. The system has a 10 % uncertainty on the
 1249 beam energy. In addition, their quoted uncertainty on the measurement has an error
 1250 of $\pm 20\%$. Looking at the pion damage curve in figure 1.6, $\pi_{300 \text{ MeV}}$ point sits on a
 1251 steep section of the DPA curve. This means that a deviation in beam energy can
 1252 have a significant effect on the damage.

1253 Two diamond samples, S52 and S79, were put in the $\pi_{300 \text{ MeV}}$ beam in the 2014
 1254 PSI irradiation campaign; S52 to $(1 \pm 0.21) \times 10^{14} \pi \text{ cm}^{-2}$ and S79 to $(3.63 \pm 0.77) \times$
 1255 $10^{14} \pi \text{ cm}^{-2}$. During the process, the golden electrodes got slightly activated, but the
 1256 activation decayed in two weeks.

1257 3.3.1.2 Charge collection efficiency and charge collection distance

1258 Three diamonds – non-irradiated S37 and irradiated S52 and S79 – were tested in a
 1259 $\pi_{120 \text{ GeV}}$ test beam in the SPS North Experimental Area at CERN [18] before and
 1260 after irradiation. The goal was to estimate the charge collection efficiency (CCE) and
 1261 charge collection distance (CCD) as a function of irradiation dose. The samples were
 1262 primed (pumped) prior to data taking using a ^{90}Sr radioactive source. The data were
 1263 then taken at a range of bias voltages ranging from 30 V to 900 V, yielding between
 1264 0.06 V/ μm and 1.8 V/ μm electrical field in the bulk. Every data point contained
 1265 approximately 5×10^4 measured particles. The charge deposited by the particles
 1266 was measured using a CIVIDEC Cx charge preamplifier. As expected, the integrated

¹²⁶⁷ amplitude spectrum followed a landau distribution. Its most probable value (MPV)
¹²⁶⁸ was used to calculate the most probable collected charge Q_i :

$$Q_i [e^-] = \frac{Q_i [fC]}{1.6 \times 10^{-4}} = \frac{MPV [mV]}{A [mV/fC]} \cdot 6.241 \times 10^4 \quad (3.2)$$

¹²⁶⁹ where $A = 9.2 \text{ mV/fC}$ is the preamplifier gain factor. The CCD was then calculated
¹²⁷⁰ using the average number of electron-hole pairs produced per micrometer in diamond
¹²⁷¹ $\delta_d = 36 \text{ e-h } \mu\text{m}^{-1}$ (from table 1.2):

$$CCD = \frac{Q_i}{\delta d} \quad (3.3)$$

¹²⁷² The resulting CCD for the three measured samples at bias voltages ranging from
¹²⁷³ $0.2\text{--}1.6 \text{ V } \mu\text{m}^{-1}$ is shown in figure 1.7a. S37 exhibits a full collection distance already
¹²⁷⁴ at $0.4 \text{ V } \mu\text{m}^{-1}$ whereas the irradiated samples have a more gentle increase of CCD
¹²⁷⁵ with increasing bias voltage. It is evident that at $1 \text{ V } \mu\text{m}^{-1}$ the maximum CCD has
¹²⁷⁶ not been reached in the case of S79 and S52. Nevertheless, to compare the measured
¹²⁷⁷ data point with those provided by RD42, the CCD at $1 \mu\text{m}$ has to be taken.

¹²⁷⁸ 3.3.1.3 Irradiation damage factor

¹²⁷⁹ The irradiation damage factor k is a way to quantify irradiation damage of a specific
¹²⁸⁰ particle at a specific energy. Via this factor different types of irradiation can be
¹²⁸¹ compared. It is obtained experimentally by measuring the CCD of a number of
¹²⁸² samples at various irradiation steps and fitting the equation 1.5 to the data. λ is the
¹²⁸³ measured CCD, λ_0 is the CCD of a non-irradiated sample and Φ the radiation dose.
¹²⁸⁴ As a reference, the damage factor for 24 GeV protons is set to $1 \times 10^{-18} \mu\text{m}^{-1} \text{ cm}^{-2}$.

$$\frac{1}{\lambda} = \frac{1}{\lambda_0} + k_\lambda \cdot \Phi \quad (3.4)$$

$$\lambda = \frac{\lambda_0}{k_\lambda \lambda_0 \Phi + 1} \quad (3.5)$$

¹²⁸⁵ The data points with the maximum CCD obtained in the test beam measurements
¹²⁸⁶ are plotted against radiation dose received (see figure 1.7b). Equation 1.5 is fitted
¹²⁸⁷ to the data points and a damage factor $k_\lambda = (4.4 \pm 1.2) \times 10^{-18} \mu\text{m}^{-1} \text{ cm}^{-2}$ was
¹²⁸⁸ obtained. This value is for a factor of two higher than the damage factor obtained by
¹²⁸⁹ RD42. This could be due to an insufficient priming time ahead of the measurement.
¹²⁹⁰ In addition, the diamond samples have not been polished and re-metallised after
¹²⁹¹ irradiation, as is the case for the RD42. Also, with only two samples measured, the
¹²⁹² statistical uncertainty is high. Nevertheless, it can be concluded that the 300 MeV
¹²⁹³ pions damage the diamond bulk more than the 24 GeV protons.

3.3. RADIATION LIMITATIONS

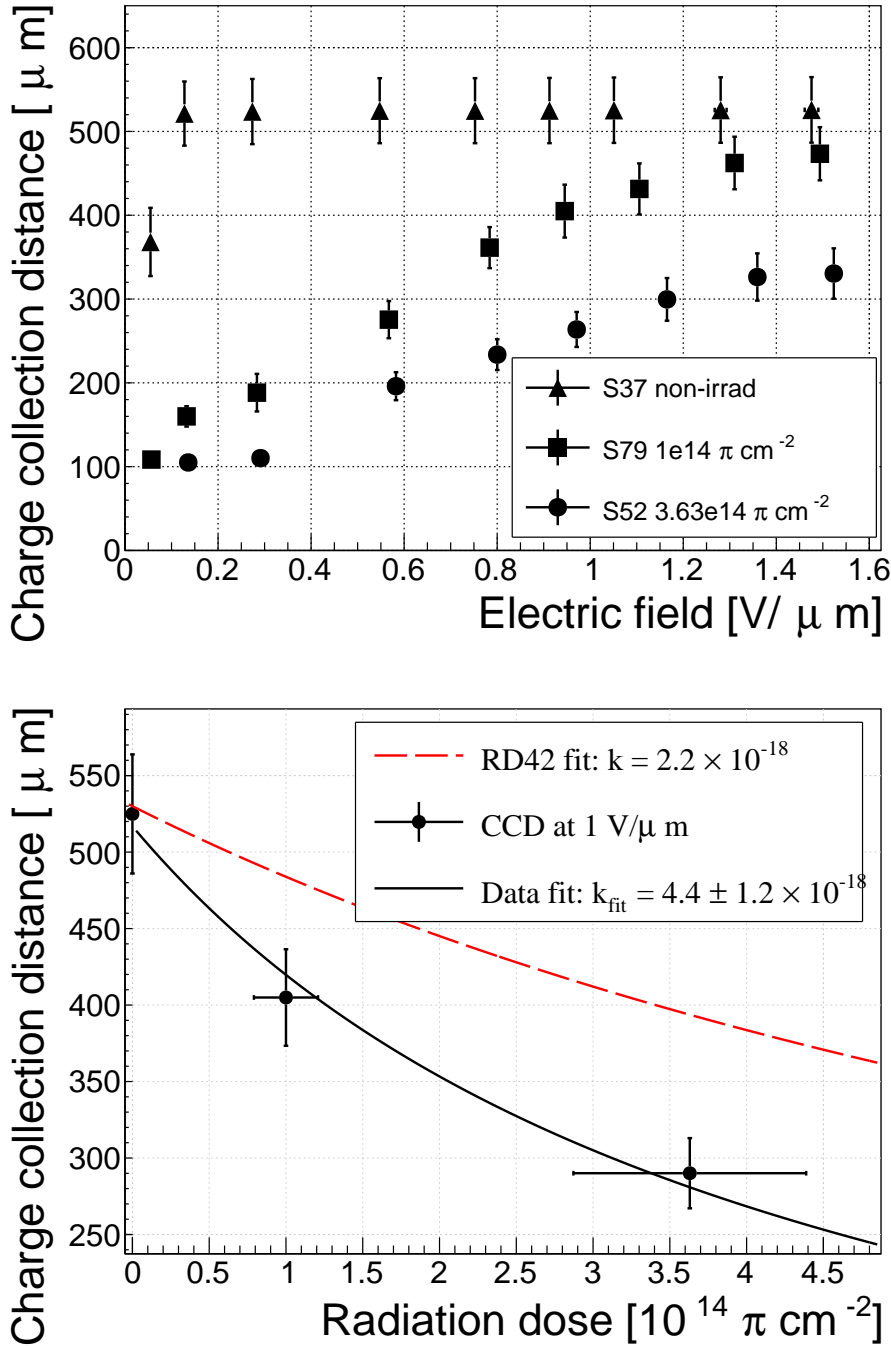


Figure 3.7: First figure shows the CCD for S37, S79 and S52 at a range of bias voltage settings. The charge collection distance at $1 \text{ V}/\mu\text{m}$ bias voltage for the three diamond samples is then compared to the RD42 data for pion irradiation in the second figure. The data points are about 15–25 % lower than expected from the RD42 data [35].

¹²⁹⁵ 3.3.2 Long-term measurement stability

¹²⁹⁶ An important requirement for particle detectors is a stable performance over long
¹²⁹⁷ periods of time. For instance, the charge collection for a defined radiation type and

1298 quantity must not change over time or has to change in a predicted way. Diamonds
1299 are stable as long as their environment and their operating point does not change
1300 significantly. The stability of diamond detectors depends on many factors (material
1301 purity, polishing process, electrode material, irradiation damage etc.). The aim is
1302 to study the behaviour of diamond under controlled conditions, with the goal to
1303 understand its limitations. One of these limitations is for sure the received radiation
1304 dose as it can affect the long-term stability of the sensor during operation.

1305 The three diamond samples (S37, S79 and S52) have been exposed to two different
1306 types of ionising radiation for a longer period to see if their behaviour changes over
1307 time. Two parameters have been observed in particular:

- 1308 1. Charge collection of β particles and
- 1309 2. Charge collection and ionisation profile of α particles.

1310 The results in this and in the next section will show that, in both cases, priming plays
1311 an important role in improving the diamond measurement stability.

1312 **3.3.2.1 β long-term stability**

1313 The diamond samples have undergone a long-term stability test using β radiation.
1314 This has been done using a ^{90}Sr source emitting ~ 2 MeV electrons at a rate of
1315 approximately $10^4 \text{ e}^- \text{ cm}^{-2}$. To simulate the initial conditions in HEP experiments,
1316 the sensors must not be primed before starting the measurements. The measurement
1317 setup consists of a diamond sample (S37, S52 or S79) with the Cx spectroscopic
1318 amplifier, a silicon diode with a C6 amplifier for a trigger and a ^{90}Sr source on
1319 top. A particle emitted by the source traverses the sensor bulk and hits the silicon
1320 diode, triggering the analogue signal readout. The source is left on the top for the
1321 course of the experiment. The measurements, however, are taken at discrete times.
1322 For every data point, approximately 10^4 triggers are recorded. The offline analysis
1323 of the recorded signal pulse amplitudes yields a landau distribution for every data
1324 point. The most probable value (MPV) of the distribution is proportional to the
1325 collected charge by the diamond sensor. The resulting graph of charge collection over
1326 time (see figure 1.8) shows that the charge collection efficiency improves when the
1327 diamond sensor is primed with a β source. This is especially evident in the case of
1328 the two irradiated samples. S79 achieves close to a full efficiency whereas S52 reaches
1329 about 50 %. Both increases are significant. At a received dose of approximately
1330 4×10^6 particles the signal stabilises. As expected, the signal of the non-irradiated
1331 S37 does not change with time – this pure sCVD diamond sample has the maximum
1332 collection distance from the start of the measurement.

1333 It should be noted that the ~ 2.28 MeV electrons emitted by this source are not
1334 MIPs; their charge deposition is higher than that of an electron MIP, according to the
1335 Bethe-Bloch distribution [16]. Nevertheless, for the purpose of these measurements
1336 this energy was adequate since only the relative change in charge collection was of
1337 our interest.

3.3. RADIATION LIMITATIONS

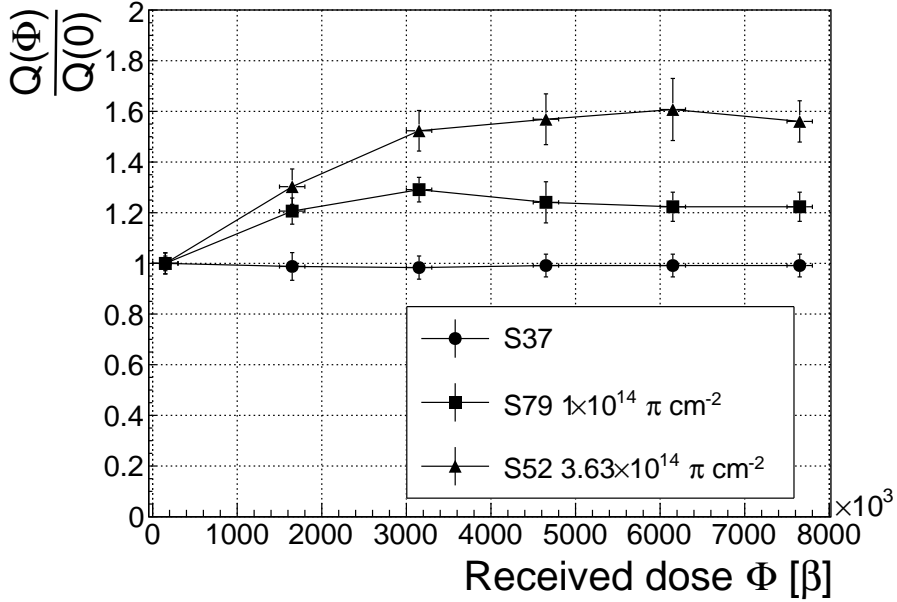


Figure 3.8: Relative increase of charge collection over time due to priming with the ${}^{90}\text{Sr}$ radioactive source. The bias voltage for this measurement is 1 V/ μm .

To sum up, diamond is a good choice for β radiation detection. Even if damaged by radiation, it reaches a stable charge collection at a received dose of $\sim 4 \times 10^6$ MIP particles. The efficiency decreases with a high irradiation dose (effects visible above 10^{12} MIP cm^{-2}). However, the decrease can be accounted for if the damage factor and the rate and energy of the particles are known. γ radiation has a similar impact on the diamond as the β because the ionisation mechanism is the same. The incident photons, if they interact with the diamond, prime the bulk, causing the increase in charge collection efficiency. The difference, however, is that the interaction probability (cross section) is lower for gammas [41, 25].

3.3.2.2 α long-term stability

This part discusses the stability of irradiated diamond sensors during α measurements. An ${}^{241}\text{Am}$ source is used, emitting α particles with a mean energy of 5.5 MeV. It is safe to assume that they will behave differently than when subject to β radiation. This is due to the point-like charge carrier creation when an α particle penetrates the bulk and stops at a depth of $\sim 14 \mu\text{m}$ (for a 5.5 MeV particle). The deposited energy produces $\frac{5.5 \text{ MeV}}{13.6 \text{ eV}} = 4 \times 10^5$ e-h pairs. Compared to a MIP, which produces an MPV of $500 \mu\text{m} \times 36 \text{ e-h } \mu\text{m}^{-1} = 18 \times 10^3$ e-h pairs in a $500 \mu\text{m}$, the collected charge is for a factor of 22 higher. In addition, the energy is deposited in a small volume – $14 \mu\text{m}$ in depth and $\sim 20 \text{ nm}$ radially [28]. This dense distribution of charge carriers affects their behaviour at the start of the drift. Furthermore, carriers of only one polarity drift through the sensor while those of the opposite polarity almost instantly

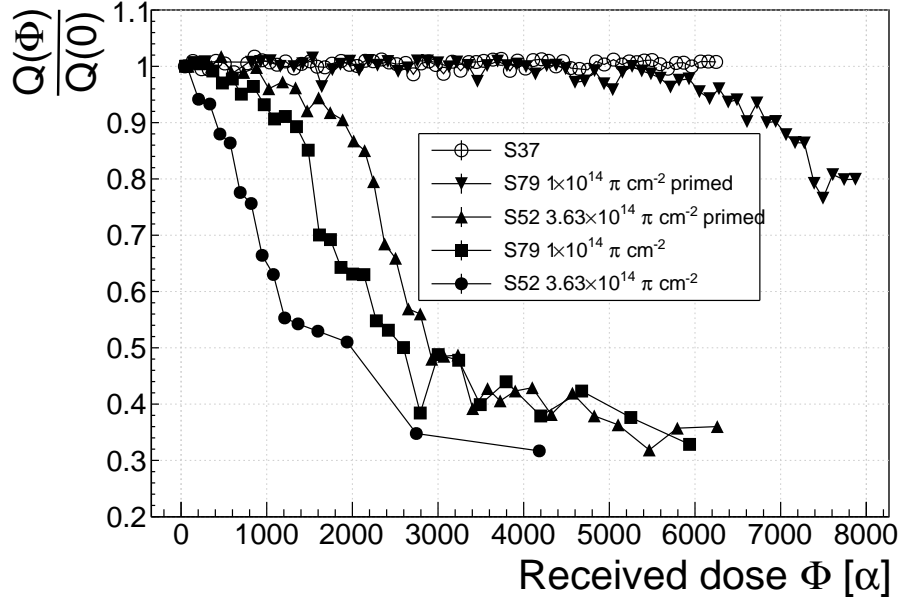


Figure 3.9: Relative decrease of collected charge with time for non-irradiated and irradiated diamond samples.

1359 recombine with the adjacent electrode. Taking into account that the diamond bulk
1360 has been damaged by irradiation, these two phenomena might have an effect on the
1361 operation of the detector on a macro scale.

1362 The first test has been carried out using the Cx spectroscopic amplifier, with
1363 the bias voltage of the samples set to +500 V. Figure 1.9 shows the results of 6500
1364 recorded hits at a rate of ~ 7 particles per second. The collected charge $Q(\Phi)$ for
1365 the non-irradiated sample is stable as compared to the initial collected charge $Q(0)$
1366 (plotted as a relative value $\frac{Q(\Phi)}{Q(0)}$). It is expected that the irradiated samples will have
1367 a lower charge collection efficiency than the non-irradiated sample. However, their
1368 initial efficiency suddenly drops after a certain period of time. The initial efficiency
1369 after priming with β particles is higher than that without priming, but eventually it
1370 deteriorates again. In addition, the spread of measured energies increases significantly.
1371 Finally, the particle counting rate decreases with the decreased efficiency.

1372 To investigate this sudden drop in efficiency, the current pulse shapes using a
1373 C2 current amplifier have to be observed (see figure 1.10). The shape of the pulse
1374 holds more information about the charge carrier properties in the sensor than solely
1375 the value of the integrated charge. This time only the primed S79 sample has been
1376 tested. Both hole and electron collection are observed to determine whether they
1377 behave differently or not. The sample has been measured long enough for the pulse
1378 shapes to start changing. The data in figures 1.10 show that the initially stable pulses
1379 start deteriorating – suddenly several different shapes start appearing, some still very
1380 similar to those from the beginning while the others with almost zero amplitude.

1381 Some charges get stopped in the charge traps in the bulk for a long time, building

3.3. RADIATION LIMITATIONS

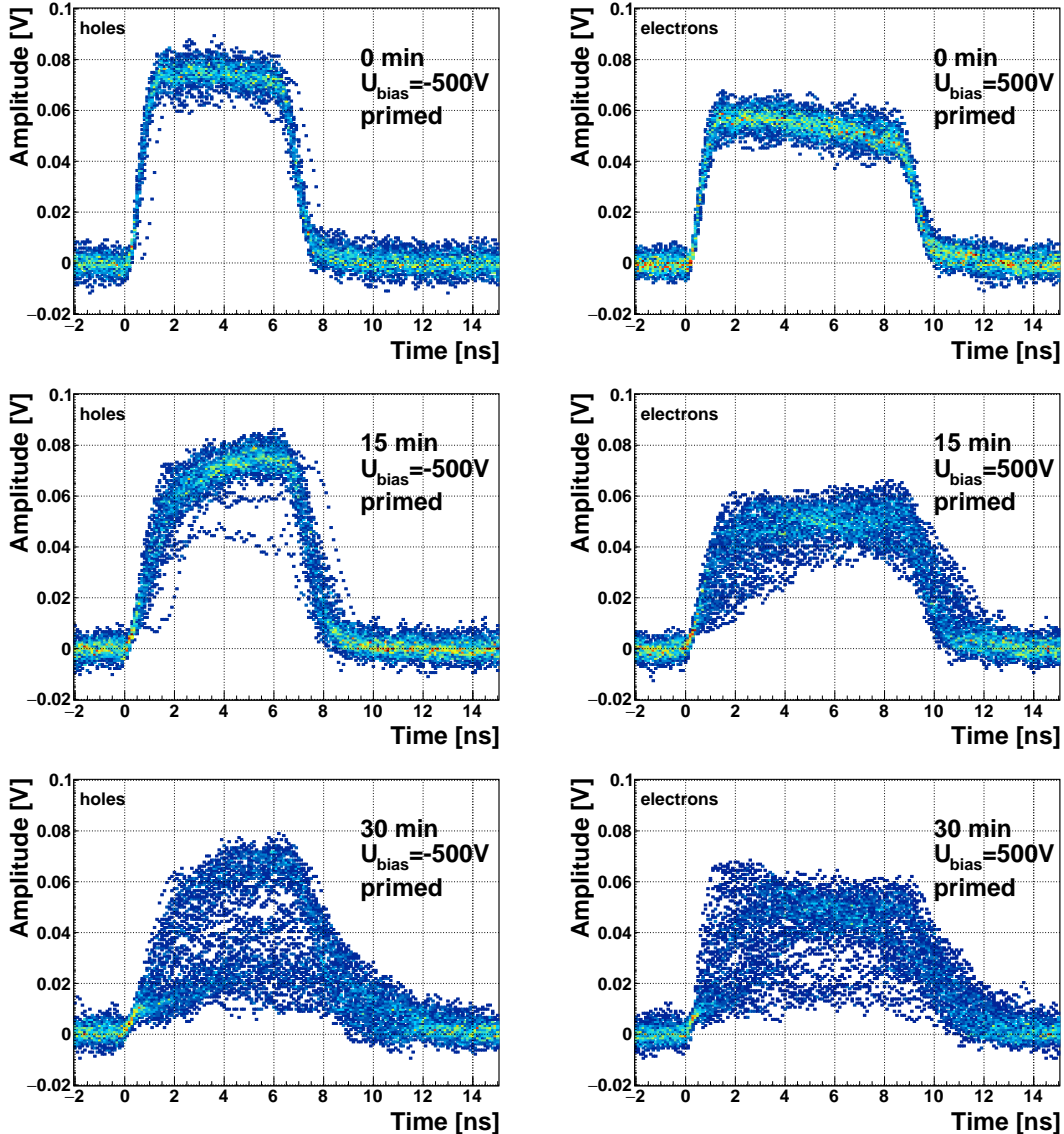


Figure 3.10: The signal of the irradiated and primed S79 deteriorates with time for both polarities. Every plot contains 60 superimposed pulses.

1382 up regions of space charge. The built up space charge affects the electric field, making
 1383 it non-uniform. The non-uniform field in turn affects the drifting carriers, slowing
 1384 them down or speeding them up, depending on the field gradient. Since the movement
 1385 of the carriers is inducing the electric current, the field gradient can be observed in
 1386 the signal.

1387 The second test with the C2 current amplifier has been carried out as follows: At
 1388 the beginning of the test when the diamond is still operating stably, 60 pulses are
 1389 recorded. An average pulse is calculated. This is a reference pulse for the subsequent
 1390 measurement points. Then an RMS of the single pulses with respect to the reference
 1391 pulse is calculated and the values are summed together (σ_{ref}).

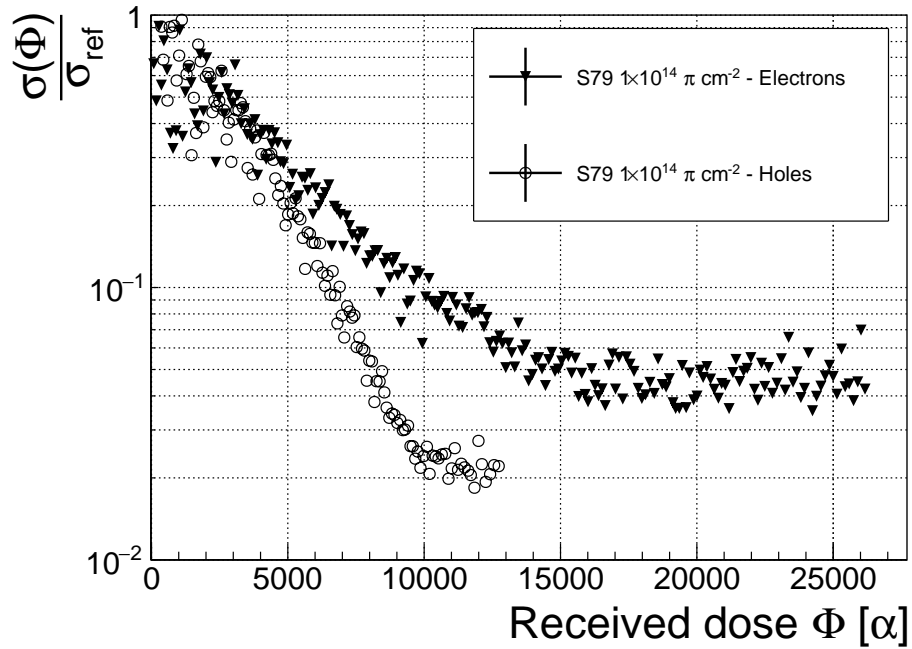


Figure 3.11: Deterioration of the pulse shapes with time

1392 All the subsequent data points also consist of a set of 60 pulses. At every data point
 1393 the summation of the RMS values of the individual pulses with respect to the initial
 1394 averaged pulse is calculated (σ). The ratio between the initial σ_{ref} and discrete values
 1395 σ gives a measure of change of the pulse shape with respect to the reference pulse at
 1396 the start of the measurement. Figure 1.11 shows the ratio $\frac{\sigma_{\text{ref}}}{\sigma(\alpha \text{ dose})}$. From the data
 1397 obtained it can be concluded that initial pulse shape quickly starts deteriorating. In
 1398 fact, the deterioration of the shape follows an approximate exponential decay function,
 1399 which can be fitted to the data. The resulting decay constants for electrons and holes
 1400 are $\tau_e = (4400 \pm 150) \alpha^{-1}$ and $\tau_h = (3300 \pm 140) \alpha^{-1}$. The electrons retain the initial
 1401 shape for longer. The deteriorated shapes also seem to be for a factor of 2 better
 1402 than those of the holes.

1403 Finally, an effort has been made to find a way for the pulse shapes to return to
 1404 their initial state. Five methods are listed:

- 1405 1. Removing the source and leaving the bias voltage switched on,
- 1406 2. Removing the source and switching the bias voltage off,
- 1407 3. Priming with γ at a rate of $400 \text{ s}^{-1} \text{cm}^{-1}$ without applied bias voltage,
- 1408 4. Priming with β at a rate of $1000 \text{ s}^{-1} \text{cm}^{-1}$ with applied bias voltage and
- 1409 5. Priming with β at a rate of $1000 \text{ s}^{-1} \text{cm}^{-1}$ without applied bias voltage.

1410 The diamond sample S79 is first primed using a ^{90}Sr source for about one hour.
 1411 Then the bias voltage is switched on and an ^{241}Am source is put on top. The pulses

3.4. TEMPERATURE LIMITATIONS

produced by the incident α particles have a proper rectangular pulse at the beginning, but then start changing – first gradually and later increasingly more in an erratic way, as described in the text above. After approximately 30 minutes, one of the methods is tested. When a “healing” procedure is started, a set of 60 pulses is taken at irregular points of time to observe the change in the pulse shape and to assess the quality of the “healing” procedure. Then the bias voltage is switched off and the sample is primed again to reset its state before starting with the next run.

The results depicted in figure 1.12 show that the methods (3) and (5) improve the shape, method (2) helps slowly, (1) does not show any change with time and (4) at first improves, but then significantly degrades the shape. The effect observed in method (4) has already been described in [32]. The “healing” process therefore depends on the rate of radiation, the bias voltage and the time of exposure. The ionising radiation creates free charges, which quickly recombine close to the place of generation. It is likely that they also release the charges trapped during the measurement, reducing the overall effect of the space charge. The traps get filled with both flavours of carriers, thus they are neutralised. The pulse shape gradually returns to its initial state.

Procedure	Source	Bias voltage	Effectiveness
1	/	ON	no
2	/	/	slow
3	^{60}Co	/	YES
4	^{90}Sr	ON	no
5	^{90}Sr	/	YES

Table 3.2: Effectiveness of healing procedures

In summary, the shape of the pulses caused by α radiation changes with time for irradiated samples. The shape of the pulses gets distorted and becomes erratic. Charge collection decreases and its spread increases. This happens even faster for non-primed diamonds. To “heal” the diamond – to bring the pulse shapes back to their initial shape – the sample must be primed using a β or a γ source for several minutes at the bias voltage set to 0 V. Switching to the inverse polarity for a few seconds helps a bit, but in a long run distorts the signal, which cannot get back to its initial shape.

3.4 Temperature limitations

A test has been carried out to evaluate the effect of temperature changes on the output signal of the diamond sensors. A cryostat filled with liquid helium is used to cool down the sensor during the measurement process. The current signal response to α -particles is measured at 18 temperature points between 4 K and 295 K. At every temperature point, a set of 300 pulses is read out at various bias voltages. Resulting data show that the charge collection is stable down to 150 K, where it starts decreasing and stabilises again at about one third of the initial value at 75 K. This behaviour was first measured and discussed by H. Jansen [28].

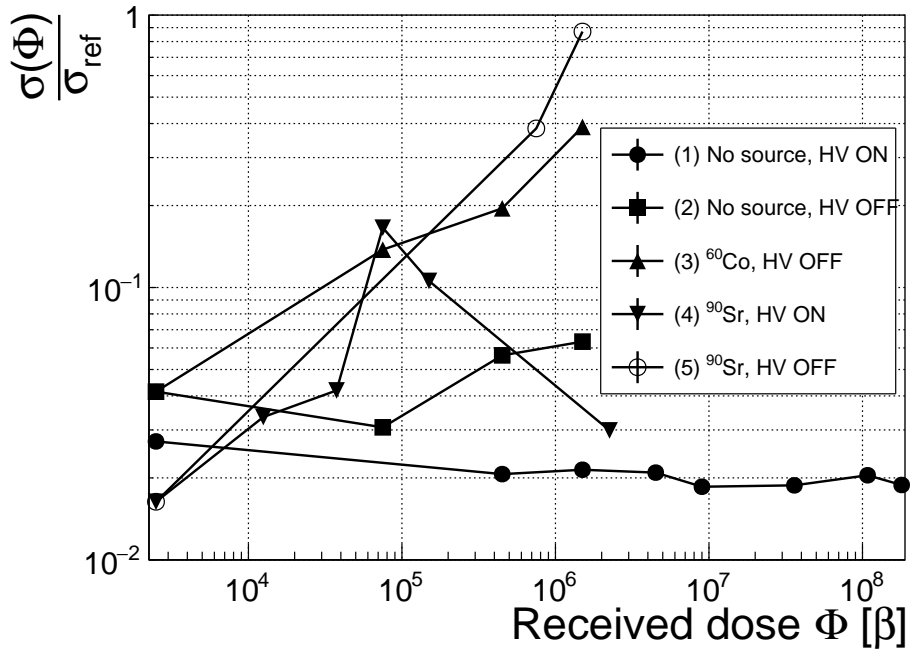


Figure 3.12: Five procedures for the “healing” process for an irradiated diamond that was exposed to α radiation at bias voltage switched on for at least 30 minutes at a rate of 10^4 s^{-1} .

The band gap energy in diamond is equal to $E_g = 5.5 \text{ eV}$ while the average energy to produce an electron-hole pair is $E_{e-h} = 13.25 \text{ eV}$. This means there is excessive energy deposited in the diamond bulk. The incident α -particle stops within $\sim 10\text{--}15 \mu\text{m}$ of the bulk, transferring all its energy to the lattice during deceleration. A part of this energy directly ionises the carbon atoms, creating free electron-hole pairs. The positively charged hole and the negatively charged electron in the hole attract each other via the Coulomb force and may undergo a bonding process during which a phonon is emitted.

The remaining energy, however, is converted into lattice vibrations (phonons [45, 28]). This means that the lattice within the ionisation volume (approximately $\sim 15 \mu\text{m} \times \sim 2 \text{ nm}$ in size) is briefly heated up. The hot plasma then cools down to the temperature of the surrounding material by heat dissipation, (i.e. phonon transport). The free electron binds the free hole into a bound state (not recombination) – the exciton [33]. The exciton binding energy is 80 meV. At higher temperatures, the lattice provides enough energy to excite the electron from the exciton state back to the conduction band. At lower temperatures, however, the exciton lifetime increases, which means that it will take a longer time for the electrons to get re-excited to the conduction band. The re-excitation lifetime at room temperature is $\sim 30 \text{ ps}$, increasing to $\sim 150 \mu\text{s}$ at 50 K [28]. This means that some of the bound electrons will not even start drifting within the period of $\sim 10 \text{ ns}$, which is the expected carrier drift time. When they are finally freed, the current they induce is already hidden in the electronics noise.

3.4. TEMPERATURE LIMITATIONS

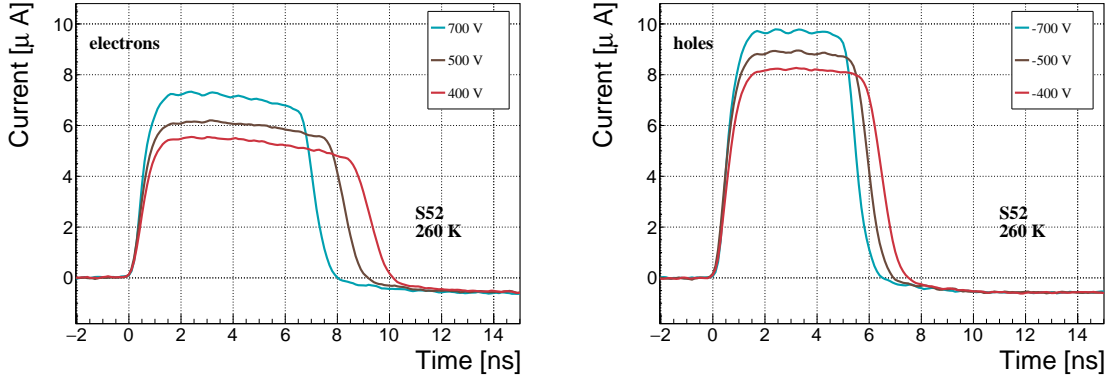


Figure 3.13: Varied bias voltage at a fixed temperature

The effective area of the observed current pulse is therefore smaller than that of a pulse induced by all the carriers drifting at the same time. This in effect reduces the measured collected charge. The longer the time constant, the lower the measured collected charge, as shown in figure 1.17 below.

3.4.1 Temperature-variant α -TCT before irradiation

Three sCVD diamond samples have been tested at a range of temperatures using the α -TCT technique. At each temperature point, the bias voltage is set to several positive and negative values. A set of 300 pulses is recorded at every data point and averaged offline. The resulting averaged pulses of sample S37 at the 260 K temperature point and a bias voltage of ± 400 V, ± 500 V and ± 700 V are shown in figure 1.13. The pulses induced by holes as charge carriers are shorter than those induced by electrons, which means that holes travel faster in diamond. The area of the pulse, however, is the same for both polarities, which corresponds to the fact that the same amount of charges is drifting in both cases.

Figure 1.14 shows pulses at a bias voltage set to ± 500 V across the range of temperatures between 4 K and 295 K – room temperature (RT). Several conclusions can be drawn by observing their shape. First, the pulse shapes change with decreasing temperature. The pulse time gets shorter, hinting at the faster carrier drift velocity v_{drift} . Second, between 150 K and 75 K there is a significant change in shape - the time constant of the rising edge increases significantly and the pulse area decreases. From 75 K down to 4 K there is no significant observable change. Last, the top of the pulse at the S52 is not flat, which means that a portion of the drifting charge is lost along its way. This is due to charge trapping, likely by means of crystal defects or impurities.

*CHAPTER 3. EXPERIMENTAL RESULTS
DIAMOND IRRADIATION STUDY*

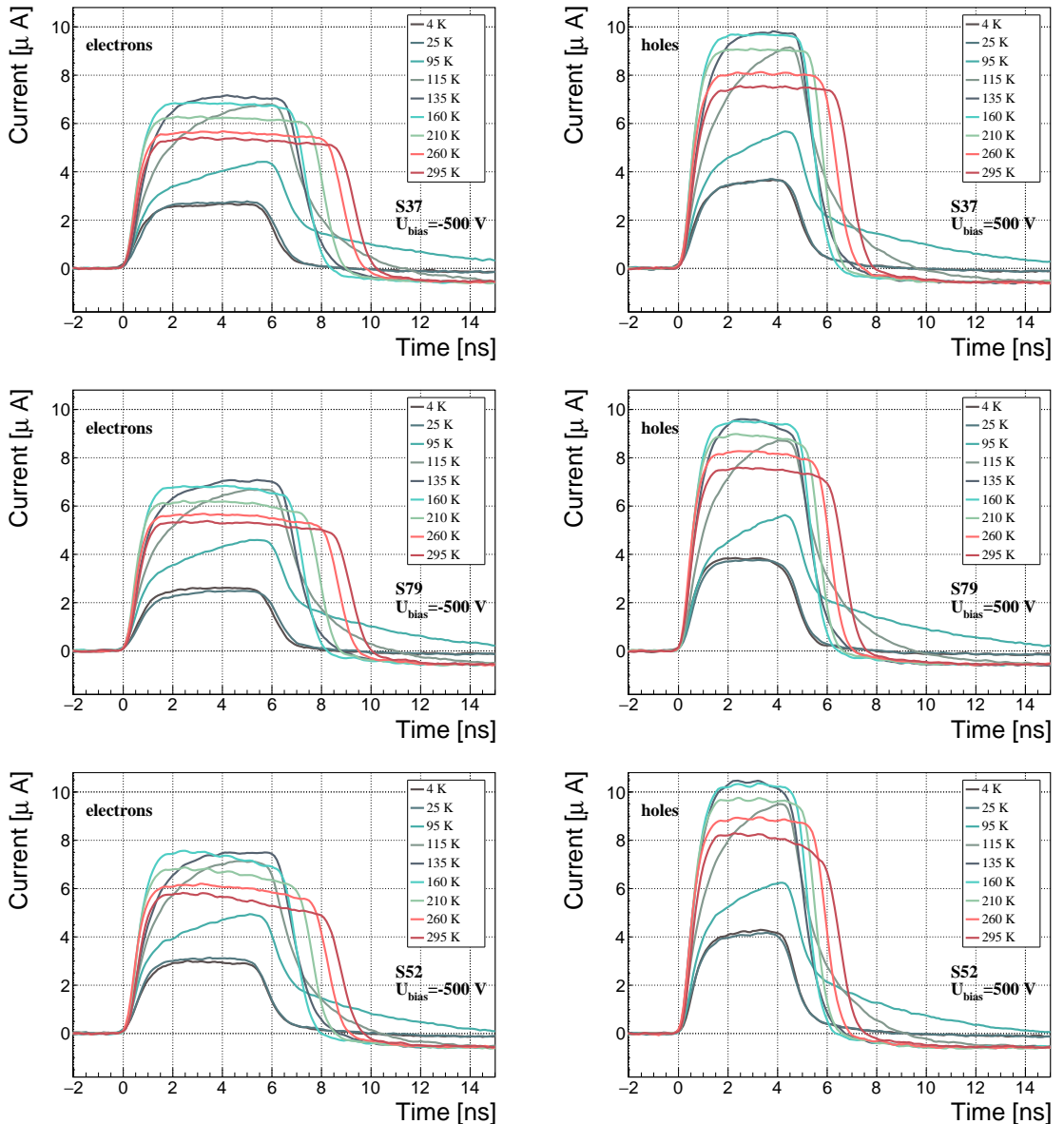


Figure 3.14: Several data points between 4 K and 295 K at a bias voltage of ± 500 V

3.4. TEMPERATURE LIMITATIONS

3.4.2 Temperature-variant α -TCT after irradiation

The irradiated S79 and S52 have been re-tested in the cryostat after irradiation. The aim was to see how their pulse shapes change with decreasing temperature, in particular the decaying top of the pulses (see figure 1.15). The decay time gives information on trapping of charge carriers while travelling through the diamond bulk. A variation of the decay time constant as a function of temperature might help to reveal the type and depth of the charge traps. To observe these effects or lack thereof, a number of requirements has to be met. First, the diamond samples are intentionally not primed prior to the experiment because priming would improve the pulse shapes and possibly change the decay time constant of the signal. Second, keeping in mind that the pulse shape of irradiated diamonds changes with time, the duration of the measurement of an individual data point has to be short – of the order of 30 seconds. Last, the sequence of the bias voltage settings is important, the reason for which is explained below.

Unfortunately it is not possible to avoid temporal pulse changes. For instance, one measurement point takes approximately one minute. After the measurement, the bias voltage polarity is swapped for a few seconds to bring the diamond back into its initial state. But a few seconds with respect to a minute is not enough. Therefore, when the bias voltage is set to the next value, there is still some residual effect of the previous measurement. Similar to the effects of polarisation, this effect is also decreasing the pulse height. This can be observed in figure 1.15, which shows the resulting pulses of S52 for bias voltages of ± 200 V, ± 300 V, ± 400 V and ± 500 V at 230 K and 260 K. In this case the measurements sequence is: 230K (200 V, 300 V, 400 V, 500 V, -500 V, -400 V, -300 V), 260 K (-200 V, -300 V, -400 V, -500 V, 500 V, 400 V, 300 V). The changes in pulse shapes for holes at 230 K and 260 K cannot be attributed to the temperature change. Instead, the explanation could lie in diamond “polarisation”. This means that, when exposed to an electric field with α measurements ongoing, the diamond builds up an internal electric field of inverse polarity, which effectively reduces the overall electric field. This internal field does not dissipate when the external bias voltage is switched off. It can be said that the diamond becomes “polarised”. When switching the polarity of the external bias voltage, the internal and external electric field point in the same direction at the beginning, increasing the overall electric field and with it the pulse height. In figure 1.15, this happens when switching from 500 V (figure 1.15a) to -500 V (figure ??) at 230 K. The built up polarisation contributes to the pulse having a sharp rising edge and a high amplitude. This effect decays during the next two voltage points. There would be a handful of ways to avoid this polarisation effect in the data:

1. After every data point invert the bias voltage and leave it to return to a neutral state for the same amount of time,
2. Make a hysteresis of data points, going from minimum negative to maximum positive bias several times,

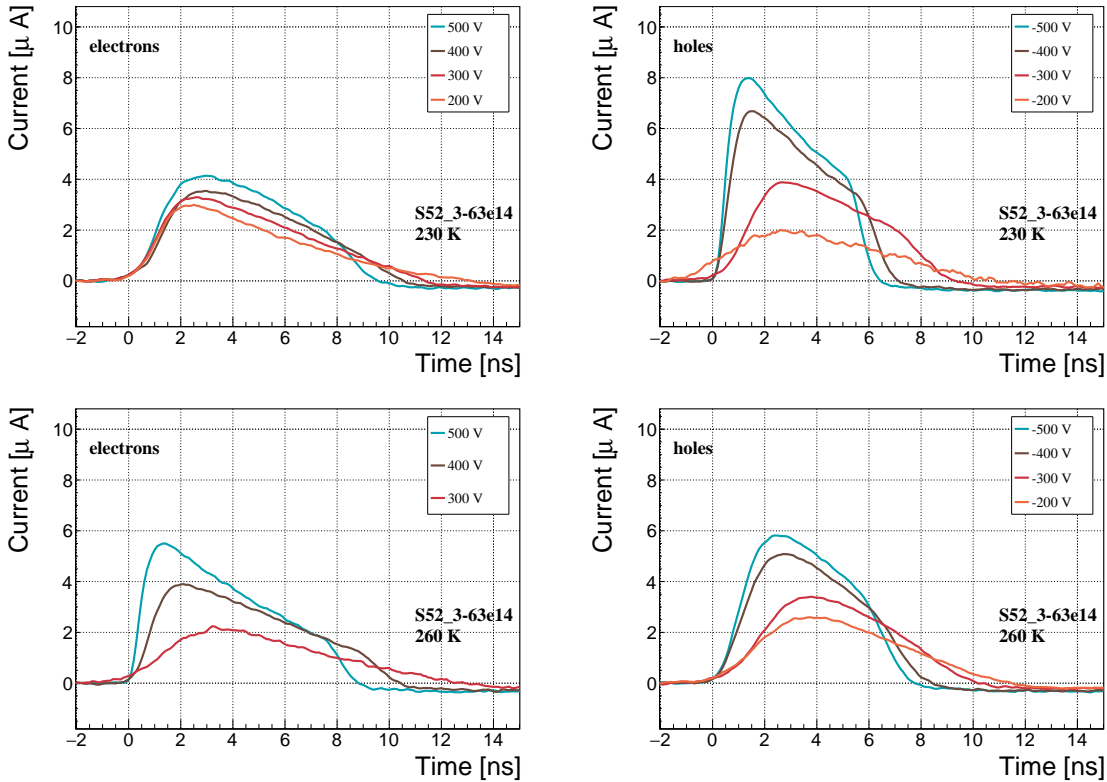


Figure 3.15: Varied bias voltage at a fixed temperature for an irradiated sample

1534 3. Reduce the measurement time at every bias voltage setting.

1535 Unfortunately, options (1) and (2) are very time consuming and would increase the
1536 overall experiment time to over one day. The third option would worsen the resulting
1537 averaged pulses. In the end an alternative option was chosen: alternating the start-
1538 ing bias voltage and the sequence at every temperature point. With this option, a
1539 meaningful systematic error in analysing the pulse shapes can be attained.

1540 Figure 1.16 shows the irradiated S52 and S79 as well as the non-irradiated S37
1541 for comparison, all at a bias voltage of ± 500 V and at several temperature points
1542 between 4 K and RT. It is evident that the radiation damage affected the shape of
1543 the pulses across all temperatures.

1544 3.4.2.1 Collected charge as a function of temperature

1545 The area below the current pulse is proportional to the charge collected by the dia-
1546 mond detector. The collected charge is observed as a function of temperature. First,
1547 the amplitude values of the averaged pulses at a bias voltage of ± 500 V and across the
1548 temperature range between 4 K and 295 K have to be integrated. Then a calibration
1549 factor is used to derive the charge for all data points. This factor is obtained using
1550 a Cx charge-sensitive amplifier. The resulting values for electrons and holes are plot-
1551 ted in figures 1.17a and 1.17b, respectively. Thesis [28] gives a model that explains

3.4. TEMPERATURE LIMITATIONS

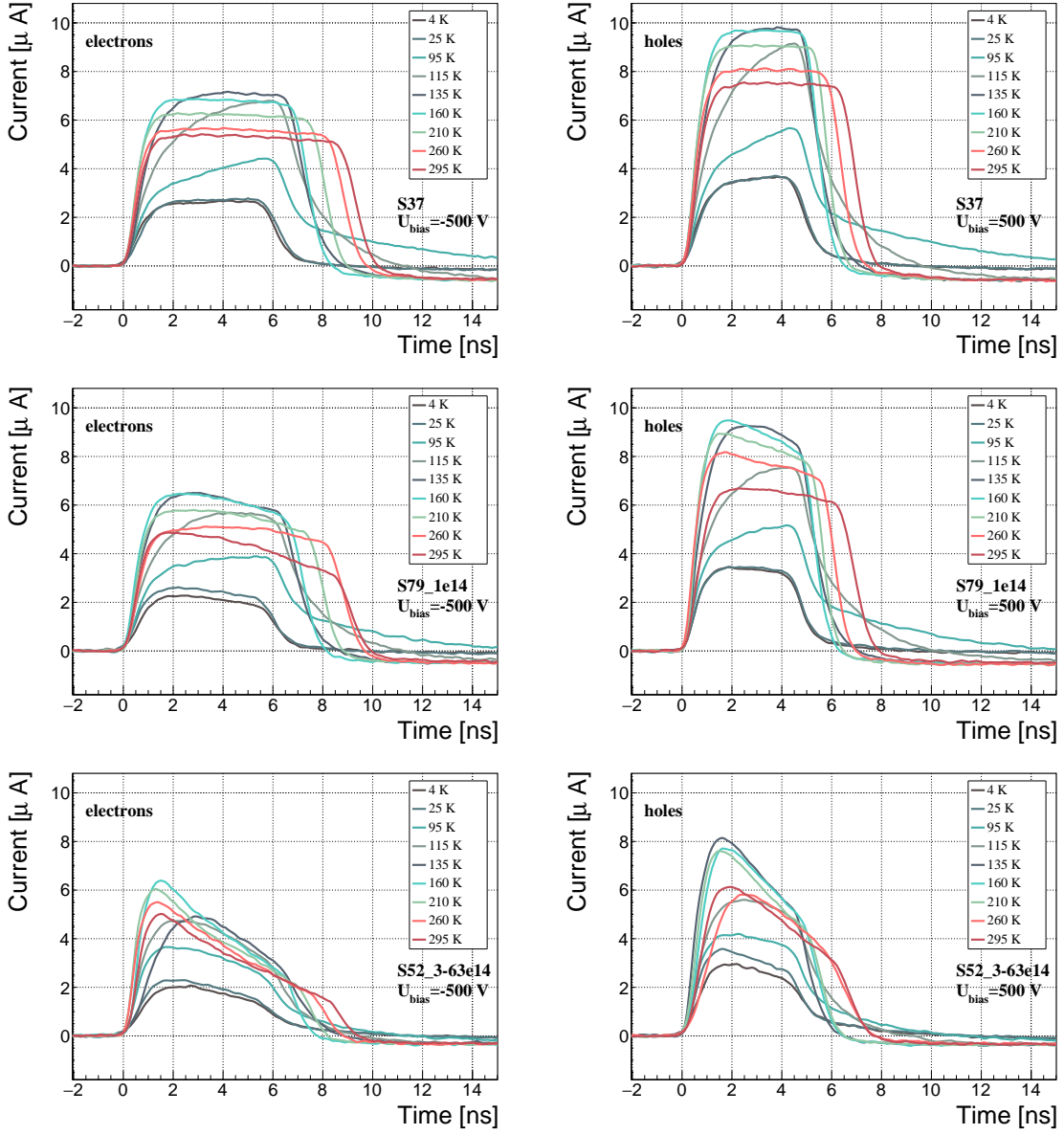


Figure 3.16: After irradiation: several data points between 4 K and 295 K at a bias voltage of ± 500 V

the drop in charge below 150 K. The new contribution are the data points for the irradiated samples. The values for them are lower than those of non-irradiated samples, which is expected.

The values for all samples are fairly stable in the range between 4 K and 75 K and between 150 K and 295 K. However, in the values for the irradiated S52 some excursions can be observed. This is due to the sequence of the measurement steps, which introduced a hysteresis effect and is explained in the preceding text.

The collected charge drops significantly from 150 K down to 75 K. In the non-irradiated samples the values in the lower temperature range are approximately 0.30

of the values at the high range. For the irradiated ones this difference is lower – a factor of 0.35 for S79 and 0.5 for S52. An interesting detail is that the ratio between the values for non-irradiated samples and their irradiated counterparts at the lower range is different than at the higher range. Looking at the values for the electron collection in figure 1.17a: for S52 the lower ratio is equal to 1.28 and the higher equal to 1.7. For S79 these ratios are 1.00 and 1.09, which means that the difference in charge collection between 4 K and 75 K before and after irradiation is negligible.

3.4.2.2 Charge trapping

The carriers drifting through the bulk get stopped by the charge traps with a certain probability. This trapping happens uniformly throughout the diamond, decreasing the number of carriers in the charge cloud. Therefore the absolute number of trapped carriers decreases. At the same time the absolute number of trapped carriers per unit of length decreases. The resulting function for the number of drifting carriers per unit of length is a decaying exponential function:

$$I(t) = I(0) \cdot e^{-\frac{t-t_0}{\tau}} + I_0, \quad (3.6)$$

where $I(0)$ is the initial induced current, I_0 is the end current, t is time, t_0 is temporal displacement of the pulse and τ is the decay time constant. This value tells how long it takes before the amplitude of the pulse decreases to 63 % of its initial height.

The decaying exponential function has been fitted to the decaying top of the averaged pulses at bias voltages of ± 400 V and ± 500 V across all temperatures excluding the transitional range between 75 K and 150 K. The resulting decay time constants τ for an individual temperature point are not equal, which stems from the fact that the pulses change with time due to “polarisation”. This counts as a systematic error. Therefore the fitted τ for ± 400 V and ± 500 V are averaged into one value representing the measurement at that temperature point. Figure 1.18a shows the fitted τ for the five samples between 4 K and 295 K. In principle, the time constants should be infinite for a perfect and non-irradiated sample. Here a slightly tilted top of the pulse due to space charge is already successfully fitted with an exponential function, resulting in a τ of the order of (200 ± 20) ns⁻¹. Consequently the fitting method is not adequate for non-irradiated samples. For the irradiated samples, the fit becomes increasingly more meaningful. As seen in figure 1.18a, the fitted values of the irradiated samples are fairly stable across all temperatures. There is a slight increase in the decay time constant of the S52 from (6.0 ± 0.5) ns⁻¹ above 150 K to (8.5 ± 0.9) ns⁻¹ below 75 K. On the other hand, this step is not observable in the S79 data. With only one sample exhibiting this behaviour, the effect is not significant enough. Judging by the data acquired, the samples would need to be irradiated to doses above $1 \times 10^{14} \pi \text{ cm}^{-2}$ to quantify this effect in detail. So far this effect will not be regarded as significant for the scope of this thesis. Building on this assumption, the conclusion is that the signal decay time constant for irradiated sCVD diamond is constant across the temperature range between 4 K and 195 K, excluding the transitional range between 75 K and 150 K.

3.4. TEMPERATURE LIMITATIONS

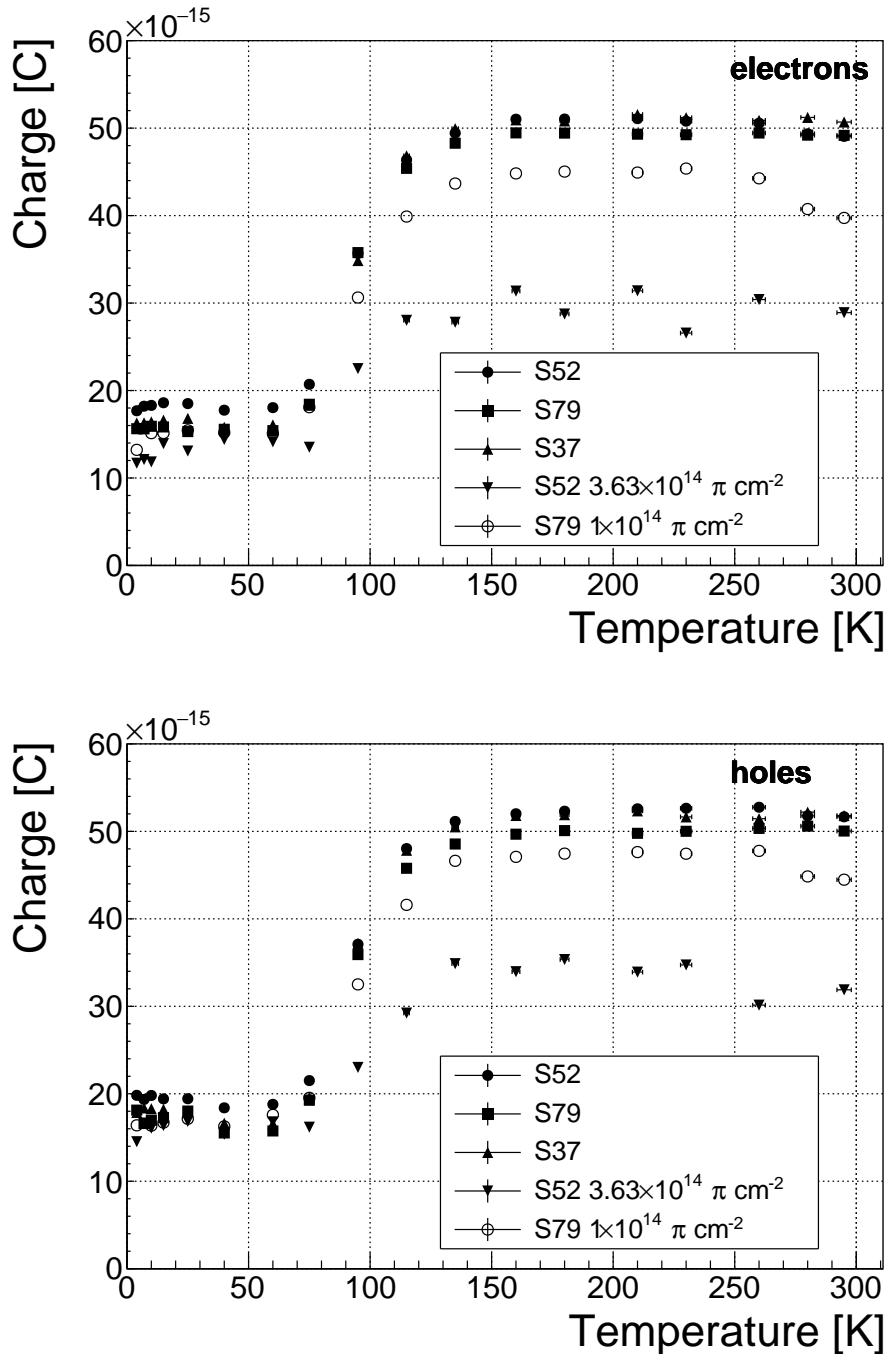


Figure 3.17: Collected charge as a function of temperature

¹⁶⁰¹ Taking into account the conclusions above, all the values can be averaged into one
¹⁶⁰² decay constant. Figure 1.18b shows these values for all samples as a function of the
¹⁶⁰³ received $\pi_{300 \text{ MeV}}$ radiation dose. To estimate the carrier lifetime with respect to the
¹⁶⁰⁴ radiation dose received, a similar model is used than that in section 1.5. This model
¹⁶⁰⁵ states that the inverse of the carrier lifetime is linearly decreasing with increasing

CHAPTER 3. EXPERIMENTAL RESULTS
DIAMOND IRRADIATION STUDY

1606 radiation dose:

$$\frac{1}{\tau} = \frac{1}{\tau_0} + \kappa_\tau \cdot \Phi \quad (3.7)$$

1607

$$\tau = \frac{\tau_0}{\kappa_\tau \tau_0 \Phi + 1} \quad (3.8)$$

1608 where τ_0 is the lifetime for a non-irradiated sample (real lifetime, therefore of the order
1609 of 400 ns^{-1}), τ is the lifetime of an irradiated sample, Φ is the received radiation dose
1610 and κ_τ the lifetime degradation factor. For these data the fitted factor is equal to
1611 $\kappa_\tau = (3.6 \pm 0.8) \times 10^{-16} \text{ s cm}^2 \pi_{300 \text{ MeV}}^{-1}$. Using this factor, the steepness of the decay
1612 in the pulse shape with respect to radiation dose can be estimated. This can help
1613 when designing a system where current pulse shape is an important factor.

3.4. TEMPERATURE LIMITATIONS

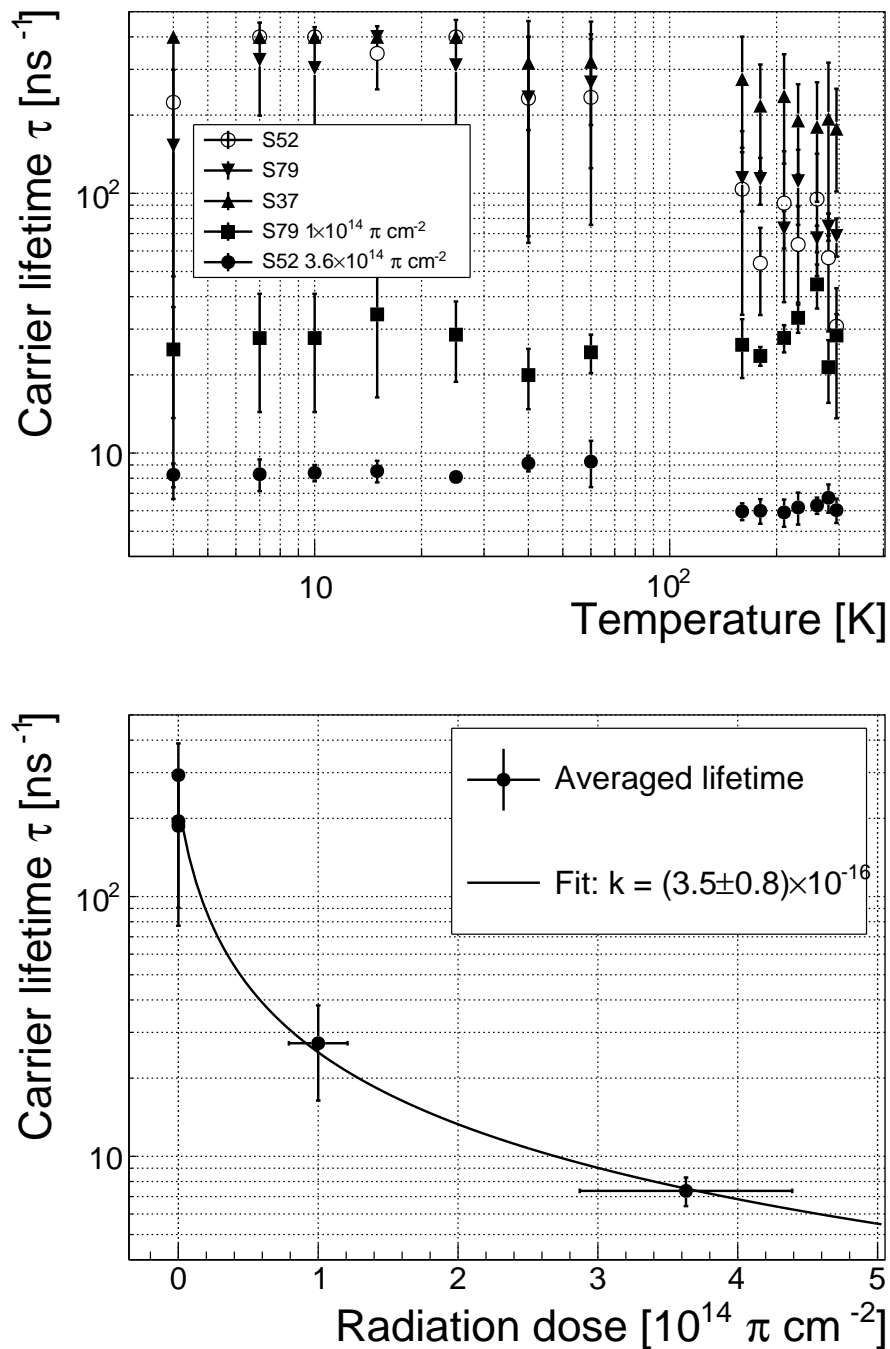


Figure 3.18: Charge carrier lifetime decreases with irradiation, but is stable across the range of temperatures between 4 K – 75 K and 150 K – 295 K. The first figure shows the carrier lifetime τ as a function of temperature whereas the second figure depicts the carrier lifetime averaged over all temperatures and plotted against the π irradiation dose

¹⁶¹⁴ **3.5 Conclusion**

¹⁶¹⁵ This chapter gives an overview of the capabilities and limitations of diamond as
¹⁶¹⁶ a particle detector. Three effects on diamond were studied – noise, radiation and
¹⁶¹⁷ temperature, the focus being on the latter two.

¹⁶¹⁸ Two sCVD diamond detectors were irradiated with 300 MeV pions. They were
¹⁶¹⁹ tested alongside a non-irradiated sample to observe the changes in the ability to detect
¹⁶²⁰ α , β and γ radiation. Their charge collection efficiency was measured in a test beam
¹⁶²¹ facility using . The results were compared to the results from the RD42 collaboration
¹⁶²² and a DPA model. A radiation damage factor $k_\lambda = (3.0 \pm 1.0) \times 10^{-18} \mu\text{m}^{-1} \text{cm}^{-2}$ was
¹⁶²³ obtained for $\pi_{300 \text{ MeV}}$ particles. The data point was not in agreement with the data
¹⁶²⁴ provided by RD42 nor with the model. However, the irradiation process and the low
¹⁶²⁵ number of tested samples hold a relatively high statistical uncertainty. In addition,
¹⁶²⁶ there was no diamond surface treatment done in between the measurements, as is the
¹⁶²⁷ case in the study conducted by RD42. The results obtained in the course of these
¹⁶²⁸ measurements will also be fed into the existing pool of data in the RD42 collaboration.

¹⁶²⁹ The next step was to test the long-term capabilities for α detection. The shape
¹⁶³⁰ of the ionisation profile was investigated to determine the behaviour of the charge
¹⁶³¹ carriers in the irradiated diamond. An exponential decay was observed in the pulses
¹⁶³² of irradiated samples, proving that there are charge traps in the bulk that were created
¹⁶³³ during irradiation. Then a long-term stability test was carried out. The results show
¹⁶³⁴ that the irradiated diamond detectors do not provide a stable and reliable long-term
¹⁶³⁵ measurement of α particles. This might be due to a space-charge build-up in the
¹⁶³⁶ bulk, which changes the electric field, affecting the charge carriers. A procedure to
¹⁶³⁷ improve the pulse shape using β and γ radiation was proposed.

¹⁶³⁸ Finally, the diamond sensors were cooled down to temperatures between 4 K and
¹⁶³⁹ 295 K. Their response to α particles was observed. The results of the non-irradiated
¹⁶⁴⁰ and irradiated samples were compared. The effect of reduction for the number of
¹⁶⁴¹ drifting charges due to exciton recombination was observed in both sets of data.
¹⁶⁴² The second set had a superimposed effect of charge trapping during the drift, which
¹⁶⁴³ was represented by an exponential decay in the signal. The decay time constant
¹⁶⁴⁴ did not change with temperature. Therefore all temperature points for individual
¹⁶⁴⁵ samples were averaged and the decay time constants were plotted against the received
¹⁶⁴⁶ radiation dose. A damage factor equal to $\kappa_\tau = (3.5 \pm 0.8) \times 10^{-16} \text{ s cm}^2 \pi_{300 \text{ MeV}}^{-1}$ for
¹⁶⁴⁷ non-primed diamonds was defined.

₁₆₄₈ **Chapter 4**

₁₆₄₉ **Charge monitoring**

₁₆₅₀ ***The ATLAS Diamond Beam Monitor***

₁₆₅₁ Particle detectors in high energy physics experiments need to meet very stringent
₁₆₅₂ specifications, depending on the functionality and their position in the experiment.
₁₆₅₃ In particular, the detectors close to the collision point are subject to high levels of
₁₆₅₄ radiation. Then, they need to operate with a high spatial and temporal segmentation
₁₆₅₅ to be able to precisely measure trajectories of hundreds of particles in very short
₁₆₅₆ time. In addition, they need to be highly efficient. In terms of the structure, their
₁₆₅₇ active sensing material has to be thin so as not to cause the particles to scatter
₁₆₅₈ or get stopped, which would worsen the measurements. This also means that they
₁₆₅₉ have to have a low heat dissipation so that the cooling system dimensions can be
₁₆₆₀ minimised. Finally, they need to be able to operate stably for several years without
₁₆₆₁ an intervention, because they are buried deep under tonnes of material and electronics.

₁₆₆₂ The material of choice for the inner detector layers in the HEP experiments is
₁₆₆₃ silicon. It can withstand relatively high doses of radiation, it is highly efficient (of the
₁₆₆₄ order of $\sim 99.9\%$) and relatively low cost due to using existing industrial processes
₁₆₆₅ for its production. Its downside is that, with increasing irradiation levels, it needs to
₁₆₆₆ be cooled to increasingly low temperatures to ensure a stable operation. This is not
₁₆₆₇ the case with diamond. In addition, diamond has a lower radiation damage factor,
₁₆₆₈ which means it can operate in a radiation-heavy environment for a longer period.

₁₆₆₉ The ATLAS Diamond Beam Monitor (DBM) [] is a novel high energy charged
₁₆₇₀ particle detector. Its function is to measure luminosity and beam background in the
₁₆₇₁ ATLAS experiment. Given its position in a region with a high radiation dose, di-
₁₆₇₂ amond was chosen as the sensing material. The monitor's pCVD diamond sensors
₁₆₇₃ are instrumented with pixellated FE-I4 front-end chips. The pCVD diamond sensor
₁₆₇₄ material was chosen to ensure the durability of the sensors in a radiation-hard envi-
₁₆₇₅ ronment and the size of its active area. The DBM is not the first diamond detector
₁₆₇₆ used in HEP, but it is the largest pixellated detector installed so far (see figure 1.1).
₁₆₇₇ It was designed as an upgrade to the existing luminosity monitor called the Beam
₁₆₇₈ Conditions Monitor (BCM) [] consisting of eight diamond pad detectors, which is

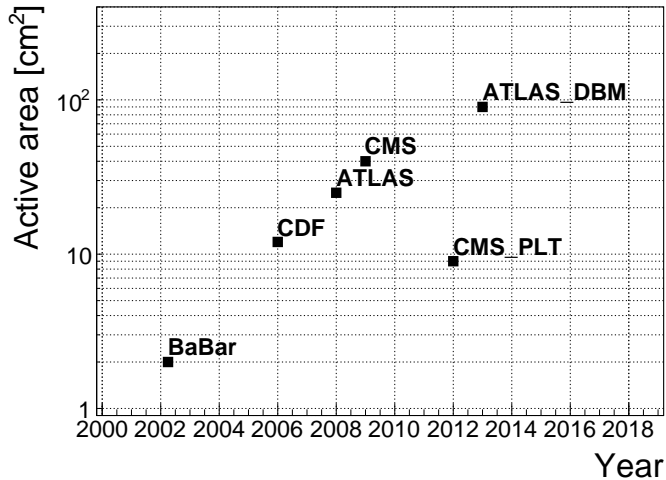


Figure 4.1: Diamond detectors installed in high-energy physics experiments in the last decade, sorted by the active sensor area. The first four detectors from the left are radiation monitors whereas the right two are pixel trackers.

able to perform precise time-of-flight (ToF) measurements. The DBM complements the BCM's features by implementing tracking capability. Its pixelated front-end electronics significantly increase the spatial resolution of the system. Furthermore, the DBM is able to distinguish particle tracks originating in the collision region from the background hits. This capability is a result of its projective geometry pointing towards the interaction region. This chapter first describes the principles of luminosity measurements. It then explains how the DBM will carry out this task. Finally, some results from tests and from the real collisions are presented.

When a particle traverses a sensor plane, a hit is recorded in the corresponding pixel. Thus, a precise spatial and timing information of the hit is extracted. With three or more sensors stacked one behind the other, it is also possible to define the particle's trajectory. This is the case with the DBM. Its projective geometry allows the particles to be tracked if they traverse the sensor planes. The DBM relates the luminosity to the number of particle tracks that originate from the collision region of the ATLAS experiment. Particles that hit the DBM from other directions are rejected as background radiation.

4.1 Luminosity measurements

Luminosity is one of the most important parameters of a particle collider. It is a measurement of the rate of particle collisions that are produced by two particle beams. It can be described as a function of beam parameters, such as: the number of colliding bunch pairs, the revolution frequency, the number of particles in each bunch and the transverse bunch dimensions. The first four parameters are well defined. However, the transverse bunch dimensions have to be determined experimentally

4.2. DIAMOND PIXEL MODULE

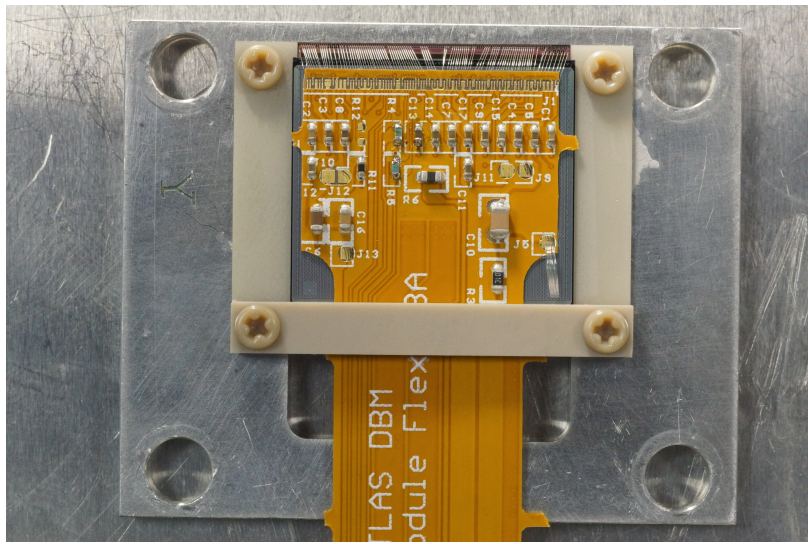


Figure 4.2: DBM module, top-down view. Visible is the flexible PCB with signal and power connections, the silicon sensor and a part of the FE-I4. Wire bonds from the PCB to the FE-I4 and to the sensor are also visible.

1702 during calibration. The ATLAS experiment uses the *van der Meer scan* [1] during
1703 low-luminosity runs to calibrate the luminosity detectors. This scan is performed
1704 by displacing one beam in a given direction and measuring the rate of interactions
1705 as a function of the displacement. Transverse charge density of the bunches can be
1706 estimated on the basis of the interaction rate. The calibrated luminosity detectors
1707 can then operate during high-luminosity runs.

1708 One approach to luminosity monitoring is to count the number of particles pro-
1709 duced by the collisions. The luminosity is then proportional to the number of detected
1710 particles. A detector has to be capable of distinguishing individual particles that fly
1711 from the interaction point through the active sensor area. If the detector has at least
1712 three layers, it can reconstruct the particles' tracks, which in turn yields more infor-
1713 mation on their trajectory. This is one reason why detectors with a high timing-
1714 and spatial segmentation are more suitable for these applications. The second reason
1715 is that, with a high spatial segmentation, the detector will not saturate even at high
1716 particle fluencies.

1717 4.2 Diamond pixel module

1718 The two most important parts of the diamond pixel module (seen in figure 1.2) are
1719 the sensor, which detects ionising radiation, and the pixellated front-end chip, which
1720 collects the ionised charge with a high spatial segmentation, processes the recorded
1721 data and sends them to the readout system. This section describes these two main
1722 parts of the module and their interconnection.

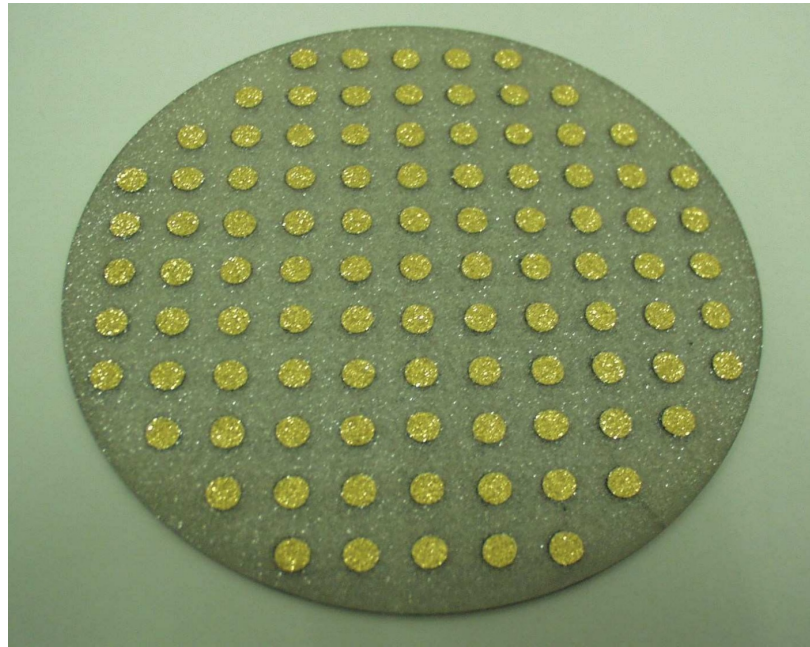


Figure 4.3: A pCVD wafer. The golden dots on the surface are the electrodes that are applied during the qualification test. The wafer is measured across the surface to find the regions with the highest efficiency.

1723 **4.2.1 Sensors**

1724 The DBM modules are instrumented with two types of sensors – pCVD diamond and
1725 silicon. The silicon sensors are used as a fallback solution because there were simply
1726 not enough high-quality diamond sensors available. In addition, a comparative study
1727 of irradiation damage between silicon and diamond can be made with such a hybrid
1728 system.

1729 **Diamond sensors** The target material for this application is pVCD diamond. The
1730 reason for this is that the active area of an individual sensor must be approximately
1731 4 cm^2 , which is too large for the sCVD diamond. pCVD material is also a bit
1732 cheaper, which makes a detector with a large active area more feasible to build. The
1733 material is provided by three companies: DDL, E6 and II-IV and it is grown in
1734 15 cm wafers, as seen in figure 1.3. The target thickness of the wafers is 500 μm and
1735 the minimum required charge collection efficiency is 40 % ($\text{CCD} \geq 200 \mu\text{m}$). They
1736 need to be operated at bias voltages between 600–1000 V. On one side there is a
1737 single gold electrode applied across the whole surface. On the other side a pixellated
1738 metallisation is added.

1739 **Silicon sensors** are standard $n^+ - in - n$ planar sensors with a 200 μm thickness
1740 and were mostly fabricated at CiS [], a company from Erfurt, Germany. They are
1741 designed to have nearly a 100 % efficiency when non-irradiated. Their bulk resistivity
1742 is between 2–5 $\text{k}\Omega\text{cm}$ and they were diffusion oxygenated at 1150 °C for 24 hours to

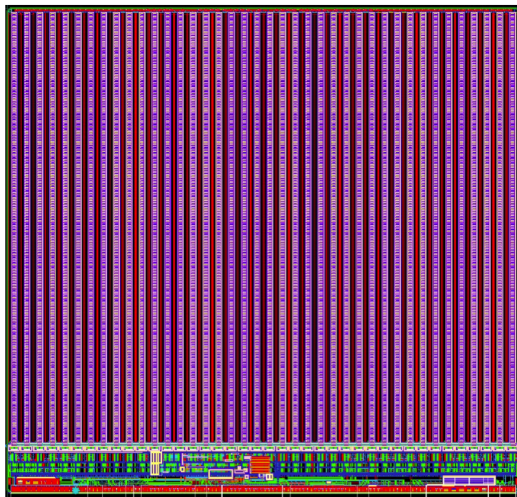


Figure 4.4: FE-I4 layout, top-down view. The pink area are pixels grouped into columns, the green area below is the common logic and the red strip at the bottom are the wire bond pads.

increase their radiation hardness. One side is segmented into pixels. Guard rings at the edges of the sensor provide a controlled drop in potential, reducing the possibility of shorts at maximum design bias voltages of the order of 1000 V.

4.2.2 Front-end electronics

The FE-I4 (front-end version four) [1] is an ASIC pixel chip designed specifically for the ATLAS pixel detector upgrade. It is built as a successor to the current pixel chip FE-I3, surpassing it in size of the active area ($4\times$ larger) as well as the number of channels/pixels ($10\times$ more). 336 such FE-I4 modules are used in the newly installed pixel layer called the Insertable B-Layer (IBL) [2]. The DBM is also instrumented with these chips. The FE-I4's integrated circuit contains readout circuitry for 26880 pixels arranged in 80 columns on a $250\text{ }\mu\text{m}$ pitch and 336 rows on a $50\text{ }\mu\text{m}$ pitch. The size of the active area is therefore $20.0\times16.8\text{ mm}^2$. This fine granularity allows for a high-precision particle tracking. The chip operates at 40 MHz with a 25 ns acquisition window, which corresponds to the spacing of the particle bunches in the LHC. It is hence able to correlate hits/tracks to their corresponding bunch. Furthermore, each pixel is capable of measuring the deposited charge of a detected particle by using the Time-over-Threshold (ToT) method. Finally, the FEI4 has been designed to withstand a radiation dose up to 300 MGy. This ensures a longterm stability in the radiation hard forward region of the ATLAS experiment.

Each pixel is designed as a separate entity. Its electrical chain is shown in figure 1.5. The bump-bond pad – the connection to the outside of the chip – is the input of the electrical chain, connected to a free-running amplification stage with adjustable shaping using a 4-bit register at the feedback branch. The analog amplifier is designed to collect negative charge, therefore electrons. The output is routed through

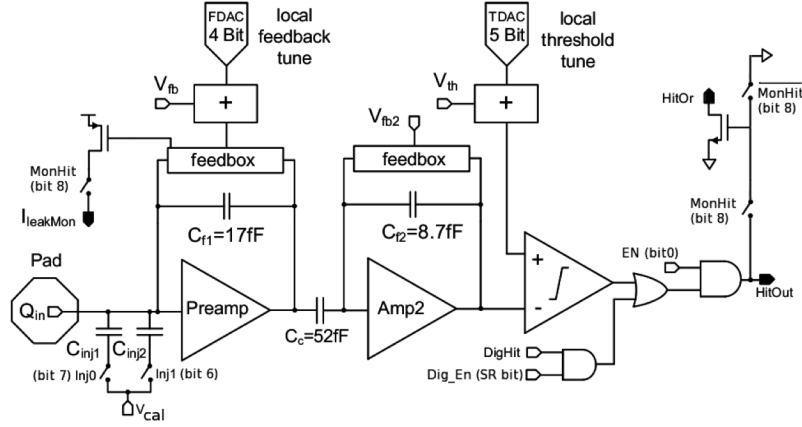


Figure 4.5: Schematic of an analog pixel. Courtesy of the FE-I4 collaboration.

a discriminator with an adjustable threshold. This value in effect defines the level at which the circuit will detect a hit. In addition, there is a counter of the clock cycles (25 ns sampling) during which the signal is above the discriminator threshold. The value of the counter is proportional to the collected charge. The logic gates at the end of the chain are used to enable/disable the pixel and to issue a so-called HitOr flag – this signal is set whenever at least one of the pixels was hit and is used as a trigger for the readout. The output of the chain – HitOut – is routed into the logic of the chip where it is buffered and eventually sent out to the readout system. The module receives all its commands from the system via a 40 MHz LVDS line. The commands are either settings for the pixel registers or triggers that start the data readout. The data are sent via an LVDS line at up to 320 Mbit/s, but by default at 160 Mbit/s, four times faster than the clock of the device. This allows the chip to clear out its buffers before new data are recorded, thus avoiding dead time and data pile-up. The FE-I4 has been successfully tested for trigger rates of up to 300 kHz.

The DBM uses pCVD diamond with $d_C = 500 \mu\text{m}$ thickness and silicon with $d_{Si} = 200 \mu\text{m}$ thickness as a sensor material. The resulting most probable value (MPV) of the deposited charge for a minimum ionising particle (MIP) is calculated with the formula $Q_S = d \cdot E_{e-h}$ and equals 18000 electrons and 17800 electrons, respectively, at a full charge collection efficiency. Unfortunately this is not the case with the pCVD material, whereby the expected charge collection efficiency is of the order of 50 % – around 9000 e. This value further decreases with received irradiation dose. Therefore in order to detect the particles depositing energy on the far left side of the landau spectrum, the threshold has to be set to a significantly lower value. On the other hand, if the threshold set too low, it also detects the electronic noise and stores a false noisy hit. With the typical noise amplitudes being in the range of 120–200 e, a safe threshold range would be between $Th = 1000\text{--}3000$ e. The target for the DBM is to lower the threshold down to 800 e.

The analog amplifier is implemented in two stages to get a fast rise time at a low noise and a low power consumption. The output signal of the analog amplifier has a

4.3. MODULE ASSEMBLY AND QUALITY CONTROL

triangular shape with a fast rise time and a long decay. The shape can be adjusted by tuning the amplifier feedback loop. Its length is proportional to the collected charge, but it needs to be calibrated first. This is done by means of two injection capacitors, $C_{\text{inj}1}$ and $C_{\text{inj}2}$, seen in figure 1.5 with well defined capacitances. First, the charge $Q_{\text{cal}} = V_{\text{cal}} \cdot (C_{\text{inj}1} + C_{\text{inj}2})$ is injected into the analog chain. Then the length of the output pulse is measured and finally the feedback value is changed to either lengthen or shorten the pulse in order to get to the required duration t_{cal} . The typical values are $Q_{\text{cal}} = 5000 - 16000$ e at the time $t_{\text{cal}} = 5 - 10$ ToT. The target values depend on the sensor, the type of a radioactive source and the application. Therefore the initial threshold Th at 1 ToT and the calibrated value Q_{cal} at t_{cal} ToT give us a linear scale of collected charge with respect to time over threshold. However, in practice this relation is nonlinear for lower thresholds, but since the goal of the measurements is to track the particles rather than to measure their deposited energy precisely, this is sufficient.

4.3 Module assembly and quality control

Parts for the detector arrived separately and were assembled into modules at CERN’s DSF lab after being checked for production faults. The assembled modules underwent a series of quality control (QC) and burn-in tests to determine their quality, efficiency and long-term stability.

4.3.1 Assembly

A single-chip module consists of a pixel module, a flexible PCB and the supporting mechanics (a ceramic plate and an aluminium plate). The chip arrives already bump-bonded to the sensor, be it diamond or silicon. First it is glued to the ceramic plate on one side and to the PCB on the other using either Araldite 2011 or Staystik 672/472. The choice of glue was a topic of a lengthy discussion. Staystik is re-workable and has a very high thermal conductivity. The latter is important because the FE-I4 chips tend to heat up significantly and need a good heat sink. The problem is that it has a curing temperature of 160/170 °C. This temperature may cause some unwanted stress build-up between the FE-I4 and the diamond sensor due to different coefficients of thermal expansion, pulling them apart. This would disconnect the pixels, yielding large regions of the module insensitive to radiation. To avoid this, an alternative glue was tried. Araldite 2011 can be cured at lower temperatures – down to RT – but it has a lower heat conductivity. In the end Araldite is used as the safer option. However, due to the longer curing, the whole assembly process using Araldite is extended to two working days. After curing, the module is wire-bonded and attached to the aluminium plate using screws made up of a radiation-resistant PEEK plastic. They have to be tightened with a great care, because their screw head is only 0.2–0.6 mm away from the sensor edge – the sensor displacement tolerance during gluing is of the order of 0.5 mm. Finally, the module is put in an aluminium carrier which protects

1835 it from mechanical damage or electrostatic discharges.

1836 **4.3.2 Testing**

1837 The modules are tested in the lab using an RCE readout system and a moving stage
1838 with two degrees of freedom. They are placed onto the stage and connected to the
1839 readout system and the power supplies. After ensuring the low- and high voltage
1840 connectivity they are checked for the signal connectivity. If everything is operational,
1841 a series of automated tests is run. Each of these tests calibrates a certain value within
1842 a pixel, whether it is the signal threshold or the value for integrated charge. These
1843 are tuned in a way that the response to a predefined calibration signal is uniform for
1844 all pixels across the sensor. This procedure is referred to as *tuning*.

1845 When the modules are tuned, they are tested using a ^{90}Sr radioactive source. Two
1846 things are checked: 1) operation of all pixels and 2) sensor efficiency. The first test
1847 is carried out by moving the module slowly under the source while taking data so
1848 that the whole surface is scanned uniformly. The resulting occupancy map reveals
1849 any pixels that are not electrically coupled to the sensor via bump bonds. This is an
1850 important step in the DBM QC procedure, because it turned out that a significant
1851 portion of the flip-chipped diamond sensors exhibited very poor connectivity. The
1852 disconnected regions on the faulty modules ranged anywhere from 0.5–80 % of the
1853 overall active surface. In two cases the sensor was even completely detached from the
1854 chip. Therefore the pixel connectivity turns out to be the most important qualification
1855 factor in the QC procedure. Unfortunately the only way to check it at the moment is
1856 to fully assemble a module and test it using a radioactive source. If the module turns
1857 out to be of poor quality, it is disassembled and sent for rework. The turnover time
1858 of this operation is of the order of one month, which affected the DBM installation
1859 schedule significantly.

1860 Only the modules that passed the pixel connectivity test undergo the second
1861 test stage in which the sensor’s efficiency was estimated. A scintillator is placed
1862 underneath the module and is used as a trigger. A particle that crosses the DBM
1863 module and hits the scintillator, triggers the module readout. In the end, the number
1864 of triggers is compared to the number of hits/clusters recorded by the module. The
1865 resulting ratio gives an estimate of the sensor’s detection efficiency. The real sensor
1866 efficiency can only be measured in a particle beam and using a beam telescope as a
1867 reference detector. Nonetheless, the *pseudo-efficiency* gives a rough estimate of the
1868 sensor’s quality.

1869 The results for the DBM QC are shown in section 1.4. All in all, 79 modules went
1870 through the QC procedure – 43 diamond modules and 36 silicon modules, 12 of the
1871 latter only for testing purposes. Figure 1.6 shows their production with time. 18
1872 diamond modules and 6 silicon modules were in the end chosen to be made up into
1873 DBM telescopes and installed into ATLAS.

1874 A very important issue is the so called erratic current. This term describes the
1875 leakage current in a pCVD diamond that becomes unstable. It can develop gradually

4.3. MODULE ASSEMBLY AND QUALITY CONTROL

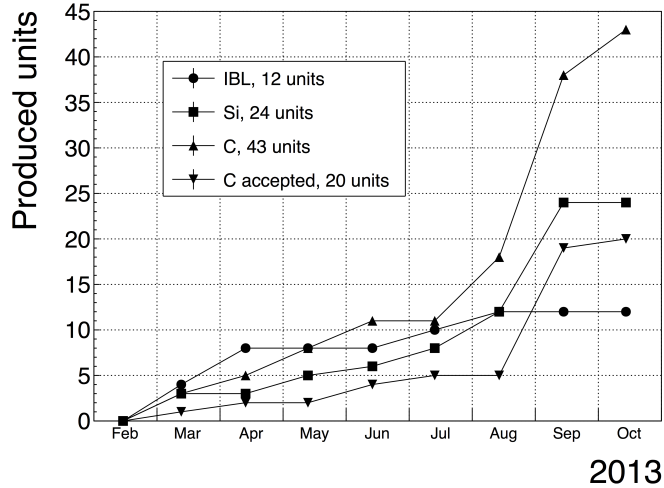


Figure 4.6: Module production with time

or can be triggered with a β source. Spikes appear in the otherwise stable leakage current. They can be up to three orders of magnitude higher than the base current. Sometimes the current also suddenly increases for a few orders of magnitude and stays at that level (e.g. from the initial 1 nA to 3 μ A). The amplitude differs in magnitude from sensor to sensor. This effect is still not fully explained, but the hypothesis is that the charges find a conductive channel along the grain boundaries, causing discharges. These discharges are picked up by the pixel amplifiers in the FE-I4. A single discharge can trigger a group of up to \sim 500 pixels, resulting in a *blob* on the detector occupancy map. Sometimes the conductive channel stays in a conductive state, making one or more pixels always to fire. These pixels only use the bandwidth of the readout channel, so they have to be masked out during measurements.

4.3.3 Installation and commissioning

The DBM modules that passed the QC tests were assembled into telescopes – sets of three modules one behind the other with a spacing of 50 mm. Of the 18 diamond and 6 silicon modules, 6 diamond and 2 silicon modules were built. A special care was taken when choosing the sets of three diamonds. The modules with a similar pseudo-efficiency, leakage current, maximum stable high voltage and shape of disconnected regions were grouped together. After assembly into telescopes, the modules were tested for their connectivity. Then the high voltage was applied and the leakage current was observed. This was an important point to check because all three modules shared the same high voltage channel. Any instabilities on one of the modules would cause problems on the other two. This would for instance happen if one of the modules had a much lower breakdown voltage.

Due to time constraints, the telescopes were not built at the same time but instead the production was pipelined. As soon as two telescopes were ready, they were transported to Point 1 – the site where parts of the ATLAS detector were being put

1902 together. There they were prepared for installation onto the pixel detector struc-
1903 ture that had been extracted from ATLAS due to pixel detector commissioning. The
1904 commissioning was nearing completion, so the technicians were preparing the detec-
1905 tor for re-insertion. The cylindrical structure was being closed off by four new service
1906 quarter-panels (nSQPs). This meant that with every day the access to the place
1907 of installation of the DBM was more difficult. The first two telescopes were still put
1908 into place when only one nSQP was in place. This allowed the installation process
1909 to be carried out from both sides. This proved to be helpful, because the process
1910 was lengthy and had to be done with great precision. It involved tightening several
1911 screws on both sides of the telescopes, adding thermal paste on the aluminium joints
1912 and removing the protective covers, revealing the fragile wire bonds. At the same
1913 time the surrounding electronics and cables had to be left untouched. The lessons
1914 learnt with the first part of the installation were helpful when installing the other tele-
1915 scopes. The last two were fitted onto the structure when three nSQPs were already
1916 in place, leaving only a narrow opening for access. The whole procedure was carried
1917 out blind. After every installation, the telescopes were tested again. First, the low
1918 voltage connectivity was checked and a set of tests was run on the FE-I4 front-end
1919 chips. An eye diagram was made to estimate the quality of the signal transmission.
1920 Then a ^{90}Sr source was used to perform a source test on three modules at the same
1921 time. Leakage current was observed during the source test. The final test included
1922 running four telescopes (all on one side) at a time. All the tests were successful and
1923 the DBM was signed off.

1924 **4.4 Performance results**

1925 This section gives an overview of the performance results of the DBM modules
1926 achieved during the QC and the test beam campaign. The source tests were per-
1927 formed to check for disconnected regions in the sensors and to measure the diamond's
1928 pseudo-efficiency. Only the modules with minimal disconnected regions and maxi-
1929 mum pseudo-efficiency were chosen for installation.

1930 **4.4.1 Source tests**

1931 All modules went through the same procedure when tested using a ^{90}Sr source – to
1932 check for disconnected regions and to measure the pseudo-efficiency.

1933 The setup consisted of a placeholder for the ^{90}Sr source, an X-Y moving stage
1934 with a holder for the module and a scintillator with a photomultiplier placed below
1935 the source and the module. The scintillator was used as a trigger – when it detected a
1936 particle, it triggered the readout of the module. If the module was placed in between
1937 the source and the scintillator, the particle had to traverse the module to hit the
1938 scintillator. Therefore, in the case of a module with a 100 % efficiency the triggered
1939 data read out by the module would need to contain at least one hit in the module. In
1940 reality the β particles scatter around the setup and sometimes hit the scintillator from

4.4. PERFORMANCE RESULTS

other directions, without incident the module. This produces empty triggers. The phenomenon sets the limitation of measuring with a radioactive source as compared to the measurements in a test beam, in which the particles in principle always travel in one direction and their scattering is minimal.

The test for disconnected regions was carried out by moving the module under the source in X and Y direction so that the exposure over the whole plane was uniform. This resulted in an occupancy scan seen in figures 1.7a and 1.7b. The silicon module had a very uniform occupancy plot. So much so that the features of the overlaying flexible PCB can be observed. The rectangular shadows are the passive components whereas the lines are the traces in the PCB. Furthermore, a circular-shaped edge of the PCB can be seen on the bottom right side of the plot. These darker areas are such because fewer electrons can penetrate the material with a high density. In the case of the diamond, the features of the PCB can be observed as well, but are much less distinguishable. In principle, the plot is much more granulated – less uniform. This high variance in the diamond’s detection ability is due to the grain boundaries in the pCVD material which trap the drifting charges, rendering some regions much less efficient.

The pseudo-efficiency test was carried out by placing the module directly below the source and collimating the particles so that their trajectory was incident the module in the middle. For every trigger by the scintillator, a script checked whether there was a hit recorded in the module or not. The resulting ratio between the number of triggers and number of hits recorded in the module is a pseudo-efficiency – an estimation of the sensor’s efficiency. It cannot give a precise value due to the triggers produced by scattered particles, but at least gives a rough estimate.

Figure 1.8a shows the distribution of disconnected regions across all tested modules. Silicon modules were performing as expected, with a minimum number of disconnected pixels. The majority of the silicon modules yielded the pseudo-efficiency of $(94.3 \pm 0.2) \%$. Silicon sensors being 99.99 % efficient, this value was underestimated by about 5 %. The measured pseudo-efficiency of the diamond modules was $(65 \pm 7) \%$, with outliers down to 10 %. The value depended on the diamond quality, the set threshold and the applied bias voltage. The latter two settings were varied to check the behaviour of the modules under various conditions.

4.4.2 Test beam results

The first two assembled prototype DBM modules, MDBM-01 and MDBM-03, were tested at DESY, Hamburg, in a test beam facility. The aim of the measurements was to measure their efficiency, the spatial distribution of the efficiency and the effect of the beam on the disconnected regions. A silicon module MSBM-02 was measured to crosscheck the measurements. Since the silicon module is almost 100 % efficient, it was used as an “anchor” – the efficiency of the diamond module was measured relative to that of the silicon module. Two beam telescopes were used as reference systems: Kartel [], built by JSI institute from Ljubljana, and EUDET Aconite []. Both are

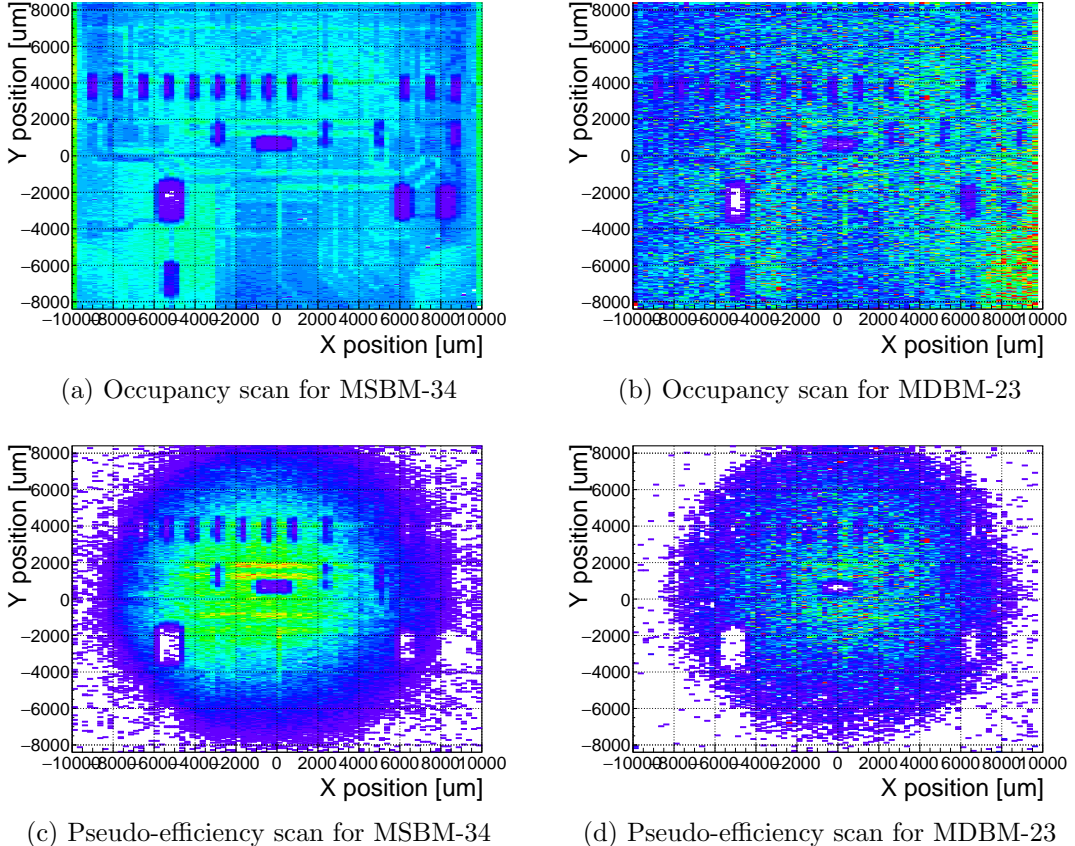


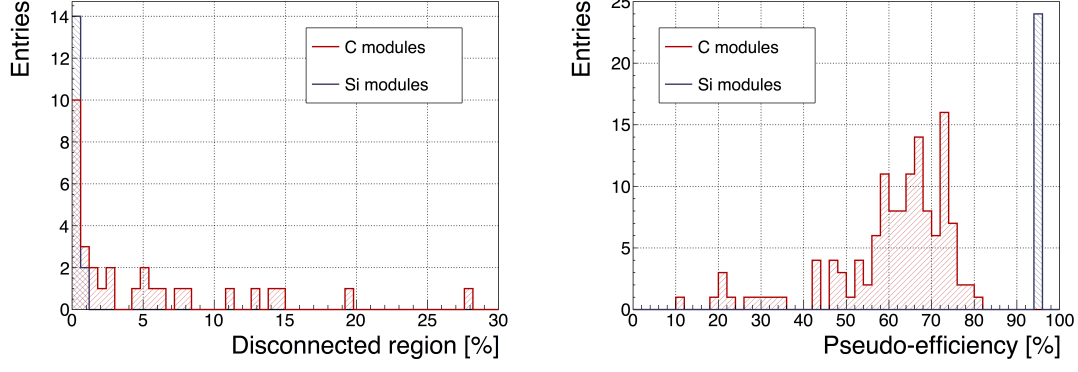
Figure 4.7: Occupancy and pseudo-efficiency scans for the silicon (left) and diamond sensor (right) to check for disconnected regions and estimate the sensor’s efficiency. Shadows of the electronic components are clearly visible because fewer electrons were able to traverse through such a higher amount of material.

instrumented with six Mimosa26 pixel planes and capable of tracking particles with a $2 \mu\text{m}$ pointing resolution.

The test beam prototypes did not meet the acceptance criteria for production DBM modules in the following areas: first, the stated CCDs were slightly below $200 \mu\text{m}$, which would be the DBM minimum. Secondly, the applied bias voltages ranged from $1\text{--}2 \text{ V}/\mu\text{m}$. In addition, the threshold cut could only be set to 1500 electrons, which is higher than the DBM minimum (1000 e). Nonetheless, the resulting module efficiencies were still in the range between 70–85 %.

To analyse the test beam data, Judith [] software framework was used. Judith is capable of synchronising data streams from several detector systems only connected via a trigger system, reconstructing tracks and calculating efficiency for the DUTs. It was also used to reconstruct and analyse the acquired Kartel test beam data together with the silicon and diamond module as DUTs. A sample of the analysed data is shown in figures 1.9a and 1.9b.

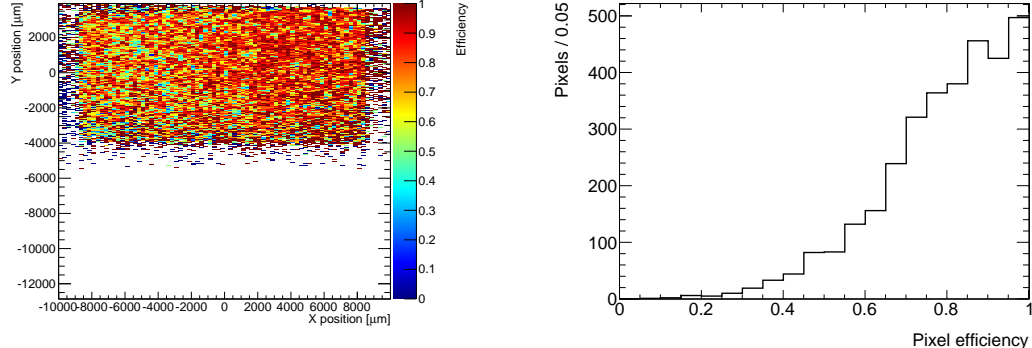
4.5. OPERATION



(a) Disconnected regions for all modules derived from the occupancy scans

(b) Pseudo-efficiencies for all modules at various threshold and voltage settings

Figure 4.8: Measurements of pseudo-efficiency and disconnected regions for all modules that went through the QC procedure



(a) This is an efficiency distribution. Each bin corresponds to a single pixel. The triggering scintillator of the Kartel telescope was smaller than the DUT. Hence, the recorded hits can only be seen in the top half of the sensor.

(b) Pseudo-efficiencies for all modules at various threshold and voltage settings

Figure 4.9: An efficiency study of a prototype DBM diamond module in a test beam. The statistics are low (~ 10 hits/pixel) as the data was collected during a short run.

4.5 Operation

4.5.1 Positioning

The DBM is placed in the forward region of the ATLAS detector, very close to the beam pipe (see figure 1.11). The mechanical structure that holds the sensor planes is, due to its shape, referred to as a DBM telescope. A telescope is a system that consists of several pixel sensors placed in series one behind the other. Each DBM telescope houses three diamond pixel modules. Eight DBM telescopes reside approximately 1 m away from the collision region, four on each side. They are tilted with respect



Figure 4.10: This photo highlights four telescopes installed onto the nSQPs and around the pipe

2004 to the beam pipe for 10°. This is due to a specific phenomenon connected to erratic
2005 (dark) currents in diamond. Studies have shown [1] that the erratic leakage currents
2006 that gradually develop in diamond can be suppressed under certain conditions. For
2007 instance, if a strong magnetic field is applied perpendicular to the electric field lines
2008 in the diamond bulk, the leakage current stabilises [2]. The DBM was designed to
2009 exploit this phenomenon. The magnetic field lines in the ATLAS experiment are
2010 parallel to the beam. Hence, an angular displacement of the sensor with respect to
2011 the beam allows for the leakage current suppression. However, the DBM telescopes
2012 still need to be directed towards the interaction region. Taking these considerations
2013 into account, a 10° angle with respect to the beam pipe was chosen. The influence
2014 of the magnetic field on the particle tracks at this angle is very low as the field lines
2015 are almost parallel to the tracks. The tracks are therefore straight, which reduces the
2016 track reconstruction complexity.

2017 4.5.2 Data taking during collisions

2018 The DBM has been commissioned in ATLAS and is now taking data. Several issues
2019 still need to be resolved regarding the readout systems. Unfortunately, due to issues
2020 with the low voltage power supply regulators, six out of 24 modules were damaged
2021 during operation: four silicon and two diamond modules. The system configured

4.5. OPERATION

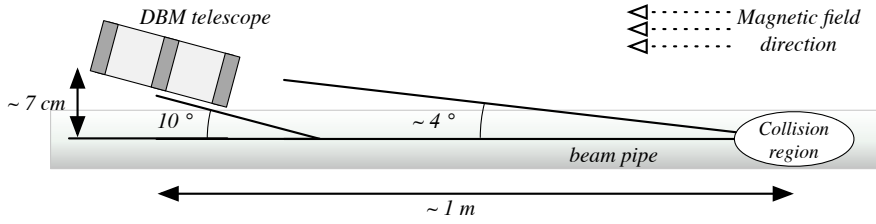


Figure 4.11: Position of the DBM in the ATLAS experiment

FIGURE PLACEHOLDER

Figure 4.12: Occupancy of individual modules during collisions. Only 16 modules were taking data.

2022 the modules into an unsteady state whereby they drew twice as much current as the
 2023 allowed maximum. This current most probably fused the wire bonds within minutes.
 2024 This has left only five diamond telescopes fully operational. The preliminary data
 2025 obtained using the remaining telescopes show that the background rejection could
 2026 indeed work.

2027 The first step of the system test was to take data during collisions and check
 2028 the occupancy in the individual modules. The occupancies were plotted side by side
 2029 for comparison. Figure 1.12 shows some of the occupancy values. At the time, the
 2030 readout system was not yet configured to read out all telescopes in parallel.

2031 The second step was to test the detector's capability of particle tracking. Only one
 2032 telescope was used to take data with the beam. If all three planes of the telescope
 2033 were hit during a bunch crossing, a linear line was fitted to the hits. This line
 2034 represented the particle's trajectory. It was projected towards the interaction point.
 2035 Two parameters were calculated where the line is the closest to the interaction point:
 2036 the radial distance and the longitudinal distance between the line and the interaction
 2037 point (see figure 1.13). This was done for the events with two colliding bunches as
 2038 well as for events with only one, non-colliding bunch. The tracks recorded during
 2039 the events with two colliding bunches could either come from the collisions or could
 2040 be background scattering. Tracks recorded during a non-colliding bunch, on the
 2041 other hand, are definitely background particles since, in principle, there should be no
 2042 collisions taking place.

2043 A comparison of the data acquired (see figures 1.14a and 1.14b) showed that, for
 2044 the colliding bunches, the majority of the reconstructed tracks had the origin in the
 2045 interaction point, with an expected spread in Z and R . For non-colliding bunches,
 2046 the distribution is more spread out. In the Z_0 plot the distribution has one peak in
 2047 the middle, which means that the empty RF buckets still held some particles. The
 2048 two peaks on the sides, however, show that a significant number of tracks had their
 2049 origin at the radius of the beam pipe. Therefore these tracks were made by stray
 2050 protons colliding with the beam pipe. These collisions are unwanted as they do not

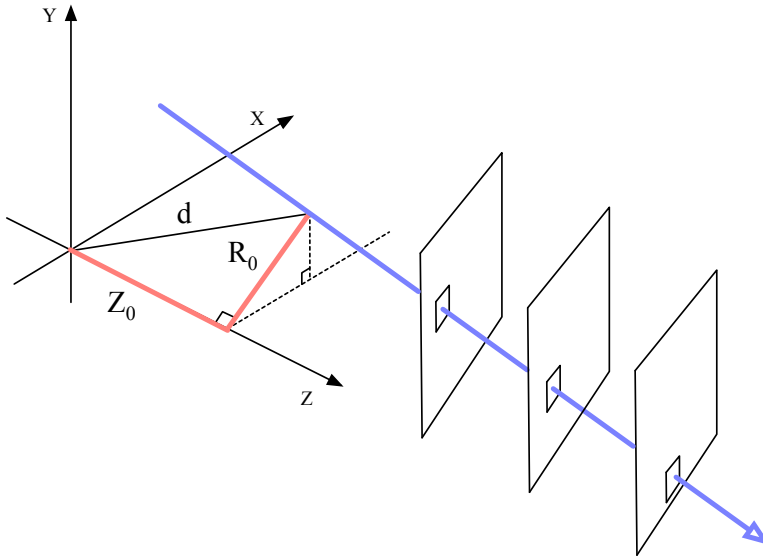


Figure 4.13: A diagram showing the radial distance R_0 and longitudinal distance Z_0 of the trajectory from the interaction point at the minimal distance d . Z is the axis along the beam line. Three module planes intercept a particle and reconstruct its trajectory.

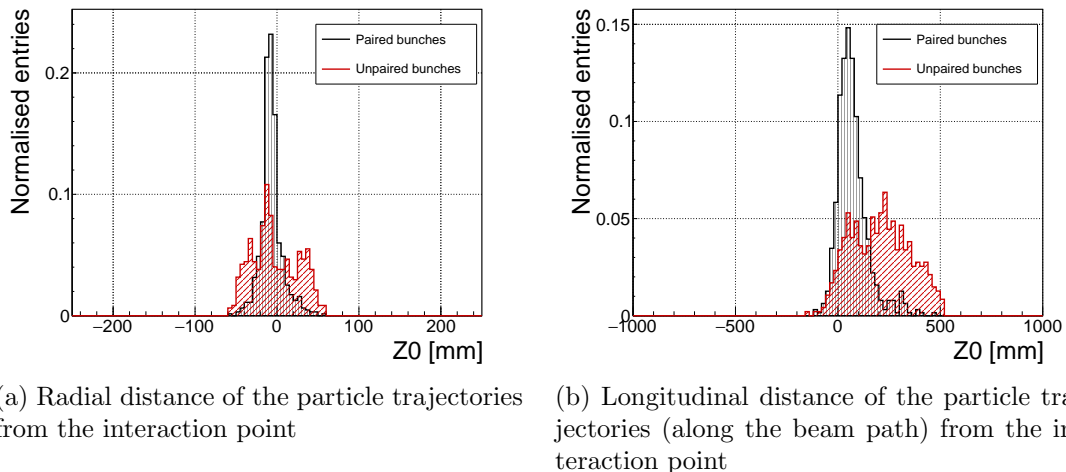


Figure 4.14: These two plots show two parameters of particle tracks recorded by one of the DBM telescopes: radial and longitudinal distance of the projected tracks from the interaction point.

2051 produce any meaningful physics while still damaging the ATLAS detector by means
2052 of the scattered radiation.

2053 **4.6 Conclusion**

2054 The Diamond Beam Monitor has been designed as an upgrade to the existing lu-
2055 minosity detectors in the ATLAS experiment. It is the first diamond pixel tracking
2056 detector installed in a high-energy physics experiment. The pixelated front-end elec-
2057 tronic chips ensure precise spatial detection of the charged high-energy particles.
2058 The projective geometry allows for particle tracking and background rejection. The
2059 detector is placed in a high-radiation forward region of the experiment. Therefore,
2060 radiation hardness of the chosen pCVD diamond sensors is an important requirement.
2061 The tests carried out in the test beam and in the laboratory confirmed that enough
2062 detector-grade DBM modules have been built to be installed in the experiment. The
2063 DBM is now running in ATLAS during collisions. Further improvements have to be
2064 made on the readout firmware before it is included in the main readout stream.

2065

Chapter 5

2066

Current monitoring

2067

Real-time particle identification

2068 Diamond sensors have a very fast signal response due to their low capacitance. The
2069 electrical signal created by drifting charge carriers retains its shape without significant
2070 distortion. When the sensor is used together with a fast current amplifier with a high
2071 broadband limit (~ 2 GHz) and a readout device with a similar limit, the information
2072 about the drifting charges is retained. For instance, a proton creates the free e-h pairs
2073 along its trajectory. The electrons and holes start drifting immediately. Those closest
2074 to the electrodes recombine quickly whereas those at the opposite side contribute to
2075 the induced signal for longer. The resulting signal is therefore a triangular pulse
2076 with a steep rising edge and a gentle falling edge. It is possible to determine the
2077 drift velocity of the charge carriers by measuring the width of the pulse, as was done
2078 in chapter [??](#). Furthermore, it is possible to determine with a certain probability
2079 what is the type of incident radiation, judging by the shape of the induced pulse.
2080 This, however, only applies to sCVD diamond material. Its uniform carbon lattice
2081 allows the ionisation profiles to retain their shape, unlike in pCVD material, laden
2082 with grain boundaries, or in even in silicon where the shape is deformed due to p-n
2083 junction non-uniformities.

2084 This chapter describes an application that carries out particle identification by
2085 means of the pulse shape analysis. It was developed for measuring activity of a
2086 neutron reactor. In this case the device has to be able to filter out the photon
2087 background with a rate several orders of magnitude higher than the neutron rate.
2088 Overall detected rate in a neutron reactor can easily exceed 10^8 particles $\text{cm}^{-2}\text{s}^{-1}$,
2089 depending on the distance of the detector from the reactor core. The device has to
2090 be able to cope with such high rates. It also needs to be dead time free or at least
2091 close to that, to minimise the counting error. At these rates, it still has to be able to
2092 identify the types of pulse. This type of online analysis cannot be done in software.
2093 It has to be implemented in an FPGA.

5.1 MOTIVATION

5.1 Motivation

Pulse shape analysis (PSA) is a common software tool for analysing sensor response to incident particles. It is usually done by means of software that runs over big amounts of data that have been acquired and saved to storage. This offline analysis can be repeated and improved. However, the saved data take up a lot of storage space. In addition, saving raw waveform data requires a system capable of a high data throughput and fast data storing. For instance, an oscilloscope can save up to 100 signal waveforms per second. This means that there is a high measurement dead time. To avoid the high dead times, the software algorithms can be ported to the FPGA where they analyse the incoming signal in real time. The signal is then discarded and only the analysis results are saved, decreasing the storage space significantly.

The offline pulse shape analysis has already been used for particle identification with a diamond sensor [29, 24]. An effort has been made to implement an online and real time application for this analysis by porting the algorithms into an FPGA. This section first describes the device specifications Then it describes in detail the PSA algorithms and the structure of the code. Afterwards it discusses the performance results, which showcase the limitations of the device. Finally it describes the data acquired with radioactive sources and in neutron reactors.

5.2 Requirements

Chapter ?? shows that the shape is heavily dependent on several factors, such as environmental temperature and received irradiation dose. At temperatures lower than 150 K the signal from an α starts deteriorating due to recombination of charges in the charge cloud. Sensor irradiation, on the other hand, introduces charge traps, which cause the signal to decay exponentially. These two factors are a significant limitation for particle identification. Priming can improve the charge collection and longterm stability of the pulse shapes. To improve the measurement further, a high bias voltage has to be applied, increasing the measurement SNR.

Factor	Operating range
Sensor material	sCVD diamond
Sensor thickness	500 μm
Temperature	150 K – 400 K
Radiation dose	$1 \times 10^{13} \text{ neq cm}^{-2}\text{s}^{-1}$
Charge carriers	holes
Bias voltage	$\sim 1 \text{ V } \mu\text{m}^{-1}$
Signal-to-noise	5

Table 5.1: Limitations to particle identification

2124 5.3 Device specifications

2125 The ROSY box has a single BNC input with the termination $50\ \Omega$ or $1\ M\Omega$ with a
2126 DC or AC coupling. The analog chain has a 250 MHz bandwidth limit. The input
2127 range can be set from $\pm 50\text{ mV}$ up to $\pm 5\text{ V}$. The signal offset can be set to any value
2128 within this range. The ADC samples this signal with an 8-bit precision at a rate of
2129 up to 5 GSPS. The PSA uses the highest sampling to achieve width measurement
2130 resolution of 0.2 ns. The spectroscopic application does not need such a fine timing
2131 resolution and therefore operates at a reduced sampling rate of 0.8 ns. The amplitude
2132 resolution depends on the chosen input range, but at 256 ADC counts per sample, it
2133 can be as low as 0.39 mV s^{-1} at the range of $\pm 50\text{ mV}$ and as high as 39 mV s^{-1} at
2134 the range of $\pm 5\text{ V}$.

2135 The logic structure of the PSA is designed using VHDL and runs on Xilinx Virtex 5. The PSA is capable of a maximum counting rate of 1.56×10^8 pulses per second,
2136 yielding a 6.4 ns double pulse resolution. The analysis is more time consuming; the
2137 maximum throughput rate of the pulse shape analysis is $\sim 5 \times 10^6$ pulses per sec-
2138 ond. This means that after every pulse, the device has a dead time of approximately
2139 (200 ± 15) ns, depending on the width of the pulse being analysed. Any pulse arriving
2140 during the analysis of the previous one will be counted, but not analysed. Any two
2141 pulses with the distance between the rising edges lower than 6.4 ns will be counted
2142 as a single pulse.

2143 The device is very sensitive to noise pick-up. Therefore the setup must be designed
2144 to minimise the pick-up by means of proper shielding, use of high-quality cables etc.
2145 The relatively low bandwidth limit filters out some high-frequency noise, but not the
2146 ringing or higher noise spikes. That is the task for the PSA.

2148 5.4 Pulse parameters

2149 A signal pulse on the input is parametrised during the analysis process. The PSA
2150 measures its amplitude, area, width and the slope of its falling edge (see figure 1.1).
2151 The amplitude is the difference between the baseline and the highest sample in the
2152 pulse and is given in ADC counts as an 8-bit value. The area is defined as the sum
2153 of amplitudes of all samples between two defined boundaries within the pulse. The
2154 width is defined as the number of samples with a value higher than a set amplitude
2155 threshold. If the threshold is at half the maximum amplitude, the resulting width
2156 is *full width at half maximum* (FWHM). The falling slope is the maximum negative
2157 difference between values of two samples and is given in ADC counts per sample.
2158 These parameters can also be used as *qualifiers* for accepting or discarding a pulse.
2159 All four parameters limited by the low and high limit are called a *qualifier set*. For
2160 instance, a rectangular pulse by an α particle will always have the same FWHM and
2161 a very steep slope. In comparison, a photon will have a lower falling slope value and
2162 a narrower FWHM. Therefore the low and high cut on these two qualifiers will make
2163 it possible to discriminate between the two pulses. Another qualifier is a *form factor*

5.5. APPLICATIONS

and is defined as the ratio between the measured area and the amplitude multiplied by the width. By comparing the measured and the calculated area the difference between a triangular and a rectangular pulse can be inferred.

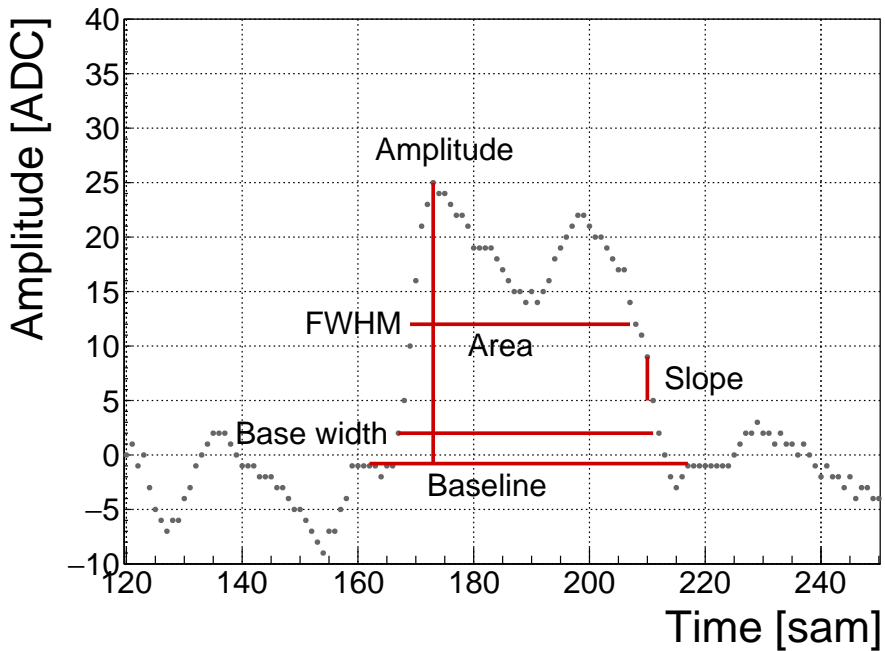


Figure 5.1

5.5 Applications

The FPGA firmware is designed for systems instrumented with CIVIDEC amplifiers and CIVIDEC sVCD diamond detectors. Three applications are available: *Spectroscopy*, *Pulse Shape Analysis* and *Counter*, each optimised for a specific task. Their capabilities are described below. The firmware runs in ROSY, a readout system produced by CIVIDEC.

Spectroscopy is a tool for measuring energy spectra of radioactive sources. It is used in combination with the CIVIDEC Cx spectroscopic charge amplifier. The signal from the charge amplifier is analysed in real time. The FPGA measures the maximum amplitude of the signal. The amplitude value is ready at the end of the pulse and is stored in the amplitude histogram. Immediately after, the analysis is reset and the system is ready for a new acquisition. Upon request from the software, the histogram is read out, during which the analysis is paused. In addition to the histogram building, the firmware can also store raw pulse waveforms, which can be then read out by the software. The maximum allowed throughput is 1 million counts per second.

2183 **Pulse Shape Analysis** is a tool for measuring energy spectra of radioactive sources,
2184 with an additional feature. It can identify the type of radiation detected by the
2185 diamond detector. By means of the pulse analysis it can subtract the background
2186 radiation and only measure the signals from the defined radiation source. It is used
2187 in combination with the CIVIDEC C2 fast current amplifier. The firmware receives
2188 a current pulse from the detector and digitises it. The pulse is then analysed and
2189 parametrised. The analysis module measures its maximum amplitude, full width
2190 at half maximum (FWHM), baseline amplitude, falling slope and its area. Then
2191 it compares the obtained pulse parameters with the qualifiers set by the software
2192 and determines what type of radiation hit the diamond detector. Depending on the
2193 qualifiers, the pulse can either be *accepted* or *rejected*. The firmware then stores the
2194 parameters of the analysed pulse into histograms. Two histograms exist for each
2195 parameter: one for all pulses and one for accepted pulses. In addition, there is one
2196 2D histogram (a scatter plot), which can plot two parameters one with respect to the
2197 other. Upon request from the software, all histograms are read out, during which the
2198 analysis is paused. The maximum allowed throughput is 1 million counts per second.

2199 **Counter** is a tool that measures the count rate and the mean time during counts.
2200 It is used in combination with the CIVIDEC Cx, C6 or C2 amplifier. It contains
2201 one histogram which holds the information about the mean time during counts. The
2202 counter is operational also during the readout of the histogram. The highest counting
2203 rate with enabled histogram writing is $3 \times 10^7 \text{ s}^{-1}$.

2204 5.6 Description of the firmware

2205 The applications are built on top of the Picotech platform. The base code handles
2206 the communication between the software and the hardware. Furthermore, it provides
2207 the interface to the ADC data, the input/output registers and the USB data transfer.
2208 The applications have a set of modules that handle the data input and output and
2209 a module for signal analysis (see figure 1.2).. The data handling modules are very
2210 similar in all the applications to ensure compatibility of the communication between
2211 software and firmware and the readout data format. The analysis module, however,
2212 is different from one application to the other. The data handling layer is the same for
2213 all applications and consists of the final state machine (FSM), the histogram builder,
2214 the raw signal handler, the USB FIFO buffer and the register array.

2215 The firmware is written entirely in VHDL. The diagram in figure 1.2 shows the
2216 module architecture. The ADC provides the module with 32 digitised signal samples
2217 every clock cycle (6.4 ns). The signal is routed directly to the pulse analyser and
2218 into the raw signal handler. The analyser outputs are connected to the I/O registers
2219 and to histogram buffers. Both the histogram buffers and raw signal buffers are
2220 connected to the USB FIFO through a multiplexor. The firmware communication to
2221 the controller is done via input/output (I/O) registers (control and status registers,
2222 counters) and serially via USB (histogram data, waveforms).

5.6. DESCRIPTION OF THE FIRMWARE

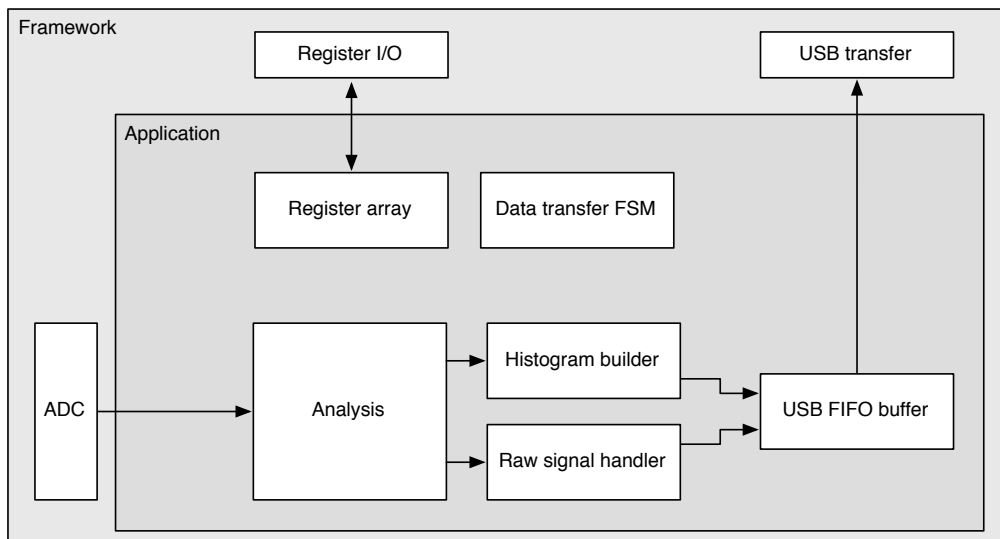


Figure 5.2: Firmware design structure

5.6.1 Analysis module

This module is different for different applications. The Pulse Shape Analysis (PSA) application has the most complex module design. The spectroscopy application only uses a small part of that design and the Counter application an even smaller one.

The analysis (or parametrisation) is carried out in several steps. The triggering block starts the readout upon signal threshold crossing. The maximum slope of the falling edge is observed. The Amplitude block calculates the pulse height and retains the maximum amplitude while pushing the signal into the pulse buffer. Then the whole pulse is clocked out of the buffer while its FWHM, baseline width and area are measured. Finally, the Form factor is calculated. At the end the Evaluation block takes in all the parametrised information and classifies the pulse according to user-defined cuts.

Triggering module handles signal polarity swapping, triggering on threshold and defining the trigger window. The real-time processing algorithm allows for a positive or an inverted input signal. However, the PSA only handles positive-polarity pulses. Therefore a negative signal is swapped in the *triggering* block. Signal analysis and readout are then triggered when the signal crosses a user-defined threshold. In addition, the signal has to be over the threshold for a defined number of samples. This is to avoid triggering on noise spikes. A double clock cycle delay is used on the signal to make sure that the recorded signal window will include the rising edge of the pulse as well as some baseline before it. A *trigger active* signal marks a window that contains the whole pulse including some baseline signal before and after it. The trigger can be vetoed by three signals: if the pulse analysis is still taking place, if the input signal exceeds the maximum voltage range or if the data transfer FSM is pausing the analysis due to data transfer to the controller.

2248 **Amplitude** block calculates the pulse height from the difference between the pulse
2249 and the baseline. It also finds the position of the maximum amplitude within the
2250 clock cycle. It receives 32 8-bit samples from the triggering block every clock cycle.
2251 Time delays in the logic prevent it to find the maximum value of the 32 samples
2252 within one clock cycle (6.4 ns). Therefore the decision logic has been pipelined in
2253 three stages, which means that the final maximum value is ready three clock cycles
2254 after the end of the pulse.

2255 **Pulse buffer** is a FIFO that stores the signal while its amplitude is being measured.
2256 At the end of the pulse the FIFO is read out so that the remaining measurements
2257 can take place.

2258 **FWHM** block uses the maximum amplitude to determine the *half-maximum* and to
2259 measure the FWHM. To do so, it counts the samples that are above the half-maximum
2260 amplitude. However, this method might also count high enough noise spikes before
2261 or after the pulse. Hence an improved method, which “cleans” the measurement of
2262 unintentional additional noise, has been implemented. It is described in section 1.6.2.

2263 **Baseline width** block is the same as the FWHM block, but it measures the width
2264 either at 50 %, 25 %, 12.5 % or 6.25 %, depending on the setting in the register. It
2265 also makes use of the special method described in 1.6.2 to avoid overestimations due
2266 to including noise in the measurement.

2267 **Area** block measures the pulse area by summing up the amplitude values of the sam-
2268 ples in the pulse. The boundaries of the summation are defined with the crossing of
2269 the amplitude above a certain threshold. Only the samples between those boundaries
2270 are summed up. The boundaries can be set at 50 %, 25 %, 12.5 % or 6.25 % of
2271 the maximum amplitude of the pulse. The area measurement makes use of the same
2272 routine as the FWHM and Baseline width block to remove the potential outlying
2273 samples.

2274 **Falling slope** block measures the highest negative difference between amplitudes of
2275 two adjacent samples, thus getting the maximum negative slope of the pulse. It is an
2276 experimental routine, only used for academic purposes.

2277 **Form factor** block is used as a special qualifier for particle identification. It com-
2278 pares the weighted measured area of the pulse with its weighted calculated “form”,
2279 which is defined as the multiplication of the measured amplitude and baseline width.
2280 The equation is as follows:

$$x \cdot a - y \cdot A \cdot BW \geq 0, \quad (5.1)$$

2281 where a is the measured area, A is the amplitude, BW is the baseline width and x
2282 and y the weighting factors for the measured and calculated area, respectively. The
2283 output of the block is the boolean result of this equation.

5.6. DESCRIPTION OF THE FIRMWARE

Evaluation block takes in all the parameters from the analysis blocks and compares them against the user-defined qualifiers. If the parameters are within the bounds, the pulse is accepted, otherwise it is rejected. The corresponding counters within the block are incremented.

5.6.2 Vector cleaning for area and width measurements

The routine for measuring pulse area and width was designed to improve the measurements with respect to the previous implementation. The core difference is that the new routine precisely defines the edges of a pulse. It does so by means of *vector cleaning*, presented in figure 1.3. An important input, beside the ADC data and the measurement threshold, is the position of the sample with the highest amplitude.

The signal arrives from the ADC as a set of 32 8-bit samples every every clock cycle with a period of 6.4 ns. All 32 samples are compared against the width measurement threshold. If a sample value is equal or higher than this threshold, a binary 1 is set in a 32-bit *vector* on the position corresponding to the position of the sample in the incoming ADC data set. The resulting vector might also include some noise at the edges of the pulse, depending on the height of the width measurement threshold. The old routine simply counts the binary ones in this vector to get the pulse width. This works well for measuring the FWHM because the threshold was high. However, for width measurements at 25 %, 12.5 % or 6.25 % of the pulse height this might already become a problem, because the noise might be counted in as well. This is why the new routine cleans the outliers in this vector before counting the remaining ones in the clean vector.

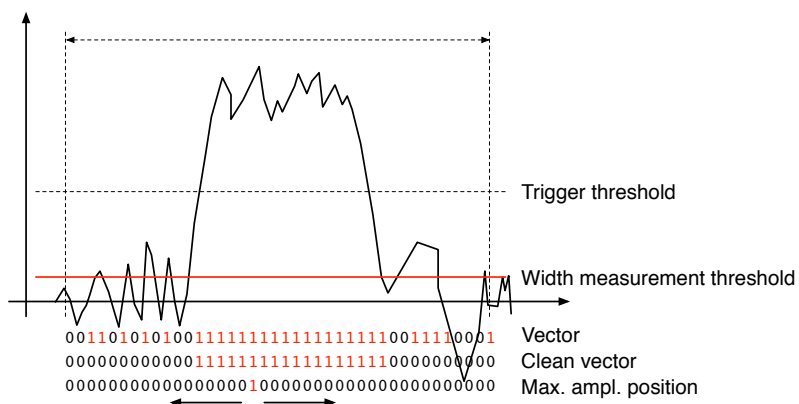


Figure 5.3: A sample pulse. The first vector shows which samples are above the width measurement height. The second vector is a clean vector. The third line shows the position of the maximum amplitude. The vector cleaning algorithm starts from the maximum amplitude and continues in both ways along the vector.

The routine starts from the position of the maximum height. It follows the vector in both ways and finds the first falling edge (0 at this position and 1 at the previous one). From there on it rewrites any binary 1 with a binary 0. The resulting clean

vector only has one bunched set of binary ones which are summed, yielding a precise pulse width. The area measurement is similar - it only integrates over the samples marked in the clean vector. Both measurement routines, for area and for width, are implemented separately so that the area routine can have a different threshold set.

This section explains how the algorithm is designed. First, the idea for it was tested using Excel and was only afterwards ported to the VHDL. The underlying algorithm first cleans the vector. Then it passes the cleaned vector either to the width or area measurement (see figures 1.4a, 1.4b, 1.5a and 1.5b). The width measurement module only sums the ones in the vector whereas the area measurement module sums the data samples marked by the cleaned vector. Both modules issue a *valid* signal when they finish the measurement.

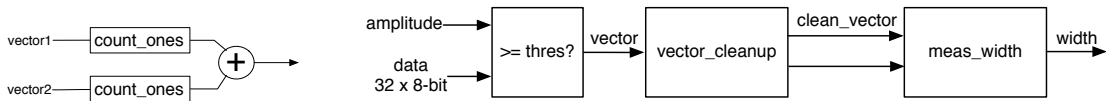


Figure 5.4: This block counts the remaining binary ones in the clean vectors and outputs this value as the pulse width.

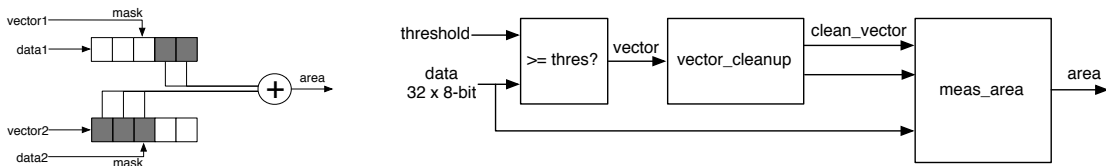


Figure 5.5: This block masks the input data with the clean vector and sums the remaining samples.

5.6.2.1 Vector cleaning

This is the most important block. Its inputs are: *vector*, *parsing active*, *position of the max. amplitude (PA)* and *its delay (DA)*. PA is a 32-bit binary number that shows the position of the sample with the maximum amplitude within the data block whereas the DA tells us how many clock cycles after the start of the parsing this PA block is. The vector cleaning module is designed as a final state machine (FSM) with the states IDLE, RISEEDGE, PEAK, FALLEDGE and READY. The FSM is idle until it receives the *active* signal from the external module, marking that the vector parsing has commenced. It switches to RISEEDGE, which starts two procedures: 1) it fills the vector of the pulse's rising edge into a last-in-first-out (LIFO) buffer and 2) counts down from the DA value. When this counter reaches 0, the FSM changes its state to PEAK because the current vector on the input is the one containing the maximum amplitude. This data block is sent through the *peak algorithm*, which cleans the vector. The FSM switches to FALLEDGE state. Now both the previously buffered

5.7. CONTROL AND DATA INTERFACE

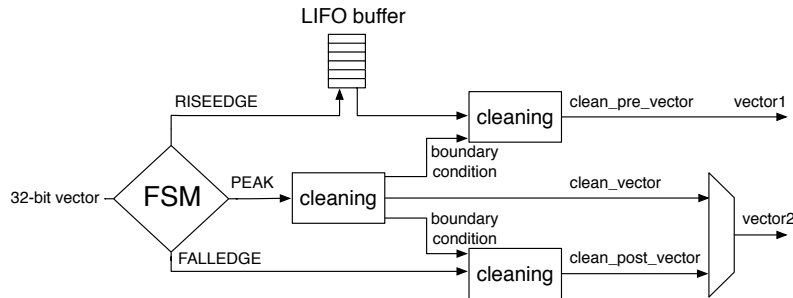


Figure 5.6: Vector cleaning routine outputs two vectors - one forward in time and one back in time from the peak of the pulse.

2334 vector of the rising edge and current vector of the falling edge go through the *pre-*
 2335 *and post- algorithm* where they are cleaned, but they get their boundary conditions
 2336 from the *peak algorithm*. The output of this module is therefore two cleaned vectors
 2337 in parallel – one forward in time and the other backwards.

2338 5.6.2.2 Algorithm

2339 The underlying algorithm is sequential - it carries out a logic operation on vector bit
 2340 0, uses the output of this operation for the operation on bit 1 and so on. This means
 2341 that it has to carry out 32 logic operations per clock cycle. With each operation taking
 2342 approximately 0.3 ns, the whole logic chain takes approximately 10 ns to complete.
 2343 With only 6.4 ns per clock cycle, this means timing errors would occur. To fix the
 2344 problem, a more complicated *decimated algorithm* was invented. It consists of two
 2345 parallel logic chains which only take every second bit into account and are at the end
 2346 merged together. This effectively reduces the number of sequential logic operations
 2347 to around 18, which is within the timing constraints.

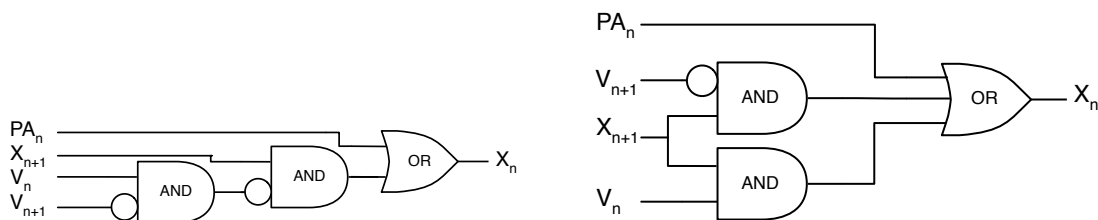


Figure 5.7: One logic step in the algorithm chain before and after Karnaugh minimisation.

2348 5.7 Control and data interface

2349 Communication between the Picoscope and the controller PC is done via the Picotech
 2350 API functions. In addition to the functions provided to the Picoscope users, the API

used by CIVIDEC has access to several extra functions. These allow the user to download a customised bitfile to the FPGA, access the I/O registers and use the USB data transfer.

5.7.1 Software

The software has been designed in C++ in several levels of abstraction. Figure 1.8 shows the structure of the classes. The classes Picoscope, PSA and RawSignalHandler are there to make it easier to read and understand the controller code. In principle the PSfunctions can also be accessed directly by the controller, but for this the instruction sequences must be well known and understood.

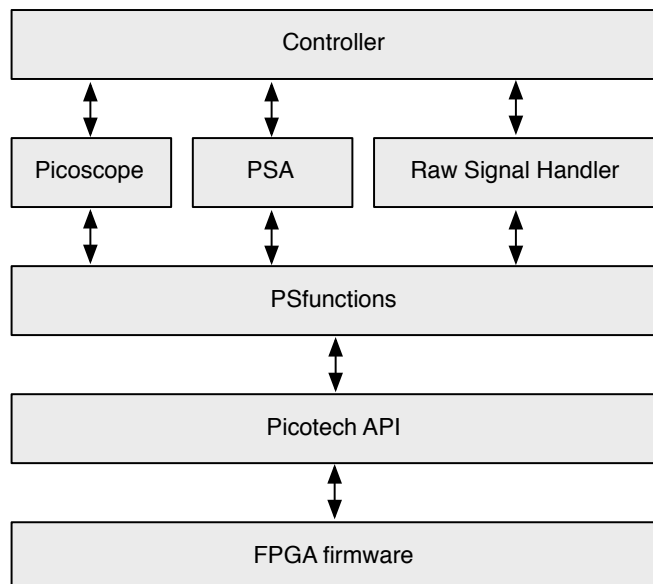


Figure 5.8: Abstraction levels of the controller software

5.7.2 Data readout

The device records the data in two forms - as signal waveforms and as histograms of analysed pulse parameters. Both are available upon request from the controller. Only one of the two can be transferred via the USB line at a time.

The waveforms are saved into a FIFO buffer, which can hold up to 64 pulses of the length of ~ 500 samples. The data format for each pulse is such that it starts with a header containing the pulse timestamp and the sequential number, continues with the data samples and ends with a header containing all the measured parameters (width, amplitude, area, falling slope and form factor). When the FIFO is full, it issues a flag, which tells the controller that the data buffer is ready for readout.

The histograms are implemented into the FPGA's Block RAM. Their size ranges from 256 to 4096 bins (an 8-bit or a 12-bit histogram, respectively), depending on the

5.7. CONTROL AND DATA INTERFACE

2372 required histogram resolution. For instance, the width parameter is measured with a
2373 0.2 ns resolution; the expected maximum pulse width is less than 20 ns. This yields
2374 the maximum range of 100 bins, making an 8-bit histogram sufficiently large. The
2375 same reasoning is applied to the amplitude measurement. In this case the maximum
2376 range is defined by the 8-bit resolution of the ADC. The area measurement, however,
2377 yields higher values and can therefore have a more refined binning (12-bit). Finally,
2378 a single 12-bit 2D histogram is included, with 6 bits for every axis. It is used as an
2379 online scatter plot for comparing one measured parameter to another. An example
2380 for it is a comparison of the width against the area, which can help the user determine
2381 the cuts that need to be applied to the measurement.

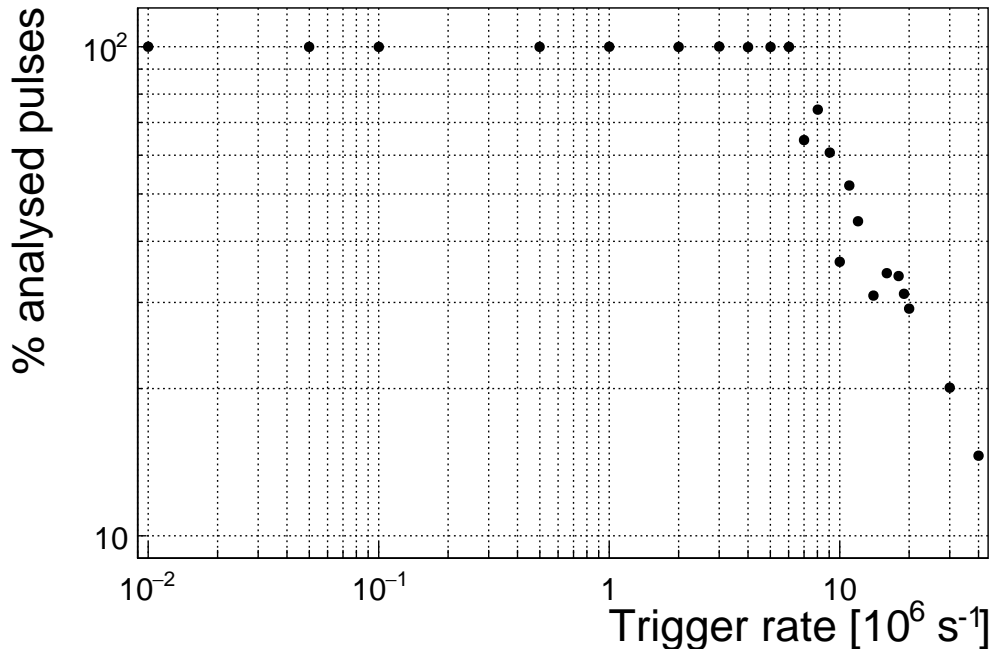


Figure 5.9: This figure shows the capability of the device to analyse all arriving pulses for a range of input frequencies. The highest achievable rate with zero lost pulses is $5 \times 10^6 \text{ s}^{-1}$.

5.8 Performance results

The device has been tested in the lab using a pulse generator as well as several radioactive sources. The results show that: 1) the amplitude, area and width measurement are linear across all input ranges, 2) the highest rate of the PSA algorithm is $\sim 5 \times 10^6$ pulses per second and 3) the lowest SNR where the algorithm still functions is ~ 5 .

Trigger rate A pulse generator was used to verify the highest achievable rate at which the PSA still analyses every incoming pulse. The final state machine implemented in the pulse analysis module prevents the triggering block from issuing a trigger due to an incoming pulse if the previous analysis is still in ongoing. Given that all the pulses were of the same length, the analysis duration was always the same. When the time between the incoming pulses was shorter than the time of the analysis, the pulses were not analysed. Figure 1.9 shows the sharp decline in the percentage of the analysed pulses when reaching the rate of 5 MHz. Therefore the overall analysis duration for a 10 ns pulse is approximately 200 ns.

Linearity A pulse generator was used to verify the linearity of the measurements across all input ranges. Pulse width and amplitude were varied and measured both with the oscilloscope and the PSA to check for non-linearities or inconsistencies in the PSA measurements. The resulting plots in figures ?? and 1.10c show that the PSA measurements agree well with those from the oscilloscope. The major inconsistency

5.9. SOURCE CALIBRATION

2401 is observed in the lower range of the plots. It stems from the fact that the bandwidth
2402 limit of the PSA is lower than that of the oscilloscope, which affects the pulse shape.
2403 Effectively, the PSA cannot measure the rectangular pulses of the width smaller than
2404 2 ns.

2405 **Stability** The input pulse signal was superimposed with white noise generated by
2406 a noise generator with a variable gain. The mixed signal yielded pulses with an
2407 SNR ranging from 5 (very noisy) to 100 (noise negligible). The PSA then performed
2408 the pulse parametrisation at different SNRs. The resulting plots in figures 1.10b,
2409 1.10d and 1.10e show that the pulse width measurement is stable even for low SNR
2410 whereas the amplitude measurement is affected significantly. This stems from the
2411 analysis taking the highest sample as the pulse's amplitude. The area measurement,
2412 being effectively the integrated amplitude across the pulse, is also affected by the
2413 faulty amplitude measurement. Nevertheless, the mean area remained the same.
2414 This means that the added noise only affects the resolution of the spectrum, not its
2415 position.

2416 5.8.1 Comparison between the charge- and current-sensitive 2417 spectroscopy

2418 The calibration was done using a $^{148}\text{Gd}^{239}\text{Pu}^{241}\text{Am}^{244}\text{Cm}$ source which emits α parti-
2419 cles with four different energies. The PSA in combination with the current amplifier
2420 was compared against the 8-bit spectroscopic application in combination with the
2421 charge amplifier and a commercial 14-bit spectroscopic readout.

2422 The ^{241}Am peak measured by the Cx amplifier has an RMS of 0.8 ADC, which
2423 corresponds to a 32 keV energy resolution. For comparison, the C2 amplifier measures
2424 this peak with an RMS of 1.9 ADC, which corresponds to a 75 keV energy resolution.
2425 Therefore the energy spectrum measured by the current amplifier has a lower energy
2426 resolution.

2427 5.9 Source calibration

2428 The operation of the pulse shape analysis was tested using several radioactive sources.
2429 In particular, an α , a β , a γ and a n source were used. Each source was placed on
2430 top of the diamond detector and left for a predefined time depending on its activity.
2431 Table 1.2 shows the sources used, the time of exposure and their rate during this
2432 time. The data for the α source were taken for both polarities. In addition, a long
2433 run with an α source with a sheet of paper in between the source and the diamond
2434 was taken. The paper stopped the α particles but let through the photons, which
2435 helped to estimate the background photon radiation of the source.

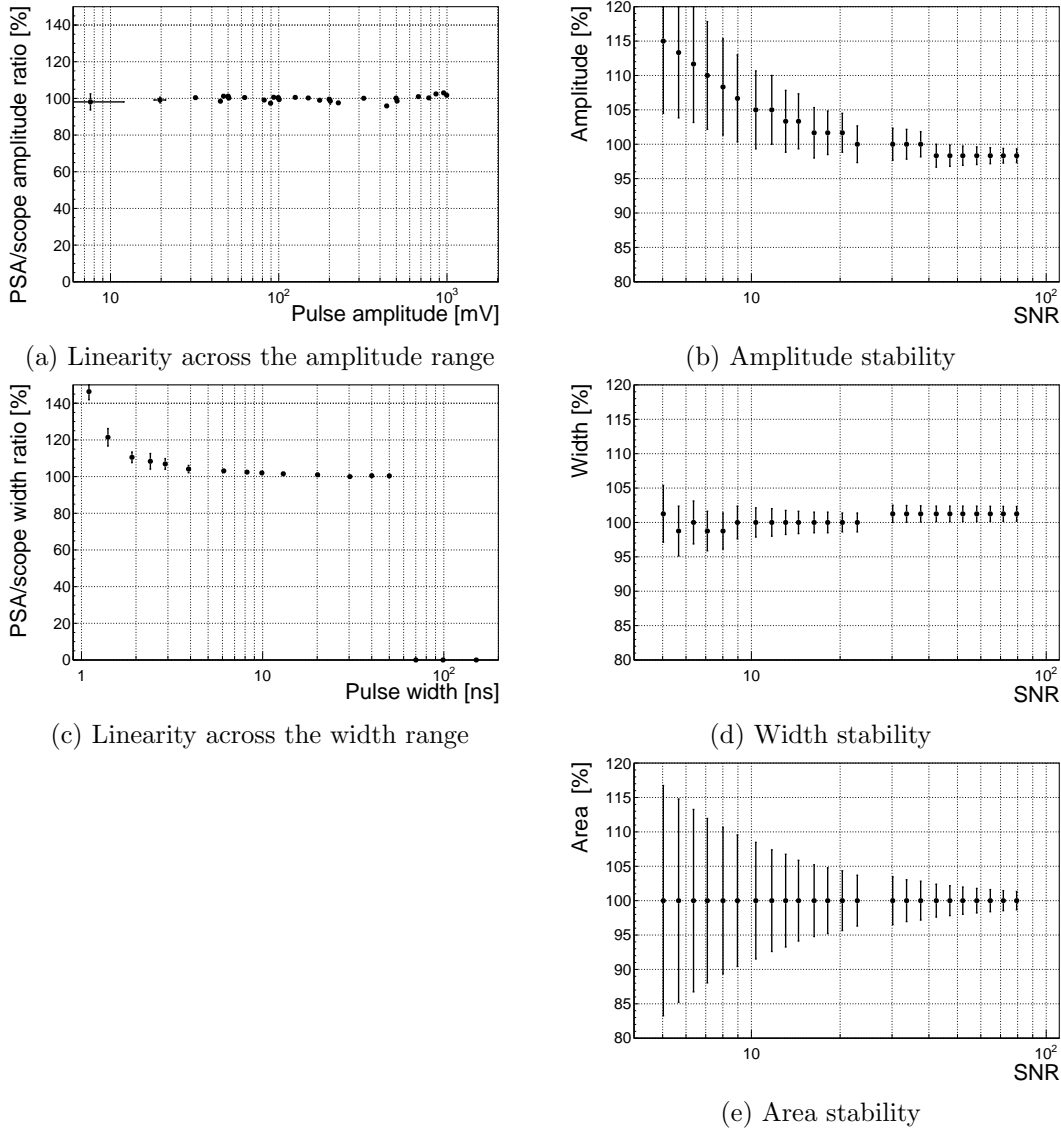


Figure 5.10: These diagrams show the linearity of the measurements and their stability with respect to analog noise.

	Run	Source	Radiation	Energy [MeV]	Time [h]	Triggers	Rate [s^{-1}]	Bias [V]
2436	1	$^{241}\text{Am}^*$	α	5.5	60	958	4.4e-3	500
	2	^{241}Am	α	5.5	17	10558	0.17	500
	3	^{241}Am	α	5.5	18	11454	0.18	-500
	4	^{90}Sr	β	2.3	0.42	1.07e6	1000	500
	5	^{60}Co	γ	1.3	0.28	1.34e6	3300	500
	6	$^{239}\text{Pu Be}$	n	1–10	2.5	1.5e6	230	500

2437

Table 5.2: Measurements carried out at Atominstitut

2438

The pulses acquired during the data taking are shown in persistence plots in figures 1.12. Figure 1.12a showing the ^{241}Am source background reveals that the 2439 diamond detector had been contaminated. This stems from the fact that α pulses 2440

5.9. SOURCE CALIBRATION

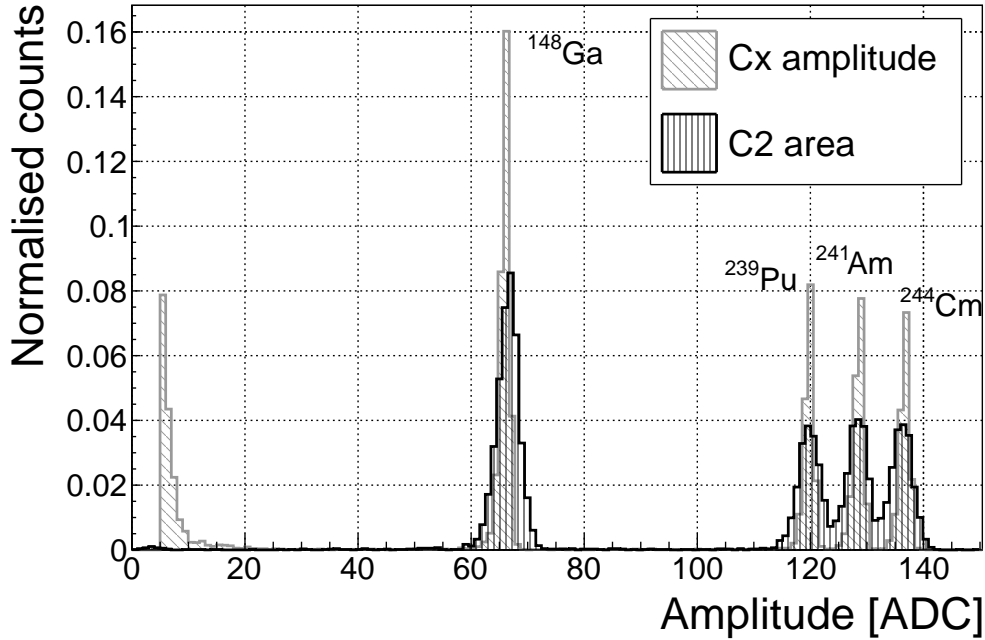


Figure 5.11: Spectrum of a $^{148}\text{Gd}^{239}\text{Pu}^{241}\text{Am}^{244}\text{Cm}$ source using a Cx and a C2 amplifier

are recorded despite having a sheet of paper, which stops all the particles emitted by the source. However, the number of α hits due to contamination is negligible - an estimated 1 h^{-1} . Another point worth noting is the falling slope of the rectangular pulse in figure 1.12c. This stems from the space charge that had built up during the neutron irradiation and is discussed in section 1.9.3. Finally, figure 1.12f shows that the neutron source causes the widest variety of pulse shapes - triangular and rectangular as well as those in between. Pulse shapes caused by neutrons are described in detail in [44, 43].

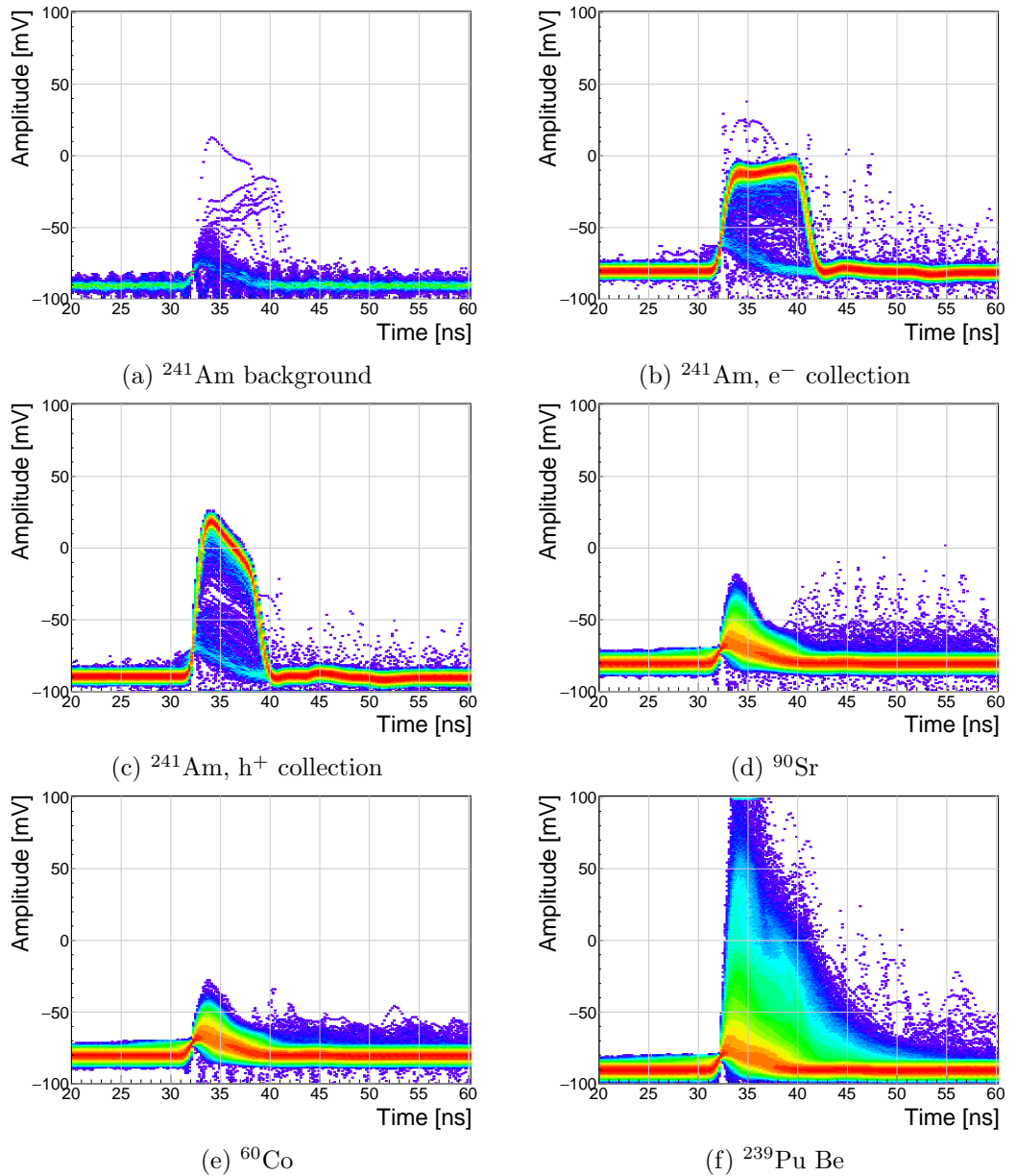


Figure 5.12: Accumulated pulses for all runs

5.9. SOURCE CALIBRATION

2449 5.9.1 Source measurements - scatter plots

2450 An online pulse shape analysis has been run on all the above mentioned data sets.
2451 The parameters of the pulses are plotted in 2D histograms - in form of scatter plots.
2452 The aim is to find a way to distinguish between the various types of radiation in
2453 order to only select the spectrum of a single type of particles from a spectrum of a
2454 mixed source. The energy spectrum is directly proportional to the measured area of
2455 the current pulses, therefore all the parameters were plotted against the pulse area.
2456 The parameters used are:

- 2457 ● FWHM
- 2458 ● Base width
- 2459 ● Amplitude
- 2460 ● Amplitude × Base width
- 2461 ● Base width - FWHM
- 2462 ● Slope

2463 The sets of plots in figures 1.13, 1.14, 1.15, 1.16 and 1.17 show the above listed
2464 parameters plotted against the pulse area for ^{241}Am background, electrons and holes,
2465 ^{90}Sr and ^{64}Co source, respectively. Any distinguishable difference between the plots
2466 of two sources would suggest that that particular parameter can be used to distinguish
2467 one type radiation from the other. In these figures the photons are considered the
2468 rejected pulses (greyscale colour palette) whereas α particles or neutrons are accepted
2469 (yellow colour palette).

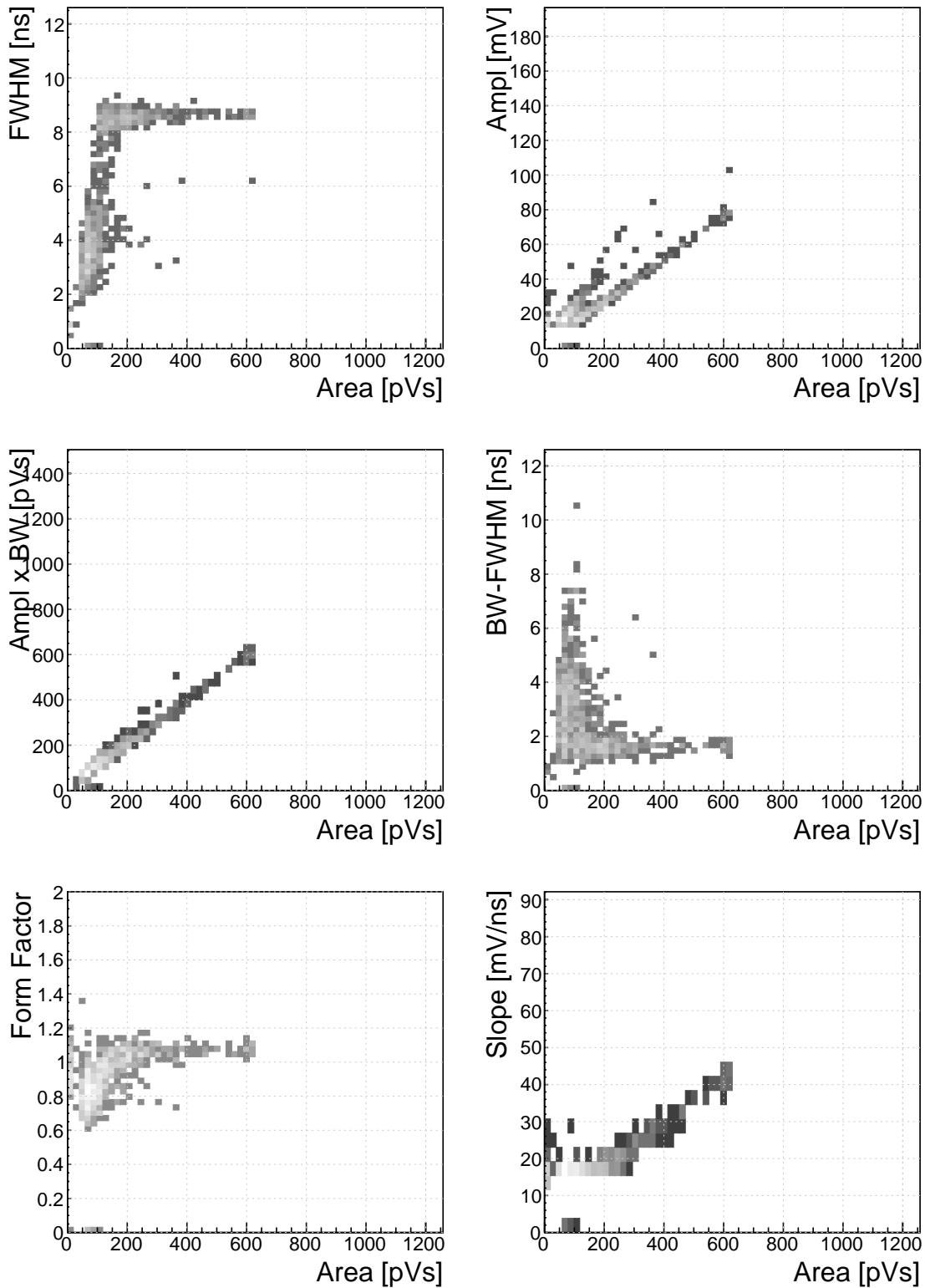


Figure 5.13: Background measurements

5.9. SOURCE CALIBRATION

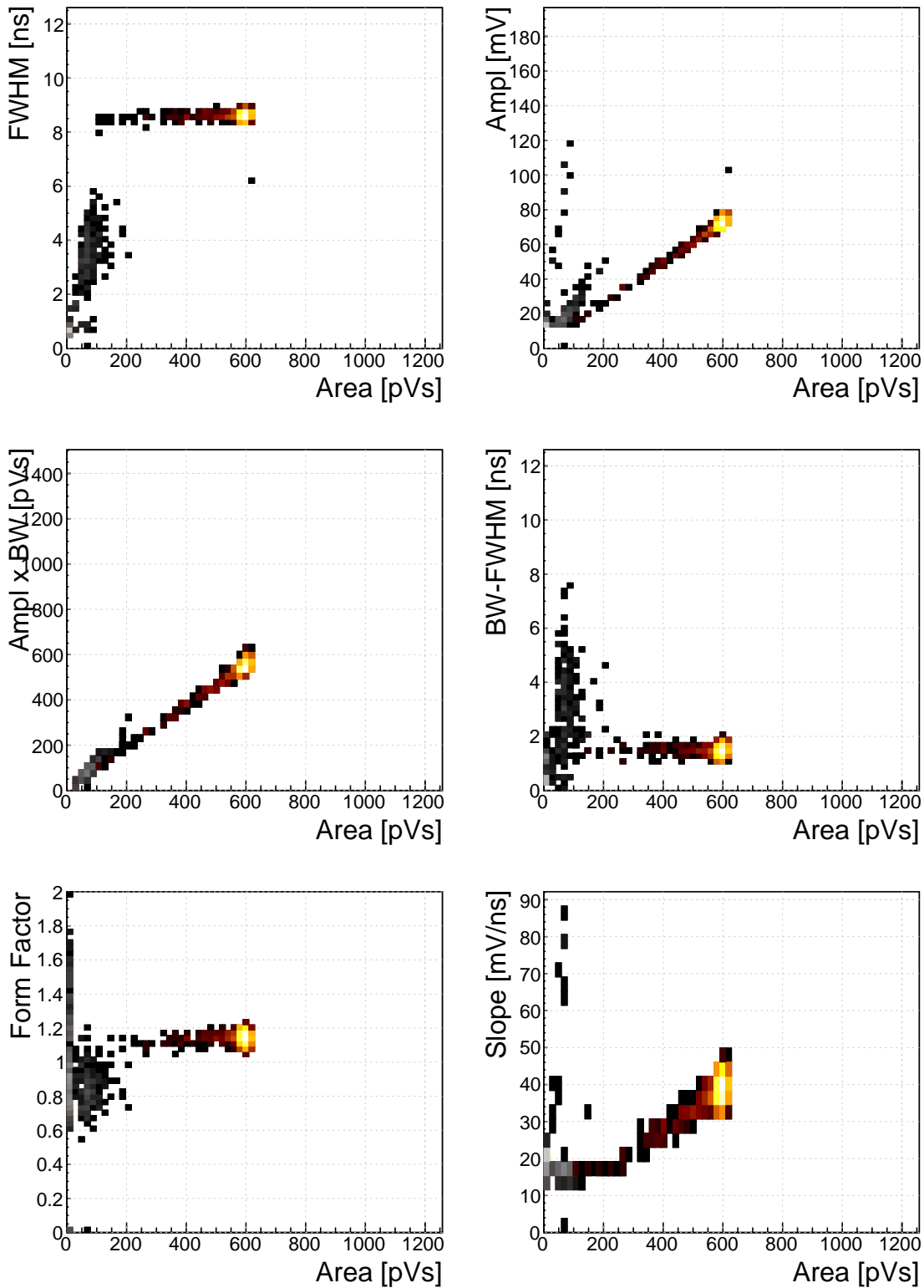


Figure 5.14: ^{241}Am , e^- collection. Qualifier: FWHM 7–10 ns.

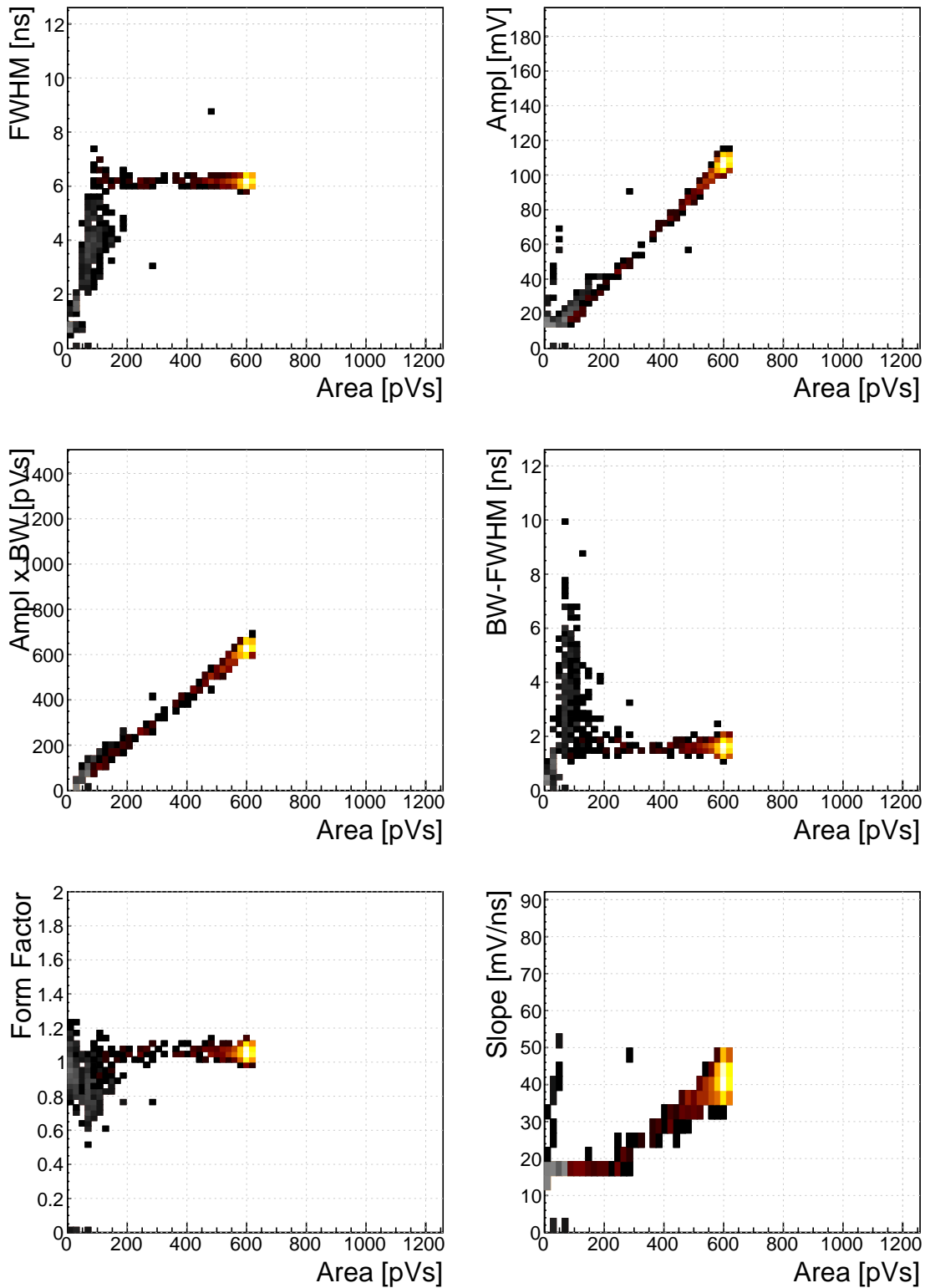


Figure 5.15: ^{241}Am , h^+ collection. Qualifier: FWHM 5.5–8 ns.

5.9. SOURCE CALIBRATION

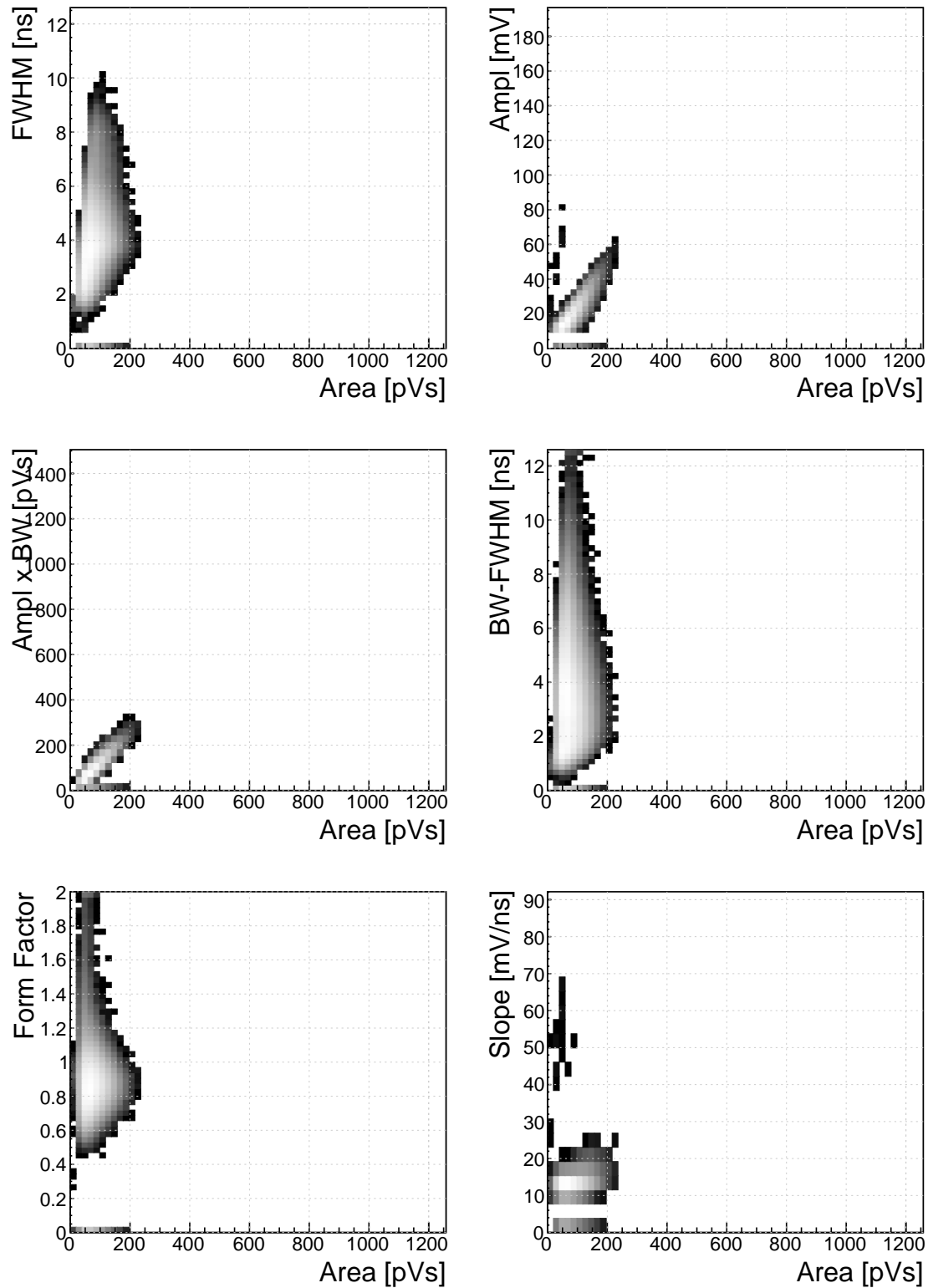


Figure 5.16: ^{90}Sr

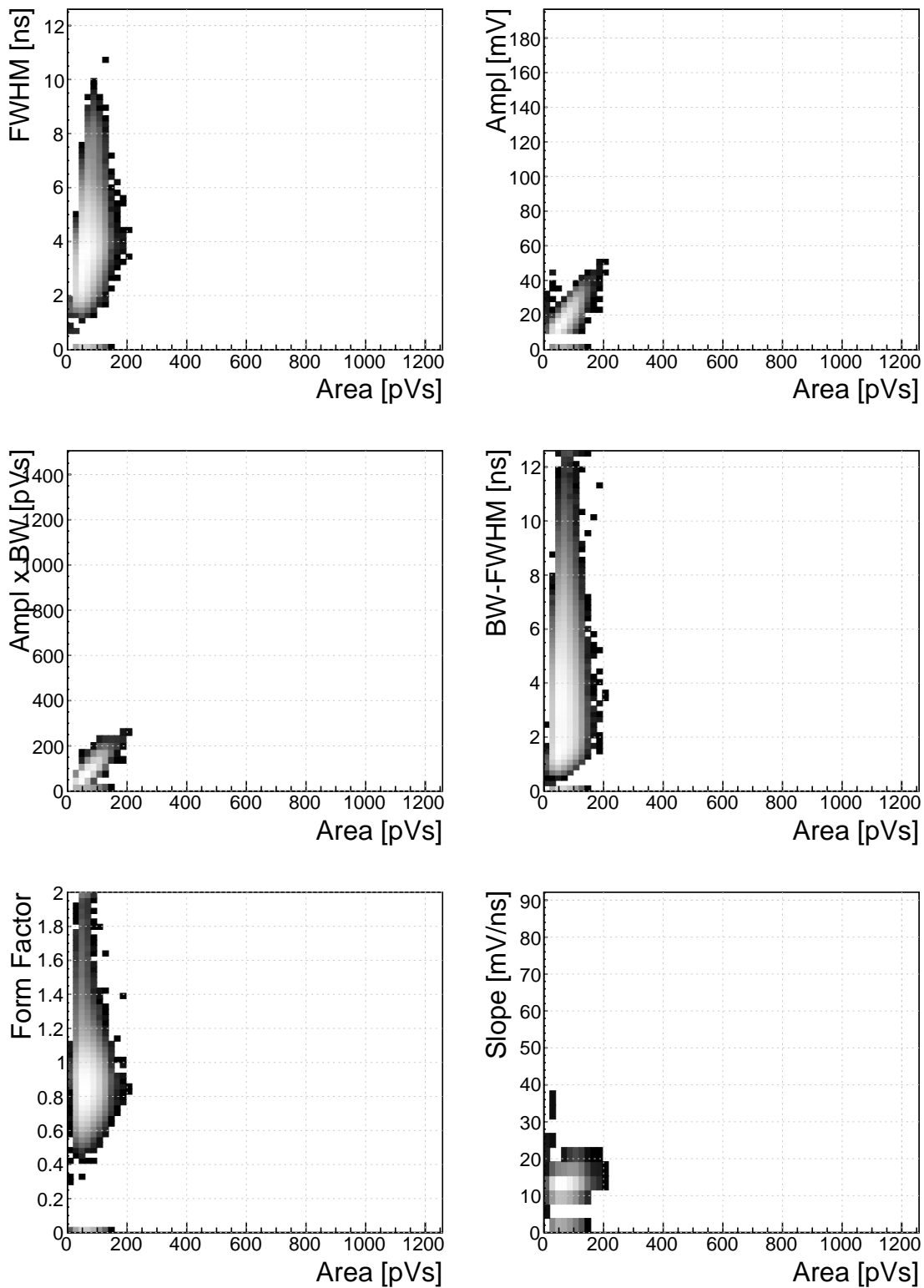


Figure 5.17: ^{60}Co

5.9. SOURCE CALIBRATION

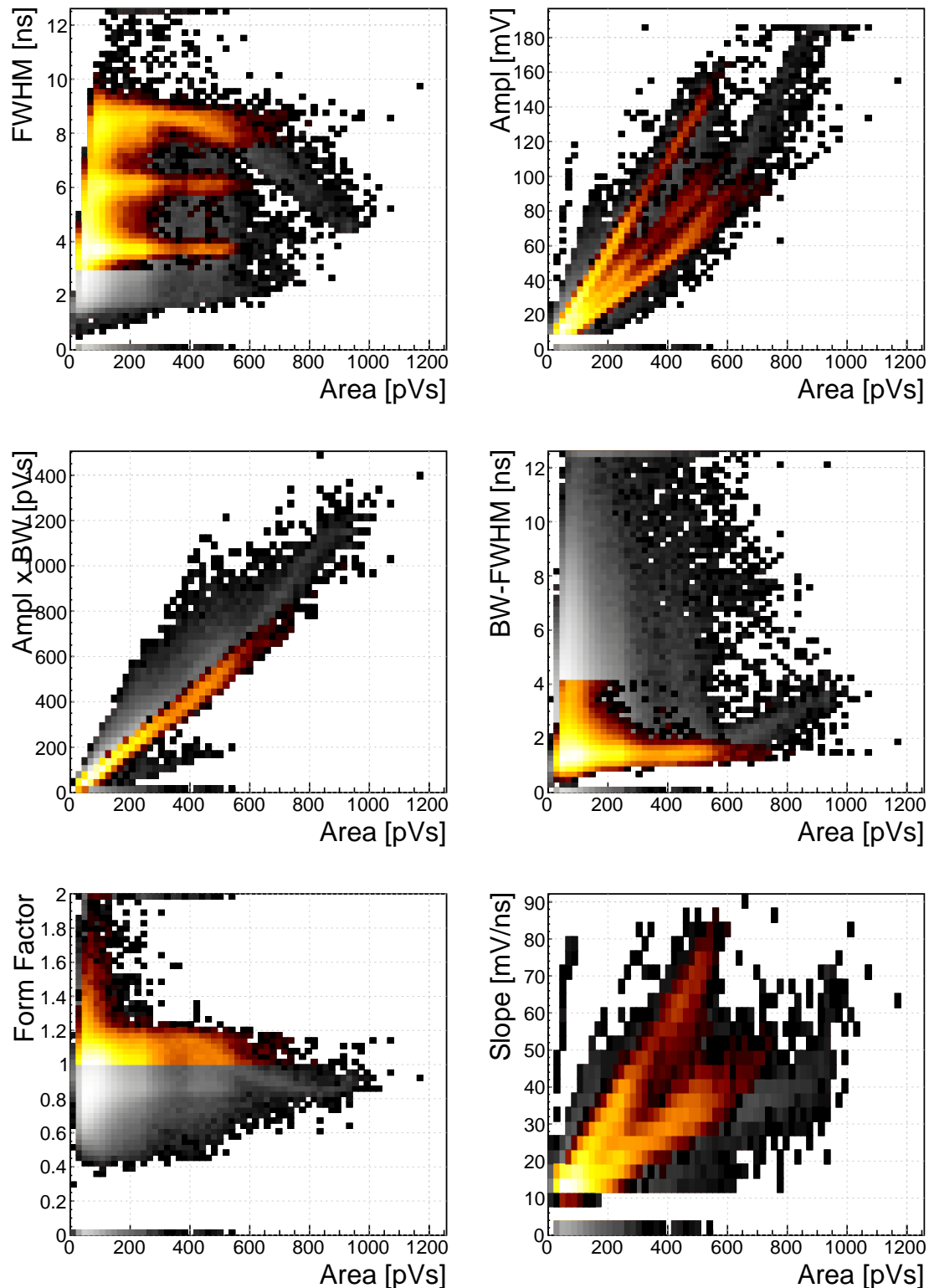


Figure 5.18: ^{239}Pu Be. Qualifiers: BW-FWHM 0.2–4 ns, FWHM 3–12 ns, Form factor 1.45

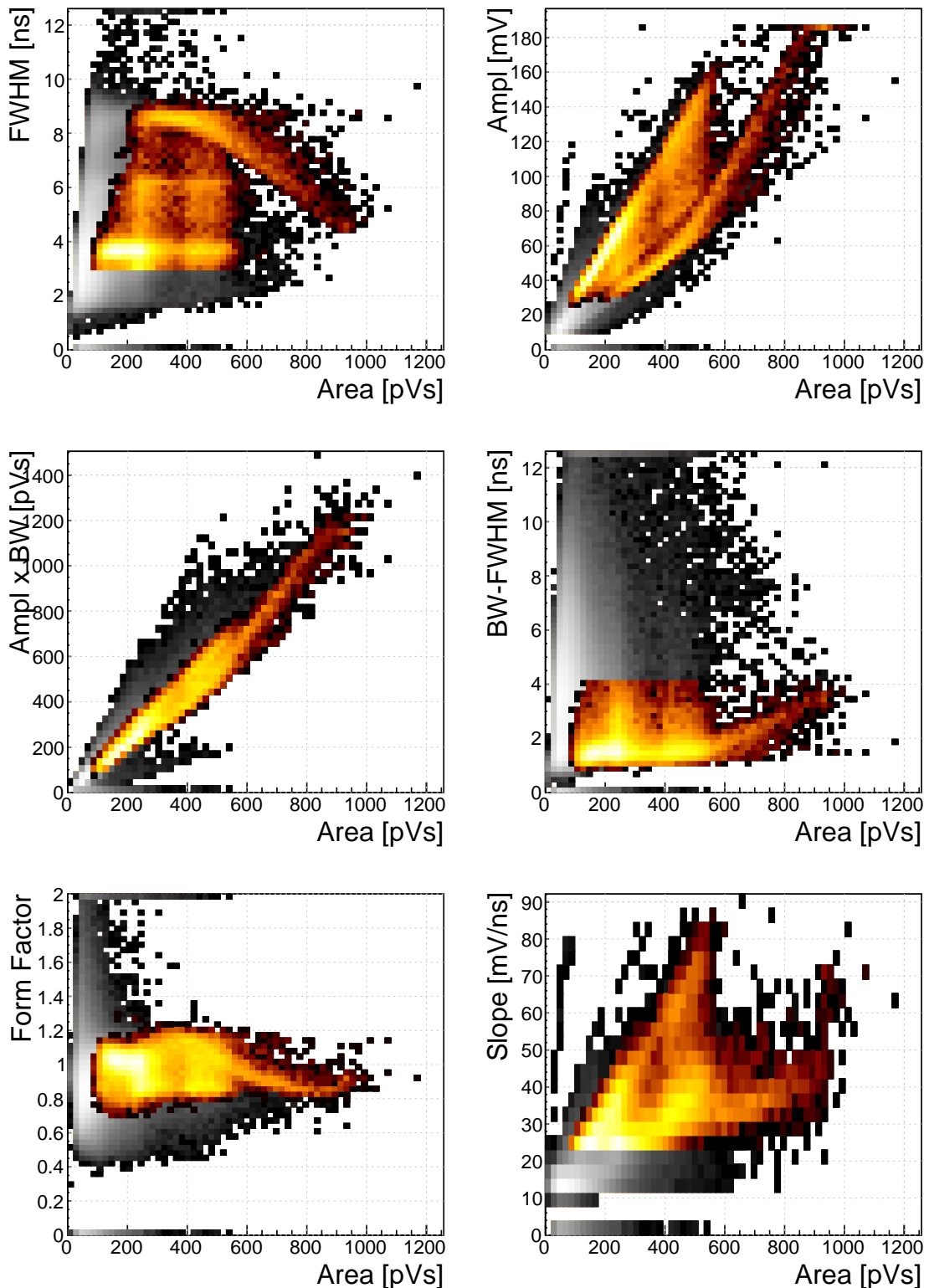


Figure 5.19: ^{239}Pu Be. Qualifiers: BW-FWHM 0.2–4 ns, FWHM 3–12 ns, Slope 25–104 mV/ns

5.9. SOURCE CALIBRATION

2470 5.9.2 Discussion

2471 The ^{241}Am background measurement (see figure 1.13) revealed that the diamond de-
2472 tector has been contaminated, probably with chipped-off grains of the source. These
2473 emit α particles, which are detected by the diamond detector. The resulting plots are
2474 almost identical to those taken during the ^{241}Am run (figure 1.14), with a difference
2475 that there are much fewer α entries in the former. Due to the losses in the air they
2476 vary in energy – from ~ 5 MeV down to 1 MeV. Therefore in the top left plot a dis-
2477 tinctive horizontal stripe appears at a width of 9 ns, ranging from 100 up to 630 pVs.
2478 The shape of the pulse at smaller energies retains the width, only its amplitude is
2479 decreased. The other cluster in the FWHM–area phase space comes from the back-
2480 ground photons. The two clusters are far apart from one another with no overlap. It
2481 is therefore straightforward to define a cut in the FWHM to distinguish between the α
2482 and γ entries. The situation is similar when inverting the bias voltage and collecting
2483 holes (see figure 1.15), but here the two clusters are much closer together, making it
2484 more difficult to define a clear border between the two. The other five qualifiers are
2485 in this case less important than the FWHM. Nevertheless, it can be deduced from the
2486 plots that the difference BW-FWHM must be below 4 ns and that the Form Factor
2487 (bottom left plots) has to be set to 1.45 to push the α entries over 1, which is the
2488 threshold for accepting entries. The slope is dependent of the amplitude, which can
2489 be seen in the bottom right plot, making it an unreliable qualifier in the lower area
2490 range. The amplitude, scaling with area, makes a distinguishable straight line in the
2491 bottom right plot. For the electron collection this line has a different slope coefficient
2492 than the photon related line. For the holes, however, these two lines are overlapping,
2493 rendering it impossible to use this as a means of identifying the α from a γ entry.

2494 The phase space of the ^{90}Sr source overlaps entirely with that of the ^{60}Co source
2495 (see figures 1.16 and 1.17). This renders it virtually impossible to distinguish between
2496 photons and electrons (MIPs). Comparing the FWHM phase space of the photons
2497 and alphas and the high reach of the former, the electron collection of the alphas
2498 would need to be used to distinguish between the two types of particles.

2499 The neutron source emits a mixed field of neutrons and photons. The neutrons are
2500 rarely detected – the interactions happen mostly in the electrodes on either side of the
2501 detector. The α particles created by the interactions are detected by the diamond.
2502 Depending on the side of the interaction, the created pulse is either due to hole- or
2503 electron collection. They make the two distinct lines in the FWHM phase space (see
2504 figure 1.18, top left plot) at 9 ns and 6 ns. The third line at 4 ns is created when
2505 a neutron interacts in the ballistic centre [?] of the diamond – the position where it
2506 takes the holes and the electrons the same time to drift to the opposite electrodes.
2507 The entries in between are created by neutron interactions at random positions in the
2508 diamond, which produce pulses of various shapes. By making use of the Form Factor
2509 set to 1.45, the three-line structure becomes more pronounced. However, a part of the
2510 cluster belonging to the 9 ns line is omitted. This part with the area ranging between
2511 600 and 1000 pVs starts decreasing in FWHM due to an unexplained phenomenon,
2512 probably detector related. Consequently its Form Factor falls below the threshold

of 1, rejecting these entries as background. In an alternative case (see figure 1.19), a Slope qualifier is used instead. By cutting the pulses whose falling slope is not steep enough, there is a big chance that neutrons with a low energy deposition (small amplitudes) are cut away as well. Nevertheless, the entries with the large area, which definitely pertain to the neutron interactions, are accepted in this case. The three distinct lines in the FWHM phase space are still visible.

5.9.3 Space charge build-up

Space charge built up during the neutron irradiation ($\sim 10^{10}$ n), which reflected on the pulse shapes. Instead of a flat top, they developed a slope. This was of opposite signs for the two polarities, as can be seen in figures 1.20a and 1.20b. The figures contain a set of 64 superimposed pulses taken at ± 500 V bias. The shape persisted until the space charge was neutralised by means of a β source irradiation at a 0 V bias. Figure 1.21 shows the decreasing of the slope coefficient as a function of received β dose.

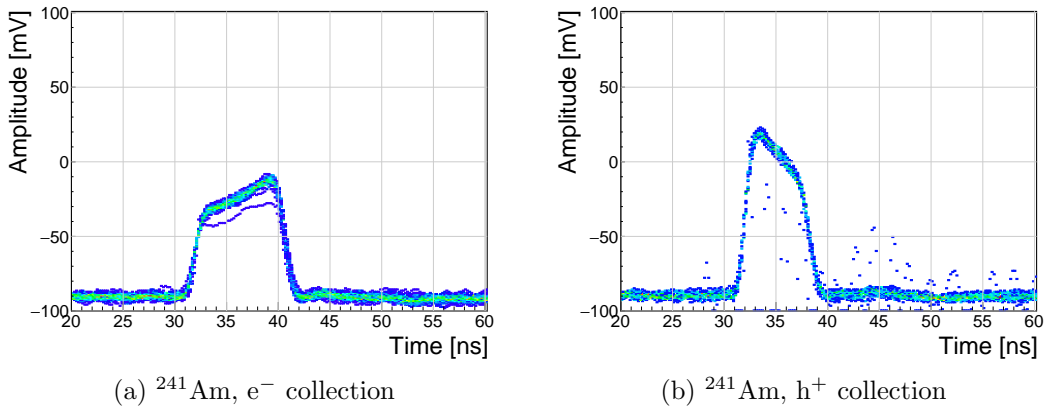


Figure 5.20: Built up space charge causes a slope which has the opposite slope for electrons and holes

5.9. SOURCE CALIBRATION

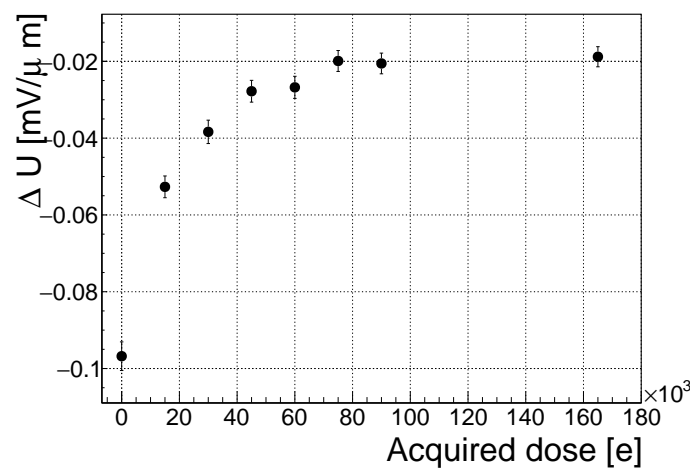


Figure 5.21: Using β radiation to reduce space charge in diamond

5.10 Applications in neutron instrumentation

The real-time pulse shape analysis procedure can be applied to more complex systems.
This section includes three applications where the PSA has been applied.

Semiconductor-based neutron detectors provide a compact technology for neutron detection. However, the cross section of a neutron with the diamond bulk is very low, since it only interacts with the core of the atom. Diamond is mainly used to detect charged particles and photons.

Research neutron reactors radiate a mix of particles, apart from neutrons also photons. The photons are considered a background radiation, concealing the neutron spectrum. When measured with diamond, the signal from neutrons is difficult to distinguish from the photon spectrum. In addition, low energy neutrons do not cause nuclear reactions in the bulk. All in all, the neutron measurements in a reactor present a challenge with diamond. However, by means of the PSA, the neutron signal can be discriminated from the photon background to some extent. The following two cases show how measurements of fast (n^+) and thermal (n^-) neutrons have been carried out by making use of the PSA.

Note the changing scale on the X axis in the figures.

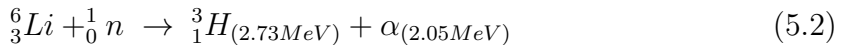
5.10.1 Thermal neutron flux monitoring

Research neutron reactors like TRIGA MARK II [?] at Atominstitut [?] in Vienna are capable of emitting neutrons at a wide range of energies. The neutron flux is proportional to the current power of the reactor. It is therefore instrumental to monitor the neutron flux to make sure that the reactor operation is within the specified limits. However, the byproduct of the radioactive decays in the core is γ radiation, which has an energy range that overlaps with that of neutrons, making it difficult to measure the neutron flux. This is where PSA and diamond detectors come into play. This section describes the application of thermal neutron flux monitoring by means of the PSA.

Thermal neutrons do not interact with the diamond bulk due to their low kinetic energy (of the order of 0.012 eV). Hence a converter foil has to be added to produce second order effects. Incoming neutrons interact with the foil, producing a set of secondary particles. These can then be detected upon hitting the detector bulk. Common neutron interactions that are used in thermal neutron detection are $^{10}\text{B}(n,\alpha)^7\text{Li}$ reaction and $^6\text{Li}(n,\alpha)^3\text{H}$ reaction (α stands for ^4_2He , see equation 1.2). The focus in this section is on the latter. With a foil installed, there are several possibilities for neutrons to interact with the detector system. Each of these interactions ionises the diamond bulk in its own way, resulting in a specific shape of the current pulse. A neutron can: 1) interact with the foil, producing an α and a ^3H , 2) interact with a carbon atom in the lattice, producing an α and a γ or even three α . The thermal neutrons do not have enough kinetic energy to interact with the lattice,

5.10. APPLICATIONS IN NEUTRON INSTRUMENTATION

2566 therefore the focus will be on case (1), the equation for this reaction is the following:



2567 The particles in the first case are produced outside the diamond and get stopped
2568 immediately upon hitting the sensor. The resulting pulses for both particles have a
2569 rectangular shape of the same width, because the carriers drift with the same speed
2570 in both cases. The difference is in the number of free carriers produced - the tritium
2571 creates more (proportional to the deposited energy), which in turn induces a higher
2572 pulse.

2573 TRIGA MARK II neutron reactor emits large amounts of γ radiation in the
2574 energy range up to 3 MeV. This already affects the measurements of α particles, the
2575 energy of which peaks at 2.05 MeV in the case of 6Li converter foil. However, γ
2576 background radiation can be suppressed by discriminating current pulses of photons
2577 from those induced by α particles. This idea has already been implemented in offline
2578 analysis in [29, 24]. The results show that the background photons can be subtracted
2579 successfully. In order to make sure that every single incident thermal neutron has
2580 been accounted for, the algorithm has been ported to FPGA where it detects and
2581 analyses particles in real time.

2582 5.10.1.1 Measurements

2583 ROSY readout device with the implemented Pulse Shape Analysis was put to a test
2584 at Atominstut in Vienna. Their TRIGA2 neutron reactor is capable of delivering
2585 thermal neutrons with the energy 0.012 eV at a rate of $10^3 n \text{ cm}^{-2} s^{-1}$, with a
2586 considerable γ background.

2587 First, the device was calibrated using an unsealed monochromatic ${}^{241}Am$ source
2588 with the emitted particle energy $E_\alpha = 5.12MeV$ (taking into account the losses in
2589 the air). Then the diamond detector was exposed to the beam. Secondary reaction
2590 products (α and 3H particles), created by neutrons hitting the converter foil, were
2591 detected by the diamond sensor, together with a significant photon background. Then
2592 the pulse identification algorithm was applied to discriminate between the reaction
2593 products and the photons.

2594 The main parts of the detector are an sCVD diamond sensor sized $4.7 \times 4.7 \text{ cm}^2$
2595 and a $1.8 \mu\text{m}$ thick LiF converter foil, both embedded in an RF-tight PCB. The
2596 diamond sensor is biased with a bias voltage of $1 \text{ V}/\mu\text{m}$ and capacitively coupled to
2597 CIVIDEC's C2 40 dB wide bandwidth current preamplifier. A 5 m long BNC cable
2598 connects the preamplifier to CIVIDEC ROSY box. The detector assembly together
2599 with the preamplifier has to be placed in front of an exit hole of the reactor.

2600 Note: this data set has been taken with an older version of the firmware, which
2601 only measured a limited number of pulse parameters.

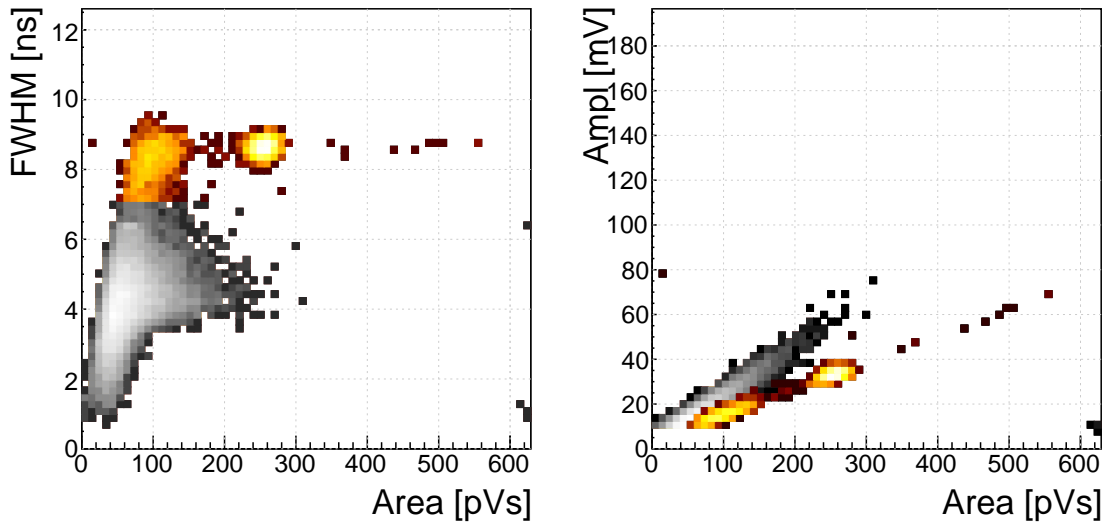


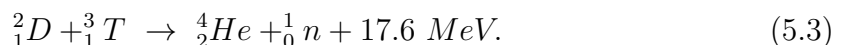
Figure 5.22: Thermal neutrons, photons. Qualifier: FWHM 7–12 ns

2602 5.10.1.2 Results

2603 The data collected by the PSA show a high flux of photons, which covers a wide area
2604 range. The ^3He peak is clearly visible and has almost no overlap with the photon
2605 cluster. The α cluster has a much lower energy and is in the same energy range as
2606 the photons. However, if a FWHM parameter is observed, a distinction between the
2607 photons and the α can be seen. By setting a qualifier to the right value, the photon
2608 background is cut away, leaving only the thermal neutron decay products in the data
2609 set (see figure 1.22).

2610 5.10.2 Fusion power monitoring

2611 Many research collaborations around the world are trying to develop a functional
2612 fusion reactor, which could provide a cleaner energy source. One of them is ITER [8],
2613 a research fusion reactor being built in France. The idea behind it is to harvest
2614 energy from the fusion of light atoms into a heavier one. For ITER the fuel chosen
2615 is a mixture of deuterium and tritium, which fuse into a helium atom at extremely
2616 high temperatures (plasma), emitting a highly energetic neutron as a byproduct. The
2617 equation is the following:



2618 The α particle immediately deposits its energy within the plasma. The neutron, due
2619 to its neutral charge, continues its way out of the system where it is stopped. The
2620 stopping power is converted into energy, which heats the water into steam, which in
2621 turn spins the turbines, generating electricity.

2622 It is possible to monitor the activity of the reactor by measuring the flux of neu-
2623 trons emitted. Neutron diagnostics such as neutron cameras, neutron spectrometers

and neutron flux monitors therefore provide robust measurements of fusion power. A high γ background makes it difficult to accurately measure the neutron flux. This is a motivation to use a diamond based detector with a real-time PSA algorithm.

The neutrons emitted are 14 MeV mono-energetic fast neutrons. The most accurate and efficient way to detect them with a diamond detector is by means of a $C_{12}(n,\alpha)$ reaction with a carbon atom in the ballistic centre [30]. In this region the positive and negative charge carriers created by α that start drifting in the opposite directions need the same time to reach the opposite electrodes.

5.10.3 Fast neutron monitoring

The CROCUS reactor at EPFL [3] is a research neutron reactor. The research group working on the reactor is interested in measuring neutrons with energies between 1–2 MeV, which is overlapping with the γ background energy range.

The highest output power of the CROCUS reactor is 100 W. Currently there are fission chambers that carry out the neutron counting, which is a measure of the activity of the reactor. The new goal is to measure both neutrons and photons, but separately. The pulse shape analysis is a good solution for this task. For this, a 400 μm thick diamond detector with a specially designed casing was added to measure the activity. The LiF foil was added for conversion of thermal neutrons. The ROSY box with the integrated PSA routine was used for signal analysis.

The results from a test run at 10 W output power are shown in figure 1.23. The data include a mixed field consisting of fast neutrons, photons and of α and 3He particles as products of thermal neutron decay (due to a LiF foil in front of the detector). The data after the applied cuts again show a distinct 3He cluster, as well as the three-lane neutron signature. The α signal is buried under the signals stemming from fast neutrons and photons.

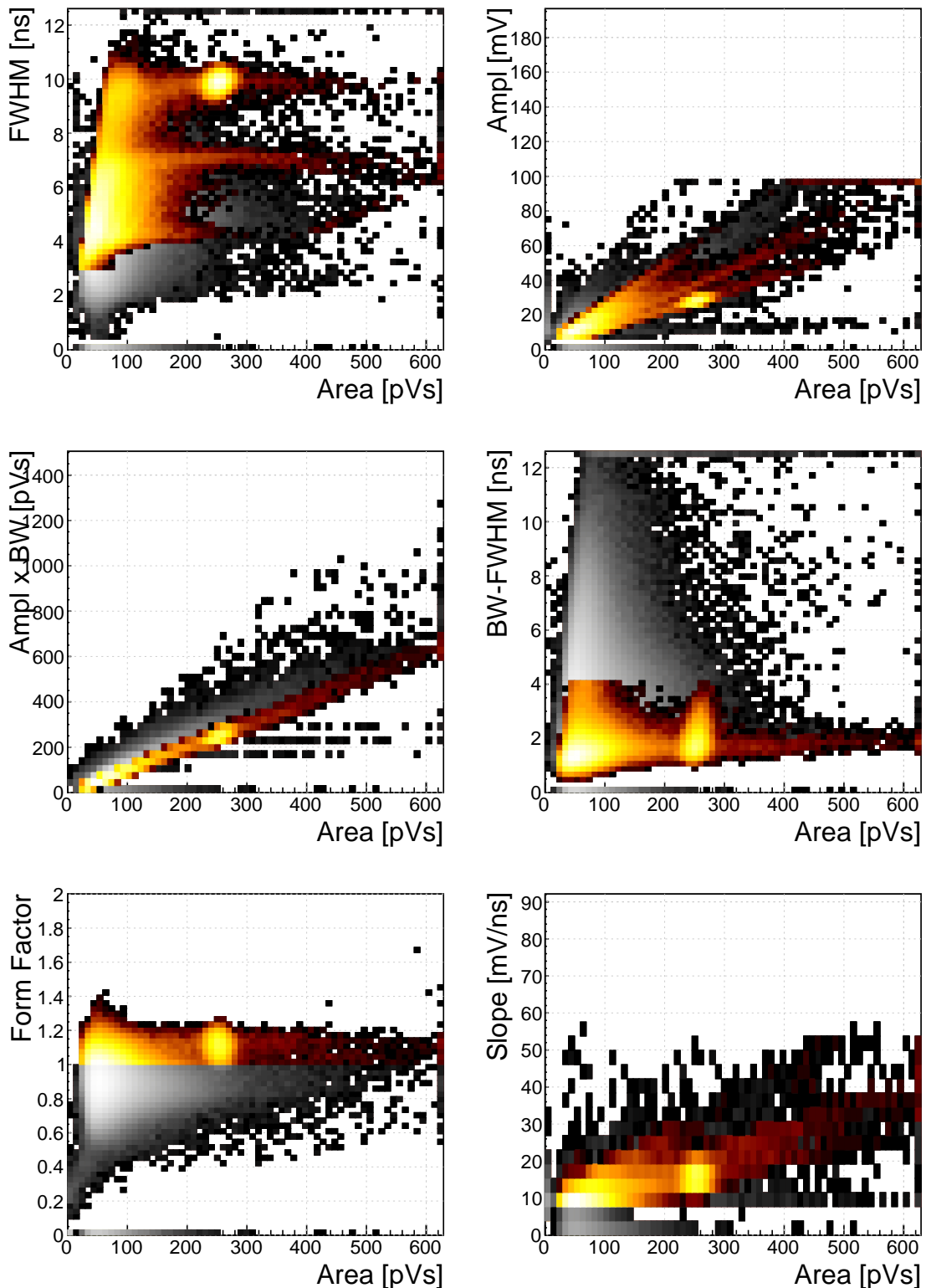


Figure 5.23: Fast neutrons, thermal neutrons, photons. Qualifiers: BW-FWHM 0–4 ns, FWHM 3–12 ns, Form factor 1.45, Slope 10–108 mV/ns

2649 **5.11 Conclusion**

2650 This chapter describes a system that can identify the type of radiation in real time.
2651 The system is implemented on an FPGA in a CIVIDEC ROSY box and is used with
2652 diamond detectors. The signal from the diamond sensor is read in and analysed in the
2653 firmware. First the shape of the pulse is parametrised. Then the logic determines the
2654 type of particle according to the user defined cuts. Finally the parameters are written
2655 into a histogram, which is read out by the user. The firmware is designed to carry
2656 out the pulse shape analysis of a single pulse in ~ 200 ns, yielding a maximum pulse
2657 rate of 5×10^6 particles per second. The rate as well as the linearity the measurement
2658 stability with respect to noise have been verified using a pulse generator. Then
2659 several radioactive sources were used to calibrate the device. Finally the system was
2660 installed in two neutron reactors to test the operation in a mixed field containing
2661 thermal neutrons, fast neutrons and photons. Various cuts were tested to optimise
2662 the identification.

²⁶⁶³ Bibliography

- ²⁶⁶⁴ [1] *ASIC*.
- ²⁶⁶⁵ [2] *Atominstitut, Technical University of Vienna, Austria*.
- ²⁶⁶⁶ [3] *CROCUS neutron reactor*. <http://lrs.epfl.ch/page-55655-en.html>.
- ²⁶⁶⁷ [4] *DRS4*. <https://www.psi.ch/drs/evaluation-board>.
- ²⁶⁶⁸ [5] *Element Six*. <http://www.e6.com>.
- ²⁶⁶⁹ [6] *European Centre for Nuclear Research, CERN*.
- ²⁶⁷⁰ [7] *I2a Technologies Pte. Ltd.* <https://www.2atechnologies.com>.
- ²⁶⁷¹ [8] *ITER fusion reactor*. <https://www.iter.org/>.
- ²⁶⁷² [9] *Neutron Time-of-flight experiment*.
- ²⁶⁷³ [10] *Paul Scherrer Institute*. <https://www.psi.ch/>.
- ²⁶⁷⁴ [11] *RD42 collaboration*. <http://rd42.web.cern.ch/rd42/>.
- ²⁶⁷⁵ [12] *TRIGA MARK II neutron reactor*.
- ²⁶⁷⁶ [13] *Xilinx Virtex 5 FPGA*.
- ²⁶⁷⁷ [14] *Determination of operational dose equivalent quantities for neutrons*. ICRU,
²⁶⁷⁸ Washington, DC, 2001.
- ²⁶⁷⁹ [15] General Atomics. *View of the TRIGA reactor*. 2015.
- ²⁶⁸⁰ [16] H. Bethe and J. Ashkin. *Experimental Nuclear Physics*, ed. E. Segre, page 253,
²⁶⁸¹ 1953.
- ²⁶⁸² [17] W. Blum, W. Riegler, and L. Rolandi. Particle Detection with Drift Chambers,
²⁶⁸³ volume 2 of 2. Springer-Verlag, Berlin Heidelberg, 2008.
- ²⁶⁸⁴ [18] Giorgio Brianti. SPS North Experimental Area. Technical Report CERN-SPSC-
²⁶⁸⁵ T-73-8. LabII-EA-Note-73-4, CERN, Geneva, 1973.
- ²⁶⁸⁶ [19] Maximilien Brice. *View of the nTOF detector*. Oct 2010.

BIBLIOGRAPHY

- 2687 [20] Maximilien Brice. *LHC tunnel*. Jan 2011.
- 2688 [21] P. Carazzetti and H. R. Shea. *Electrical breakdown at low pressure for planar*
2689 *microelectromechanical systems with 10- to 500 μm gaps*. *J. Micro/Nanolith.*
2690 *MEMS MOEMS*, (8(3), 031305), Jul-Sep 2009.
- 2691 [22] Daniel Dominguez. *Standard Model. Le modele standard*. General Photo, Mar
2692 2015.
- 2693 [23] CIVIDEC Instrumentation GmbH. *sCVD diamond sensor*. 2015.
- 2694 [24] E. Griesmayer, R. Bergmann, H. Böck, M. Cagnazzo, P. Kavrigin, B. Mor-
2695 genbesser, and M. Villa. *A Novel Neutron Flux Monitor Based On Diamond*
2696 *Detectors at the Vienna TRIGA Mark II Reactor. submitted to the proceedings*
2697 *of ICRR 2015*, 2015.
- 2698 [25] E. Griesmayer and B. Dehning. Diamonds for beam instrumentation. *Physics*
2699 *Procedia*, 37:1997 – 2004, 2012. Proceedings of the 2nd International Conference
2700 on Technology and Instrumentation in Particle Physics (TIPP 2011).
- 2701 [26] Moritz Guthoff, Wim de Boer, and Steffen Mller. Simulation of beam induced
2702 lattice defects of diamond detectors using {FLUKA}. *Nuclear Instruments and*
2703 *Methods in Physics Research Section A: Accelerators, Spectrometers, Detectors*
2704 *and Associated Equipment*, 735:223 – 228, 2014.
- 2705 [27] M. Huhtinen. Simulation of non-ionising energy loss and defect formation in
2706 silicon. *Nuclear Instruments and Methods in Physics Research A*, 491:194–215,
2707 September 2002.
- 2708 [28] Hendrik Jansen, Norbert Wermes, and Heinz Pernegger. *Chemical Vapour De-*
2709 *position Diamond - Charge Carrier Movement at Low Temperatures and Use in*
2710 *Time-Critical Applications*. PhD thesis, Bonn U., Sep 2013. Presented 10 Dec
2711 2013.
- 2712 [29] P. Kavrigin, P. Finocchiaro, E. Griesmayer, E. Jericha, A. Pappalardo, and
2713 C. Weiss. *Pulse-shape analysis for gamma background rejection in thermal neu-*
2714 *tron radiation using CVD diamond detectors*. *Nuclear Instruments and Methods*
2715 *in Physics Research A*, (795), 2015.
- 2716 [30] P. Kavrigin, E. Griesmayer, F. Belloni, A.J.M. Plomp, P. Schillebeeckx, and
2717 C. Weiss. *$^{13}C(n,\alpha_0)^{10}Be$ cross section measurement with sCVD diamond detec-*
2718 *tor*. *submitted to EPJA*, 2016.
- 2719 [31] Claude A. Klein. Radiation-induced energy levels in silicon. *Journal of Applied*
2720 *Physics*, 30(8):1222–1231, 1959.

BIBLIOGRAPHY

- [32] Gregor Kramberger, V. Cindro, A. Gorisek, I. Mandic, M. Mikuz, and M. Zavrtanik. Effects of bias voltage during priming on operation of diamond detectors. *PoS*, Vertex2012:013, 2013.
- [33] W. Y. Liang. Excitons. *Physics Education*, 5:226–228, July 1970.
- [34] Claudia Marcelloni De Oliveira. *IBL installation into the inner detector of the ATLAS Experiment side C*. General Photo, May 2014.
- [35] M. Mikuž. *Diamond sensors for high energy radiation and particle detection*. TIPP, 2011.
- [36] W P C Mills. *The present performance of the SPS*. *IEEE Trans. Nucl. Sci.*, 26(CERN-SPS-AOP-79-9):3176–3178. 3 p, Mar 1979.
- [37] S. F. Novaes. *Standard model: An Introduction*. In *Particles and fields. Proceedings, 10th Jorge Andre Swieca Summer School, Sao Paulo, Brazil, February 6-12, 1999*, 1999.
- [38] Joao Pequenao. *Computer generated image of the whole ATLAS detector*. Mar 2008.
- [39] Heinz Pernegger. *The Pixel Detector of the ATLAS Experiment for LHC Run-2*. Technical Report ATL-INDET-PROC-2015-001, CERN, Geneva, Feb 2015.
- [40] S. Ramo. *Currents Induced by Electron Motion*. *Proceedings of the IRE*, 27:584–585, 1939.
- [41] V. Sarin. *Comprehensive Hard Materials*. Elsevier Science, 2014. p. 411.
- [42] W. Shockley. *Currents to Conductors Induced by a Moving Point Charge*. *Journal of applied Physics*, 9:635, 1938.
- [43] C. Weiss. A CVD diamond detector for (n,α) cross-section measurements. PhD thesis, TU Wien, Vienna, 2014.
- [44] C. Weiss, H. Frais-Kölbl, E. Griesmayer, and P. Kavrigin. *Ionization signals of diamond detectors in fast neutron fields*. publication in preparation, 2016.
- [45] J. L. Yarnell, J. L. Warren, and R. G. Wenzel. Lattice vibrations in diamond. *Phys. Rev. Lett.*, 13:13–15, Jul 1964.